Dynamic Radio location in medical environment

Dissertation

zur Erlangung des akademischen Grades

Doktoringenieur
(Dr.-Ing.)

von Dipl.-Ing. Danilo Briese M.A.
geb. am 09.11.1985 in Erfurt
genehmigt durch die Fakultät für Elektrotechnik und Informationstechnik
der Otto-von-Guericke-Universität Magdeburg

Gutachter:
Prof. Dr. rer. nat. Georg Rose
Prof. Dr. rer. nat. Thomas Neumuth

Promotionskolloquium am 26.04.2024

Declaration of Honor

„I hereby declare that I produced this thesis without prohibited external assistance and that none other than the listed references and tools have been used. I did not make use of any commercial consultant concerning graduation. A third party did not receive any nonmonetary perquisites neither directly nor indirectly for activities which are connected with the contents of the presented thesis.

All sources of information are clearly marked, including my own publications.

In particular I have not consciously:

- Fabricated data or rejected undesired results
- Misused statistical methods with the aim of drawing other conclusions than those warranted by the available data
- Plagiarized data or publications
- Presented the results of other researchers in a distorted way

I do know that violations of copyright may lead to injunction and damage claims of the author and also to prosecution by the law enforcement authorities. I hereby agree that the thesis may need to be reviewed with an electronic data processing for plagiarism.

This work has not yet been submitted as a doctoral thesis in the same or a similar form in Germany or in any other country. It has not yet been published as a whole.“

Bamberg, August 6, 2024

Danilo Briese

Kurzfassung

Offenchirurgische Operationen werden zumehmend durch minimalinvasive Eingriffe abgelöst. Eine Vielzahl technischer Verfahren ermöglicht erst die minimalinvasive Chirurgie. Medizinische Bildgebung, telemedizinische Geräte und bildgestützte Navigationssysteme sind Beispiele für deren Einzug in die medizinische Routine. Für den behandelnden Arzt steigen Zeit und Aufwand, um die technischen Geräte zu bedienen. Diese Entwicklung verdeutlicht, dass ein Zuwachs an neuen Geräten, Methoden und Funktionalitäten allein nicht ausreicht, um einen klinischen Mehrwert zu generieren.

Intelligente Wege zur Integration neuer und bestehender technischer Lösungen stellen wichtige Anforderungen für den klinischen Ablauf und große Herausforderungen für Medizingerätehersteller dar. Die Kenntnis der Position jedes Objekts zu jedem Zeitpunkt sowie die Identifikation der Objekte sind grundlegende Prämissen für ein ganzheitliches Konzept zur Integration automatisiert und manuell bewegter sowie stationärer Geräte. Das Ziel einer umfangreichen Integration sind Anwendungen, wie Kollisionsvermeidung zwischen Objekten oder anspruchsvolle Kooperation medizintechnischer Geräte.

Optische und elektromagnetische Navigationssysteme sind gegenwärtig in der interventionellen Therapie etabliert und industriell verfügbar. Sie erreichen die anwendungsbezogen geforderten Genauigkeiten, können aber das Bestreben einer umfangreichen Integration nicht unterstützen, da sie für markerbasierte Tools in einem dedizierten Sichtbereich konzipiert sind. Um die Nachteile bestehender Systeme sowie akademischer Ansätze zur optischen Raumüberwachung zu überwinden, fokussiert sich die vorliegende Arbeit auf Technologien zur Funkortung für die Lokalisation und Identifikation von Geräten und Objekten im medizinischen Umfeld.

Einleitend werden mit Radio Frequency Identification (RFID) und Ultra Wideband (UWB) zwei vielversprechende Technologiekandidaten betrachtet und hinsichtlich ihrer Eignung untersucht und bewertet. Zentraler Bestandteil der Dissertation ist eine Machbarkeitsstudie basierend auf UWB, da es die initial formulierten Anforderungen maßgeblich erfüllt. Ein Prototyp mit industriell verfügbaren UWB Modulen wird eingehend im medizinnahen Umfeld inspiziert. Mittels Sensorfusionsansatz wird das Sensorsystem mit dem Ziel verbesserter Dynamikeigenschaften erweitert. Es wird ein 9-Achs-Inertialsensor mit dem UWB System integriert und mit Hilfe eines modifizierten Kalman Filters fusioniert. Die Inertialsensordaten adaptieren direkt die Kovarianzmatrix des Filters. Dieser Ansatz führt zu wiederholgenauem Verhalten im statischen Fall und bildet die Dynamik eines beweglichen Objekts ab. Anhand von Experimenten im medizinnahen Umfeld wird gezeigt, dass eine UWB-gestützte Lokalisationslösung mit Sensorfusion die proklamierten Anforderungen erfüllt und ein ganzheitliches Integrationskonzept ermöglicht.

Abstract

Open surgery is more frequently replaced by minimally invasive interventions. A wide range of technical devices render minimally invasive surgical possible. Medical imaging and telemedical devices as well as imaging based navigation systems are popular examples that hold entrance to medical routine. The attending physician needs an increasing amount of his time and effort to operate these devices. This trend clearly shows that it needs more than new methods, functionality and devices to generate additional clinical value.
Smart integration of new and existing technical solutions are important requirements for clinical processes and a big challenge for medical device suppliers. Knowledge of spacio-temporal information as well as identification of objects are fundamental requirements for a holistic integration concept of automated and manually moved or stationary devices. Applications like collision avoidance between objects or challenging coregistered and cooperative collaboration of medical devices are the goal of an extensive integration.
Nowadays, industrially available optical and electromagnetic navigation systems are well-established for interventional therapy. They satisfy the required accuracy but cannot contribute to a comprehensive integration approach, since they mostly work with marker-based tools and a dedicated field of view. To overcome drawbacks of existing systems and academic approaches for optical surveillance, this thesis focuses on radio location technologies for localization and identification of devices and objects in a medical environment.
Firstly, two promising technology candidates Radio Frequency Identification (RFID) and Ultra Wideband (UWB) are scrutinized and assessed with regard to their suitability. Central part of this thesis is a feasibility study based on UWB, since it satisfies the initially formulated requirements superior to RFID. A prototype with industrially available UWB modules is evaluated in-depth in a medical environment. To improve the dynamic performance of the prototype an extension using sensor fusion is pursued. A 9-axis-inertial sensor is integrated with the UWB system and fused by using a modified Kalman Filter approach. The inertial sensor data directly adapts the filter's covariance matrix leading to precise behavior in static cases as well as good dynamics for moving objects. Experiments in a medical environment have shown that an UWB-based localization with sensor fusion can satisfy the formulated requirements and is well suited for a holistic integration concept.

Contents

VI Appendix

List of Figures

List of Tables

Part I

Introduction

1 Motivation

In recent times, there has been a growing trend in the utilization of advanced technical equipment and devices in medical interventions (TS03; Gom11) and more and more of the surgeons‘ time and effort is needed to operate technical devices. This development makes it clear that it is not enough to only provide more devices, methods and features, but also smart ways of handling these new tools to seamlessly integrate them into the clinical workflow. This rising demand can be witnessed in many clinical fields. „The modern operating room requires an increasing number of new surgical instruments, monitoring and imaging devices, information systems, and communication networks.“ This is the opening statement of the workshop „OR 2020, The Operating Room of the Future“ in 2004 with approximately 100 attendees from different clinical and technical fields (CK05). Five common themes were identified that relate to all aspects of the operating room of the future, one of which is „Interoperability of devices“. One basic prerequisite for integrated behavior or interoperability of individual technical devices in medical environments is the knowledge of spacial information of each of the devices at any time it is needed. To enable advantageous applications amid both actively moving and stationary devices, a localization system with identification information regarding the localized objects is required. Figure 1.1 visualizes a typical crowded hybrid operating room comprising a C-arm imaging system, an operating table with led shields, ceiling mounted lights and displays and several trolleys like an anesthesia cart. In addition to established medical devices surgical robots could be part of an advanced medical ecosystem in the interoperable OR. With a spatio-temporal localization framework, it becomes feasible to enable sophisticated applications like collision avoidance to prevent mobile device collisions, and co-registered operations involving multiple devices (CLM$^+$07).

Today‘s operating rooms and interventional suites already comprise a large variety of technical devices starting with a motorized movable patient table, a mobile or fixed imaging system, a display, carts and trolleys. Additional devices do not only improve the physicians possibilities e. g. to perform minimally invasive interventions but also add to the complexity of the room setup. Especially moving devices automatically like robots or the cone-beam system itself lead to a need for additional safety considerations. Even a setup with comparably few moving components like shown in figure 1.2 generates the need for ideas on collision avoidance or cooperative movement between the actively moving devices.

Figure 1.1: Typical hybrid operating room setup with ceiling-mounted cone-beam CT system Artis zee, Siemens patient table, large ceiling mounted display, ceiling supplies with OR-lights and other devices positioned on movable trolleys. (Inc17)

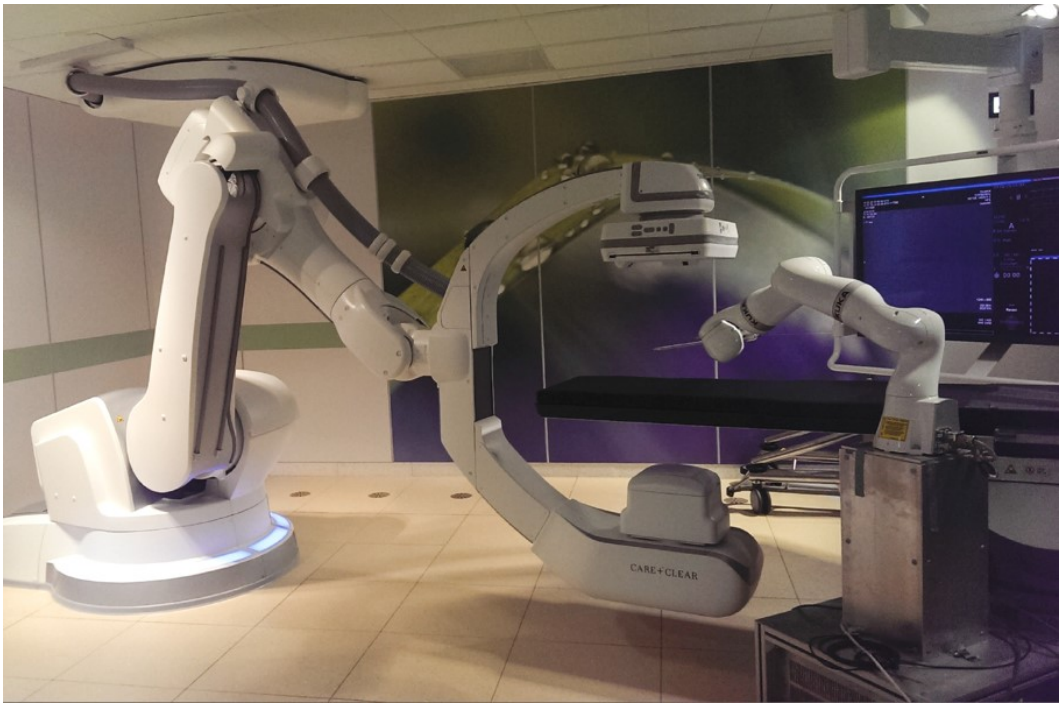

Figure 1.2: Interventional suite setup with robot-based cone-beam CT system Artis zeego, Maquet patient table, large ceiling mounted display and leight weight robot positioned on a movable trolley. (GBMR15)

For today's individually used technical devices well-established approaches exist for localization and co-registration with e. g. the imaging system to provide additional information by combination of the information of two worlds. Some technologies have been used in the interventional suite or operating room for many years. Two of the most well known and estab-

lished examples are optical end electromagnetic navigation systems frequently used to track medical tools like catheters or screws during intervention. Many publications like (RRK+08) suggest that navigation based tool positioning is superior to freehand targeting. Based on these outcomes a large variety of products in the field of medical tool tracking has arisen. In (SRHM+08) three industrially available optical navigation systems are compared regarding localization accuracy. Differences between the three systems are in the sub-millimeter range and are found to have a negligible effect on the quality of the medical procedure. Two established products from Medtronic (Med17) and Brainlab (Bra17) providing optical navigation solutions are shown in figures 1.3 and 1.4. The electromagnetic navigation approach is represented by Stereotaxis' Niobe system (Ste17) in figure 1.5.

Figure 1.3: Medtronic surgical imaging system comprising an O-arm X-ray system and a Stealth Station optical navigation system. (eur16)

Figure 1.4: Brainlab Brainsuite iMRI with high-field intraoperable MRI and optical navigation system. (Mid06)

All of these navigation solutions focus on the tracked medical tool and on the registration to available image data. They lack the ability to track spatio-temporal information of other

Figure 1.5: Stereotaxis Niobe EM system combined with Artis zee cone-beam CT system. (Hea17)

devices in the operating room of the future and thus cannot fully integrate them into one advanced medical ecosystem.

There are different approaches to overcome this local behavior of industrially available clinical navigation systems. (LBN08) is provided as an example to realize room supervision in a medical environment by using 16 cameras on the ceiling and fusing their image outputs to a voxel representation of the captured scene. Four workstations where set up to control four cameras each and provide a prereconstruction. A fifth computer combines the partial reconstructions and performs a collision test. The sheer amount of 16 cameras highlights the challenges due to line of sight occlusions in a crowded and dynamic environment. To overcome shadowing artifacts the positioning of the cameras is demanding and does not necessarily lead to a solution with good coverage. When pursuing a camera based solution it is also crucial to consider the light conditions in the environment. It could lead to disastrous outcomes if the supervision system would fail under faint light conditions, which are frequently encountered in clinical environments to have a high contrast perception of the medical images.

To overcome drawbacks of local navigation solutions or optical surveillance approaches, this thesis focuses on radio location technology for localization of objects in a medical environment.

2 Goals and Structure

Topic of this thesis is the prototypal development of a radio location system based on industrially available components, and the evaluation of this system regarding it's feasibility for the proposed medical environment. Major requirements for the aspired localization solutions are:

- Technology decision based on a comprehensive technology evaluation
- Use of industrially available hardware
- Implementation of a suitable localization framework
- Localization accuracy in the low centimeter or sub-centimeter range
- High localization precision in sub-centimeter range in static and dynamic environment

The remainder of this thesis is structured into four parts, each supporting specific aspects of the goal of this thesis.

Part II - Fundamentals
This part provides a technology study on different aspects of the two scrutinized radio technologies, RFID and UWB, including the technical background and worldwide regulations. The state of the art in scientific literature and industrial implementations is given. The evaluation of the radio technologies results in a decision of the preferred technology for satisfying the major requirements of a localization system. Furthermore four well-established ranging technologies and three popular localization techniques are introduced to give an overview of the possibilities for radio-based localization systems.

Part III - Radio Location Prototype
The prototype setup based on the chosen radio, ranging and localization technologies is described in the beginning of this part. Thereafter, tracking filters are introduced, that are implemented into the radio location prototype to improve the localization results are introduced. Experiments based on simulations and real measurements in a medical environment are conducted, evaluated and compared regarding the overall Ultra wideband results and the tracking filter effectivity.

Part IV - Dynamic Radio Location Prototype
An extension of radio location with additional sensor data is pursued in this part. Several external sensor types are introduced and evaluated regarding their suitability to enhance UWB localization information. Inertial Measurement Units are found to best fit UWB data and two industrially available implementations of Inertial Measurement Units are compared based

on performed real measurements experiments. The approach of fusing measurement data of both sensor types is introduced and evaluated with experiments in a medical environment.

Part V - Summary, Discussion and Outlook
This concluding part provides a summary of the thesis, discusses the developments, experiments and results and gives an outlook to future work or other possibilities in the context of UWB localization.

Part II

Fundamentals

3 Radio Technologies

Radio technology uses electromagnetic waves to propagate information through media. In contrast to optical technologies, radio propagation uses electromagnetic waves of a different frequency. Whereas optical waves are in the range of hundreds of gigahertz in the infrared to hundreds of terahertz in the spectrum of visible light, radio technology uses the spectrum of radio and microwaves from kilohertz to hundreds of gigahertz. In chapter 1 it is shown, that optical localization systems have several drawbacks in challenging medical environments. Depending on the part of the radio technology spectrum the characteristics of electromagnetic waves differ in various aspects. That is why localization systems based on radio technology are used in a wide field of applications. It is also the reason why it is important to identify the appropriate radio technology for a specific task and environment. In this chapter two well known radio technologies, that provide industrially available implementations, are introduced and evaluated for their suitability to provide radio localization in medical environment. Radio frequency identification (RFID) is a technology originally used to provide identification information based on electromagnetic waves where no other technology could be applied, like for aircrafts (Dob12). It is also applied to overcome the use of optical identification mechanisms like barcodes or technologies that need contact for identification. RFID can also provide localization information in addition to identification. In section 3.1 RFID is introduced. Ultra wideband (UWB) makes use of a broad spectrum of electromagnetic waves in contrast to a narrowband signals like RFID. One possible application with industrially available systems with UWB technology is high data rate transfer, but it can also provide ranging information for localization systems. In section 3.2 UWB is introduced. A conclusion on the suitability of the introduced radio technologies for localization in medical environment is given in section 3.3.

3.1 Radio Frequency Identification

RFID is based on the idea of identifying an object using electromagnetic waves to exchange information. RFID is not one specific technology but a variety of approaches that differ in the used signal frequency, the power supply of the sensor and the protocol for information transfer. (DKA07) gives a short introduction to the history of RFID, types of frequencies and industrial applications. Nevertheless, a link between RFID systems can be found since every one consists of three mandatory components (Dob12):

- transponder or tag on the object to be localized
- reader or interrogator that, depending on implementation, is used for reading and writing
- antennas or coils to send and receive electromagnetic waves and to mediate between those waves and voltages on wires

The tag and reader both comprise antennas or coils. Figure 3.1 gives an example for RFID transponders comprising a coil or an antenna as the coupling device.

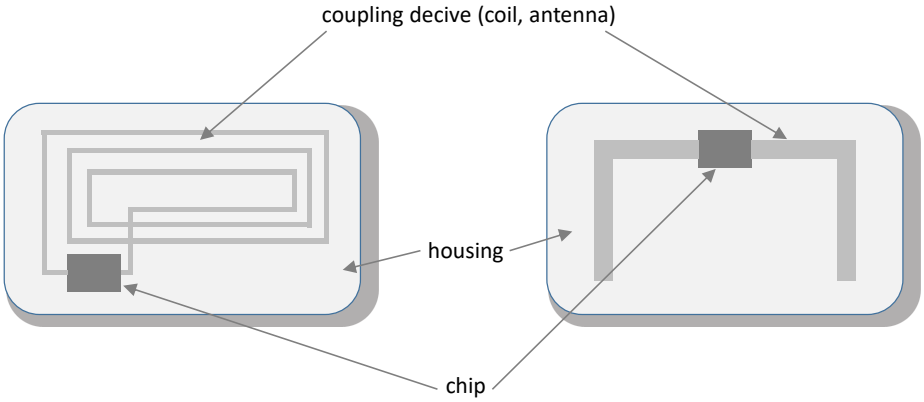

Figure 3.1: Two examples of RFID transponders. The left implementation comprises a coil as coupling device, whereas the right transponder uses a dipole antenna. Both characteristics have their right to exist dependent on the part of the electromagnetic spectrum in use.

In figure 3.2 an RFID system consisting of a reader and a tag are displayed. The two-way communication between both components is shown. By exchanging the ID stored in the tag, the reader identifies the object to be observed.

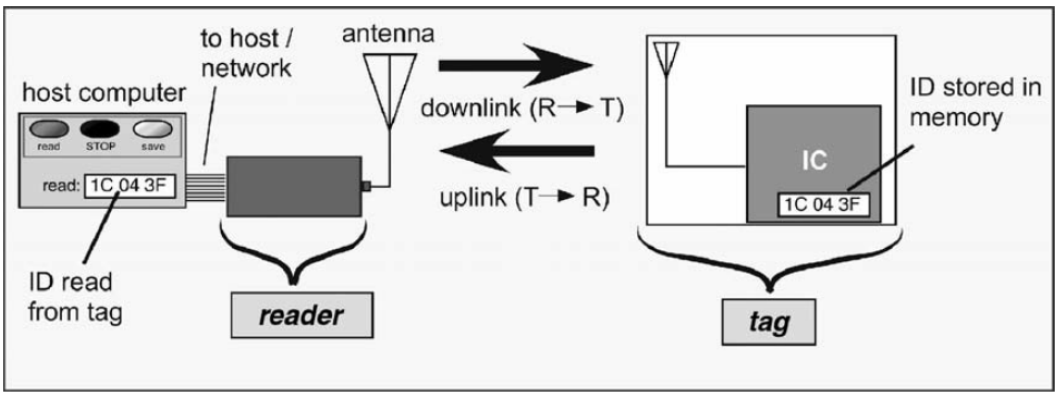

Figure 3.2: RFID system comprising a reader unit with antenna and link to a host computer and a transponder or tag with antenna and integrated circuit (IC) containing the (unique) identification (ID). Up- and downlink describe a communication between reader and tag in both directions to exchange the ID or other additional information. (Dob12)

Since there is no specific RFID technology, section 3.1.1 focuses on identifying and evaluating the best suited technology set from the variety of RFID approaches for localization in medical environment. Section 3.1.2 introduces backscatter coupling for UHF signal frequencies as a technology for long range RFID systems. Section 3.1.3 sheds a light on RFID localization in literature and industrially available implementations.

3.1.1 Finding a suitable RFID technology

To find the right RFID characteristics for the goal of localizing objects in medical environment the used signal frequency is the most important parameter to start with (Fin12). Depending on the chosen signal frequency a variety of characteristics can be realized for RFID systems. Figure 3.3 gives an overview of the spectrum of electromagnetic waves used for RFID and highlights frequency bands that are used for industrially available implementations. It also structures the available spectrum into the two regions „inductive“ and „radiative“. These regions indicate the coupling behavior used by the RFID system.

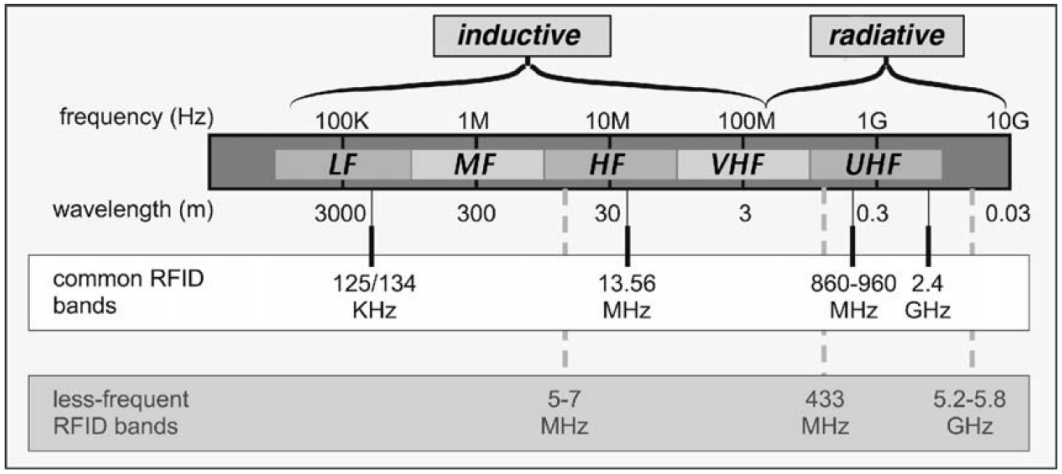

Figure 3.3: Overview of the used frequency bands and corresponding wavelengths for RFID systems (Dob12). The spectrum is split into two regions, „inductive“ and „radiate“, that describe the coupling behavior of the RFID system. Existing RFID bands are presented with common industrially used bands being highlighted.

The most frequently used frequency bands for industrially available RFID systems have given these types their commonly used names:

- 125 / 134 kHz — low-frequency (LF)
- 13.56 MHz — high-frequency (HF)
- 860 - 960 MHz and 2.4 GHz — ultra-high-frequency (UHF)
- 5.8 GHz — super-high-frequency (SHF)

The variety in frequencies naturally results in a large variety in wavelengths. By using equation 3.1 the wavelength of a radio signal can be deduced from frequency f and speed of light c.

$$\lambda = \frac{c}{f} \tag{3.1}$$

This leads to wavelengths in the range of kilometers for LF systems and centimeters for UHF and SHF systems. Based on (Dob12) systems with a large wavelength compared to antenna size are typically inductively coupled, whereas systems with a wavelength comparable to antenna size usually use radiative coupling. The coupling behavior of an RFID system has a major influence on the range for reader transponder communication. Inductive coupling takes place in the near-field of the antenna whereas radiative coupling works in far-field distances. In case of inductive coupling the electromagnetic field strength attenuates as the cube of distance d $(1/d^3)$ or $60\,dB$ in the near-field of the RFID reader antenna. For radiative coupled RFID systems only the space attenuation or free space path loss in the far-field is of importance which leads to a field strength decline as the distance d $(1/d)$ or $20\,dB$. Figure 3.4 provides an example of the near-far field transition for a HF RFID system. It illustrates the electromagnetic field strength over the distance from the antenna and indicates the region of the transition from near- to far-field. For other signal frequencies used, the near- to far-field transition works at a different distance level.

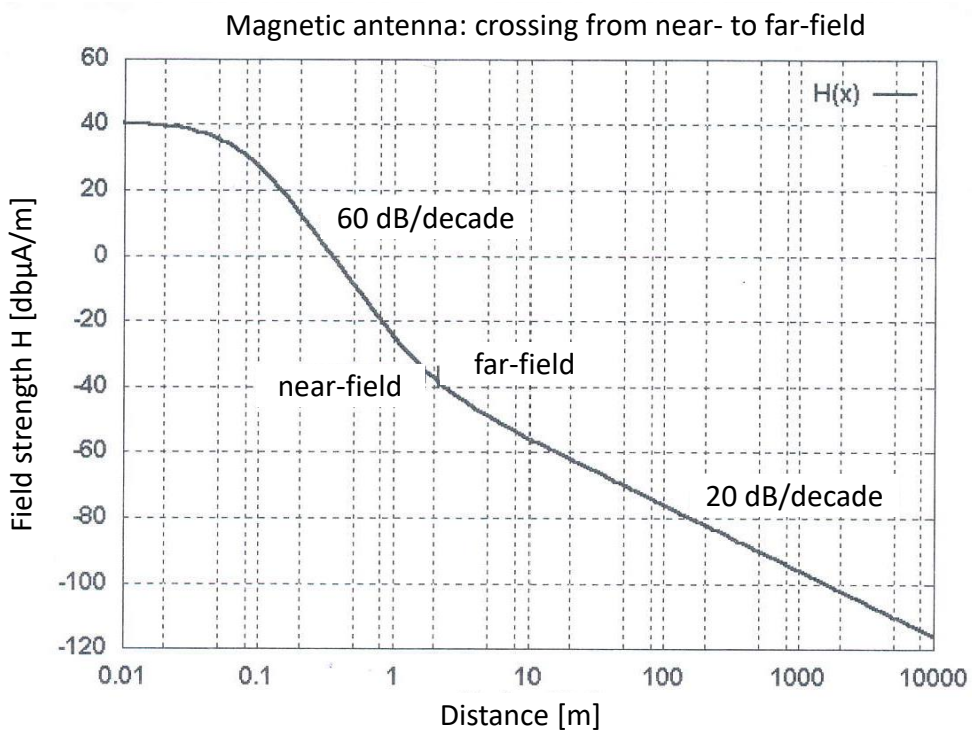

Figure 3.4: Electromagnetic field attenuation over the distance from the antenna for a HF RFID system. The transition from near- to far-field is highlighted and also describes the transition from inductive to radiative coupling. Based on (Fin12).

Based on (Fin12) RFID systems can be structured by their range, beginning with close

coupling systems with a range below $1\,cm$. They are typically utilized for applications with a strong safety background but no need for long range. Examples can be found in access control or payment by contactless chip card. Frequencies in the range of LF and HF are used to implement close coupling systems. A second range group of RFID systems are remote coupling systems which work in a range of up to $1\,m$. They also utilize LF and HF systems with inductive coupling. Typical applications are animal identification or industrial automation. RFID systems operating in a range over $1\,m$ are called long range systems. They utilize UHF and SHF frequencies and work with radiative coupling in the far field. The most common working principle for long range systems is backscatter coupling.

Both approaches to classify RFID systems based on their operating range and their used signal frequency lead to the same result of inductive coupling with LF and HF systems not being suitable for a localization application in a room supervision scenario in medical environment.

The decision for a signal frequency not only influences the range capabilities of an RFID system but also defines characteristics like the interaction or penetration of the used signal impinging on material it comes into contact with. (Dob12) provides the skin depth δ to describe this penetration. Equation (3.2) elucidates the interaction of frequency f, magnetic permeability μ, and the electrical conductivity σ to form the skin depth δ.

$$\delta = \sqrt{\frac{1}{\pi \mu \sigma f}} \tag{3.2}$$

Table 3.1 gives an idea of penetration depth for common combinations of signal frequencies in RFID systems and materials in medical environment.

Table 3.1: Material penetration of RFID signals with different signal frequencies.

material	penetration depth at			
	$125\,kHz$	$13.56\,MHz$	$865\,MHz$	$2.4\,GHz$
Tap water	$8\,m$	$2\,m$	$4\,cm$	$8\,mm$
Human tissue	$1.2\,m$	$11\,cm$	$2.7\,cm$	$1.8\,cm$
Carbon	$5.3\,mm$	$0.5\,mm$	$63\,\mu m$	$38\,\mu m$
Lead	$0.65\,mm$	$62\,\mu m$	$7.8\,\mu m$	$4.7\,\mu m$
Aluminum	$0.23\,mm$	$22\,\mu m$	$2.8\,\mu m$	$1.7\,\mu m$
Iron	$20\,\mu m$	$1.9\,\mu m$	$0.2\,\mu m$	$0.15\,\mu m$

It can be seen that low signal frequencies have a huge advantage in material penetration over high frequencies. This behavior would overcome line-of-sight problems for localization purposes for some relevant materials like water and human tissue, but lacks in communication range due to inductive coupling. For common material in medical environment like lead glass or lead shielding, carbon and iron low signal frequencies do not provide a reasonable penetration to overcome line-of-sight issues either. UHF signals can only provide penetration for thin layers of water or tissue but fulfill the range requirements.

To summarize the outcome of finding a suitable RFID technology for localization in medical environment based on (Dob12):

- LF and HF uses inductive coupling and therefore does not work for long range communication. UHF works with radiative coupling, especially backscatter, and provides long range communication.
- LF and HF tags use coil antennas with more or less turns. UHF tags use dipole-like antennas
- LF and HF penetrate water and human tissue well. UHF only provides penetration for centimeter ranges in water and human tissue.
- Neither LF, HF nor UHF are able to penetrate metal in reasonable depths.
- LF, HF and UHF easily penetrate other non conductive material like clothing or medical cloth.
- LF RFID systems provide low data rates between tag and reader, whereas HF and UHF manage much higher rates.

For a localization system capable of monitoring a room in medical environment, the range capability is the most important parameter. Due to the lack in range for inductive coupling with LF and HF RFID systems the remainder of this chapter focuses on UHF systems with backscatter coupling. The drawback of not penetrating conductive material like human tissue and water comparable to lower frequencies have to be accepted and considered as constraints in localization system design.

3.1.2 Backscatter RFID

Using backscatter radiation for communication is a common principle in radiatively coupled RFID systems working in far-field. It makes use of the RFID transponder affecting the electromagnet field emitted by the RFID reader. As learned from figure 3.2 on page 12 the IC on the tag holds the identity of the object that is tagged with the transponder. This ID information needs to be transmitted to the reader using the backscatter. Figure 3.5 gives an overview of power spreading of a radiatively coupled RFID signal and the tag response as a backscattered wave.

The electromagnetic field emitted by the RFID reader is a continuous wave (CW) signal. To provide information this signal has to be modulated. Often a resistor is used as a load in the RFID transponder. By switching it on and off the signal is modulated resulting in a binary sequence providing the unique ID of the RFID tag and communication information. The modulated signal is radiated into free space and a proportion of this signal is received by the reader antenna after being backscattered by the tag. Since the signal provided by the reader is many times stronger than the received backscattered signal they have to be differentiated. This is possible due to the fact that by modulating the signal on transponder side it provides its information in two sidebands slightly higher and lower than the emitted signal frequency ω. With this in mind the signal can be filtered at the receiving side of the reader and the two sidebands can be demodulated to get the information of the RFID tag.

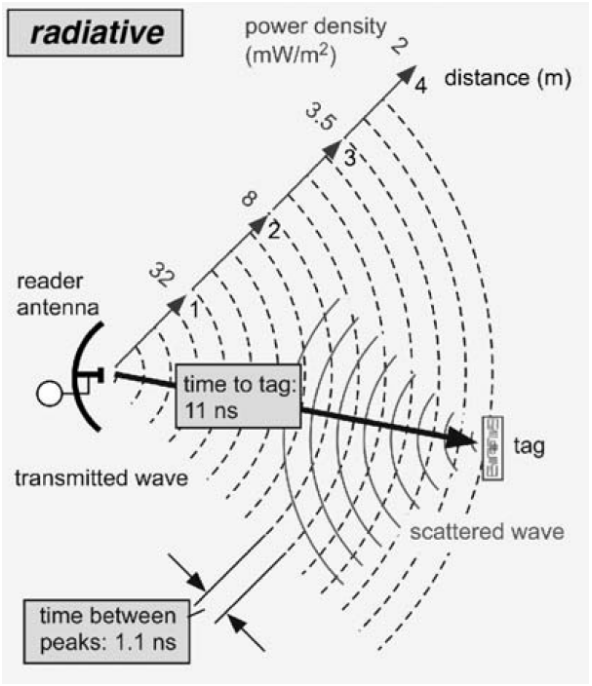

Figure 3.5: Schematic visualization of radiative coupling with a reader antenna transmitting an electromagnetic field and a tag located in the field. It shows the power density of the field along the distance from the reader antenna. The RFID transponder receives the field, manipulates it by modulation and sends it back in a backscatter manner. (Dob12)

There are different approaches and modulation schemata available in literature and industry (AWM09) (Kue12). Basic information on modulation and sidebands in backscatter RFID can be found in (Rem09).

The achievable range and type of signaling is fundamentally influenced by the choice of power supply for the RFID tag. In general there are three different ways to handle the electrical supply of the tag. In figure 3.6 the approaches from passive, semipassive to active are visualized, as well as their power source and signaling.

In the passive and semipassive approaches the information is transmitted by a backscattered modulated wave received from the RFID reader and affected by the RFID tag. In contrary to the passive case, where the electronics on the tag are powered by extracting energy from the reader's electromagnetic field itself, the semipassive and active tags both have a battery to power the electronics. Additionally, the active tag provides it's own modulated signal and not a backscattered signal from the RFID reader. Passive tags provide the more cost effective solution when compared to semipassive or active tags. Furthermore they allow for the best workflow options since they do not need to be charged and thereby add operational convenience. These arguments make passive tags an idea worth pursuing for localization systems in a medical environment. On the contrary passive tags need to extract all the energy needed for tag operation from the RFID reader's field. (Fin12) gives equation (3.3) to find a measure for the free space path loss given the range r, the frequency f and the gain

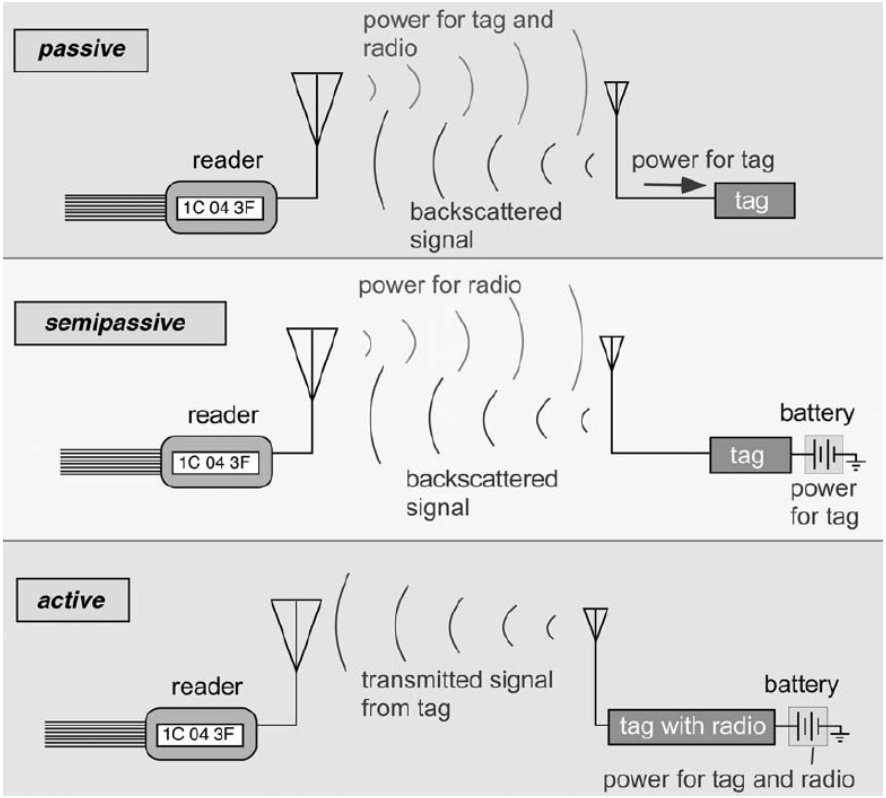

Figure 3.6: Three ways of powering an RFID tag are visualized. In the passive case the tag is powered by the electromagnetic field itself and extracts the energy needed for the electronics from that field. In the semipassive case the energy for the electronics on the tag are provided by a battery, but for signaling purpose only the field from the reader is backscattered. The active approach uses a battery to power the electronics on the tag and also provide the energy for transmitting the signal to the reader. (Dob12)

of the tag antenna G_T and reader antenna G_R.

$$a_F = -147.6 + 20 \log r + 20 \log f - 10 \log G_T - 10 \log G_R \tag{3.3}$$

The free space path loss a_F characterizes the proportion between the energy emitted by the RFID reader and the energy received by the RFID tag. By knowing the power consumption of the utilized passive RFID tag and the efficiency of the rectifier the achievable communication range can be estimated. Taking into account an IC with $5\,\mu W$ power consumption and an efficiency of 10 %, the field needs to provide $50\,\mu W$ at the tag antenna. With an RFID reader emitting $2\,W$ equivalent radiated power (ERP) or $3.3\,W$ equivalent isotropically radiated power ($EIRP$), the free space path loss must not exceed 48.2 dBm. Under the assumption of a dipole tag antenna with $G_T = 1.64$, an isotropic reader antenna with $G_R = 1$ and a signal frequency of 865 MHz, the passive UHF RFID system can provide a communication range of $r = 9.1$ m. For the same RFID system with a signal frequency of 915 MHz, which is used in the USA, the communication range shrinks to $r = 8.6$ m. For the concept of a localization system

in medical environment these communication distances are sufficient. Therefore, and because of the greater operational effectiveness discussed previously, we focus on passive RFID tags for the reminder of this chapter. When trying to use higher frequencies like 2.45 GHz or 5.8 GHz, the available communication range for the given parameters drastically decreases to $r = 3.2\,\mathrm{m}$ and $r = 1.4\,\mathrm{m}$, respectively. This is a drawback but could be compensated by using ICs with lower power consumption and a more efficient rectifier.

Another topic to look at is the regulatory point of view in UHF and SHF RFID. The regulatory environment in the UHF region from $860 - 960\,\mathrm{MHz}$ is complex and diverse for different countries. Figure 3.7 gives an impression of the worldwide regulations in UHF RFID from $860 - 960\,\mathrm{MHz}$ in 2006.

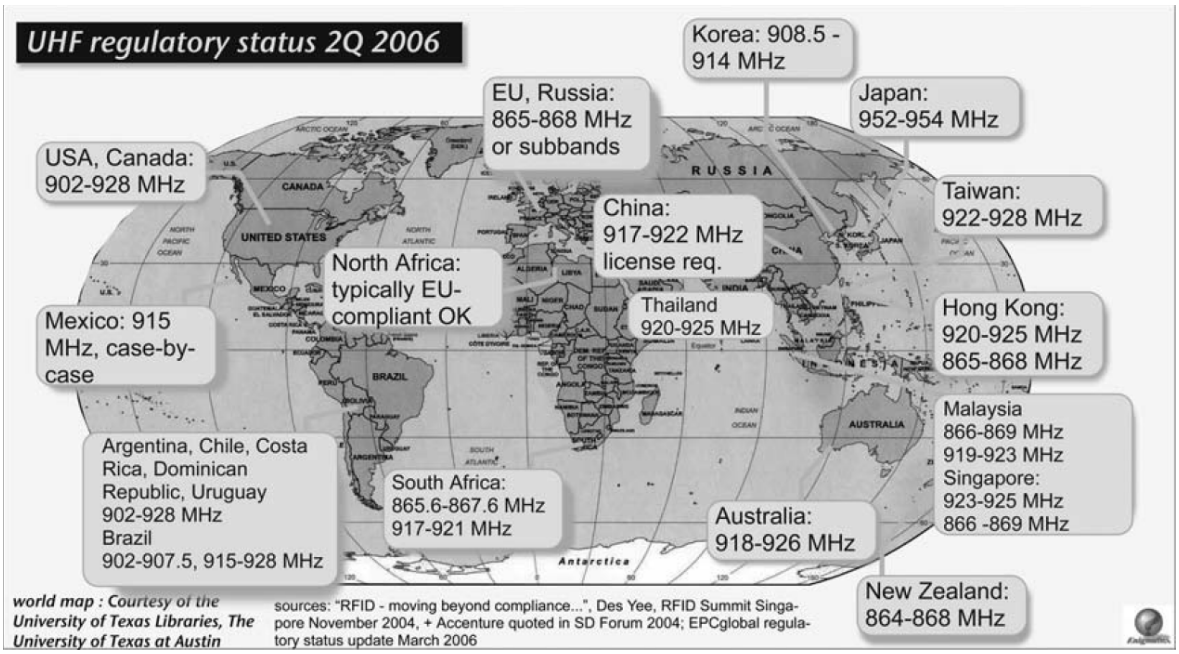

Figure 3.7: UHF regulatory map of the world from 2006. Every nation can specify their own regulatory requirements. On the contrary to that freedom it can be seen that worldwide frequencies from 865 MHz to 954 MHz are specified and in many countries cling to regulations from either Europe or the USA. (Dob12)

It can be seen, that the Federal Communications Commission (FCC) in the USA and the European Telecommunications Standards Institute (ETSI) provide different regions in the electromagnetic spectrum to use for UHF. Most other countries align to FCC or ETSI regulations. The current regulatory status of the UHF RFID spectrum usage can be found in (GS116). In the current version from November 2016, it provides 81 countries listed with their respective frequencies, radiated power, communication techniques and the responsible regulator. For the maximum radiated power mainly two different conventions are used. Whereas the ETSI uses the effective radiated power (ERP) to describe the radiated power, the FCC uses the effective isotropic radiated power (EIRP). Both conventions can be used interchangeably by applying a conversion based on equation (3.4).

$$\mathrm{dBm(ERP)} = (\mathrm{dBm} - 2.15)(\mathrm{EIRP}) \tag{3.4}$$

With the FCC and ETSI allowing 4 W EIRP and 2 W ERP, respectively, and converting EIRP to ERP the difference comes down to 0.75 dBm or 0.37 W higher maximum radiated power for the FCC regulation. This generates a need for different hardware to provide a worldwide functioning localization system based on the $860 - 960$ MHz UHF frequency range.
$2.4 - 2.45$ GHz RFID works in a region of the electromagnetic spectrum that is available for unlicensed operation almost anywhere in the world. This makes it easy to provide one solution with one hardware for a worldwide release. On the contrary, this region presents a high chance of interference, as it is crowded with other users of this spectrum like telephones, wireless local-area networks or Bluetooth. Taking the lower communication range and the crowded spectrum prone to interference into account, 2.4 GHz or even 5.8 GHz RFID are inferior to $860 - 960$ MHz RFID systems for the purpose of a localization system in medical environment.

3.1.3 Available RFID localization systems

The first generated and transmitted continuous wave (CW) radio signal was demonstrated by Ernst F. W. Alexanderson in 1906 (Lan05). This experiment marks the starting point of modern radio communication (Lan05). In 1948, (Sto48) presented the paper „Communication by Means of Reflected Power“ which introduces the idea of RFID but also claims that much effort is needed to enhance this technology for useful applications. It took its time to improve hardware used for RFID with e. g. the usage of CMOS circuits and EEPROM to reduce RFID transponder size and price. It was also important to solve regulatory questions and be able to use the invention of the personal computer (PC) to exploit the full potential of RFID. Figure A.1 sheds a light on the variety of RFID transponders from printed paper-thin models to wearables or exemplars with massive housing. With an increasing amount of industrial application for RFID in the 80s and 90s (Lan05) the idea grew to also be able to localize the tagged objects instead of just identifying them. One of the few products to provide RFID localization and not only presence in a certain room or position on a conveyor belt is NaviFloor by Future-Shape GmbH (Nav17). It uses a landmark-based approach where RFID transponders are distributed into a special floor with a grid size of 50 cm. WhereNet by Zebra Technologies is another RFID localization product. It provides industrially usable transponders with a ranging accuracy of 30 cm (Whe17). The accuracy realized with both systems is not sufficient for a localization system in medical environment. Over the past 15 years, there has been a growing and still ongoing interest in RFID localization systems in the scientific community with a broad spectrum of approaches towards the goal of localization. The following paragraphs shed light on different approaches to RFID localization based on signal strength, signal phase at one and multiple frequencies, coverage region and fingerprinting, respectively.

Signal Strength One of the first RFID lcalization systems is SpotON by (HWB00), published in 2000. It provides an aggregation approach based on received signal strength (RSS) for localizing the transponders and realizes an accuracy of up to $1\,\mathrm{m}^3$. In 2004 LANDMARC was introduced by (NLLP04), which provides localization based on RSS by using reference tags at 308 MHz. The achievable accuracy also lies in the range of $1\,m$ with the maximum error being less than 2 m. In 2009, an extended version of LANDMARC with 3D localization and passive transponders was introduced by (KA09). It achieves an accuracy in position estimation of 0.5 m.

Coverage Region A quiet different approach is given by (LCS06) with „Ferret“ in 2006. It provides a mobile tracked reader that, based on the reading of the RFID tag, adjusts a probability map of where the tag is located. By moving the reader around the map shrinks to those areas where a tag is likely to be found. The achievable accuracy is given with 1 % of the readers „field of view“. Since you have to move the reader around to get an idea of the tag's position, you have to track the RFID reader to make reasonable results. It also takes some time for the tag location area to shrink.

Reference-based (SBC09) provides the idea of fingerprinting for RFID reader localization with a great number of reference transponders on the ceiling and a database of reference measurements for certain positions. It uses read results of the reference tags to map it to a reader position based on the database. The approach achieves a localization accuracy of less than 60 cm. In (CRZ10) and (CR11) present an improved fingerprinting approach by calibrating reference tags with changing power levels of the RFID reader. In the conducted experiments they showed an overall accuracy of $15 - 18\,\mathrm{cm}$. PinIt is a reference-based localization approach by (WK13) that exploits multipath measurements to obtain position estimates. It provides a beam steering antenna that additionally moves on a line to simulate an antenna array. The beam steering allows the proposed system to realize an angle of arrival estimation for the target transponder and the reference tags. Based on that measurements it creates a multipath-map and compares the paths of the target with the references. With this approach and a reference tag map of $15\,cm$ spacing an accuracy median of 11.2 cm is achieved. In (MKV11) and (MKV13) a localization approach based on synthetic aperture produced by moving the RFID reader is provided. It uses a holographic representation of the tag location probability. Measurements conducted in an office environment 2D scenario with a synthetic aperture of 1.2 m and a step size of 2 mm give a localization accuracy of 2 cm in x-direction, parallel to the aperture, and 7 cm in y-direction, orthogonal to the aperture. With measurements in a different setup using an aperture of 0.8 m and a step size of 4 cm the accuracy for tag localization remains good in x-direction but decreases to 0.5 m with a standard deviation of 0.8 m in y-direction.

Signal Phase In 2007, one of the first angle of arrival (AOA) localization schemata, called direction estimation, was introduced by (ZAK07). It provides a two antenna array which

exploits the phase-difference-of-arrival (PDoA) of the backscattered signal and computes the direction or angle of the incoming signal wave. It achieved an angular accuracy of $1.5 - 2$ deg standard deviation. Further approaches making use of phase-based measurements are proposed by (HBE+09), (NMR+10) and (PS11). In 2010, also implementing a phase-based RFID system, localization results in millimeter range are experimentally shown under ideal situations by (HWGL+10). In (ACD+11b) and (ACD+11a) a phase-based AOA localization approach is provided with off-the-shelf RFID reader and transponder hardware in an office environment. The experiments lead to a mean error in localization accuracy of 0.21 m and 0.10 m respectively.

In (WW10) a simulation on close to ideal noise free phase-based measurements is conducted. The results provide a best case scenario for phase-based RFID localization with an accuracy below 2 mm in direct line-of-sight environment. Real measurements where conducted in (WBW11) in a plastic basin shown in figure 3.8 with nearly ideal conditions in terms of multi-path propagation, spatial extent of the measurement area and reflective objects.

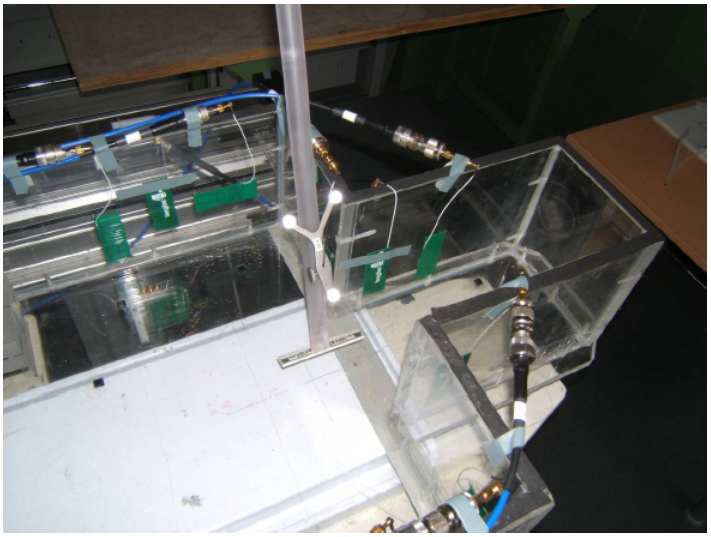

Figure 3.8: Measurement Environment for RFID localization experiments. (WBW11)

Training datasets are acquired and used in a supported vector regression (SVR) algorithm to determine the transponders localization. Results are provided in the range of millimeters for small regions of interest. Further experiments in the same environment in (WMW12) realize different raster sizes for training datasets and compare signal strength, phase-difference and a reader-based post-processed phase-difference. The measurements lead to accuracy measures from $1.0 - 4.2$ mm depending on the training grid size and the conducted measurement paths.

(SVHJ12) presents an approach to overcome the phase measurements' wavelength ambiguity by introducing an extended Kalman filter and the Rauch-Tung-Striebel smoother. It includes position, velocity and the phase offset of the antennas used. Experiments are conducted in a $3\,\text{m} \times 3\,\text{m}$ anechoic chamber with four antennas and a moving tag at 890 MHz with a root mean square error of 3.2 cm and 1.5 cm respectively. (SPS+13) provides a phase-of-arrival based localization approach with a frequency-stepped continuous waveform to overcome multipath

disturbances. Experimental measurements with eight antennas result in a median error of 3.6 cm and a root mean square deviation (RMSD) of 0.6 m. By additionally applying a tracking algorithm to account for outliers the precision could be improved to $RMSD = 3.8$ cm. An extension to this approach that combines phase-of-arrival (PoA) and phase-difference-of-arrival (PDoA) algorithms is given in (SPS14). The PDoA provides information on the movement of the RFID transponder. The median error in experimental measurements in given with 1 cm and the RMSD with 6.4 cm.

Multi-frequency (LZA09) implemented a multifrequency-based phase-difference-of-arrival approach. It overcomes the ambiguity of phase-based ranging methods by using more than one signal frequency with a certain separation in the spectrum. In figure 3.9 the achievable accuracy is shown over the frequency separation for three signal to noise ratio (SNR) levels.

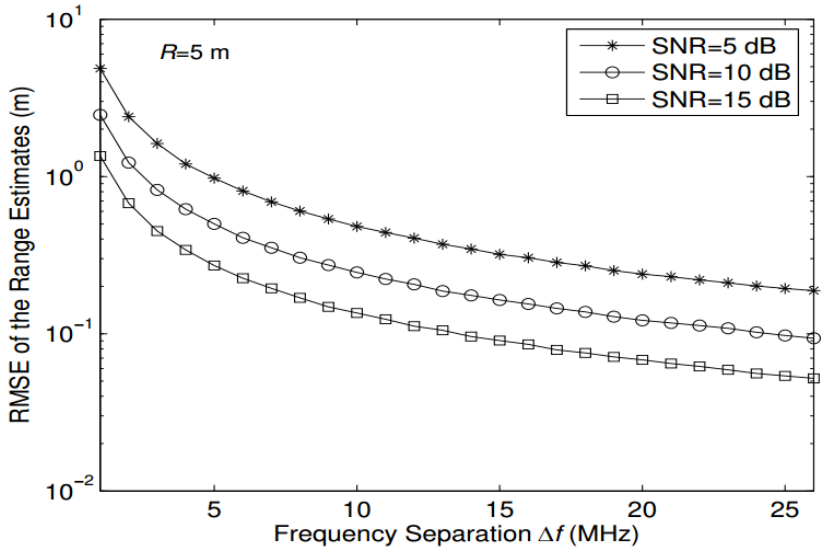

Figure 3.9: Achievable accuracy for range estimation with a multifrequency-based ranging approach. The figure shows the root mean square error (RMSE) for range estimates over frequency separation for three signal to noise ratio (SNR) levels. (LZA09)

It can easily be seen that a higher SNR leads to better results. A higher frequency separation also improves the ranging accuracy. With having the regulatory map 3.7 in mind one can easily derive that it is possible to achieve a frequency separation of 26 MHz in the USA with a root mean square error (RMSE) of up to 5 cm. With the regulatory situation in Europe it is only possible to provide a separation of 3 MHz with a RMSE of roughly 40 cm, which severely limits the potential of this solution. A slight extension of this approach is given by (VPJ10), which accounts for the reflection behavior of unknown RFID transponders but also is in need of high bandwidth to achieve the proposed mean error of 68 mm and a maximum position error of less than 40 cm.

General Some general aspects of RFID localization that apply to many or all provided methods and algorithms have been investigated over the years. (PC11) discusses the influence of

interference occurring for simultaneous reading of RFID transponders, one RFID tag being read by multiple RFID readers or reader to reader interference. They compare different localization algorithms regarding their behavior due to different interference measures and advise for careful design in systems with high tag population. (FWAM11) shed light on the influence of multipath propagation for RFID localization approaches. They provide a multipath channel model and conducted simulations for several phase-based localization approaches and found that multipath has severe effects on the localization performance when not accounted for. (LAE+11) investigates on the bandwidth dependence of UHF RFID localization in multipath environments. Experimental Measurements are conducted in a warehouse portal with severe multipath environment. They come to the conclusion that, due to regulatory restrictions, channels in the ISM bands are not suited for severe multipath channels and suggest to use signals like Ultra Wideband with a larger bandwidth to overcome the multipath drawbacks.

3.2 Ultra Wideband

In contrast to RFID, where the name relates to the pursued application of identification by using radio frequency, Ultra Wideband (UWB) describes the signal itself that is used for this technology. The name directly indicates the bandwidth as the main parameter that comes into play for the definition. An UWB signal is defined to meet at least one of two requirements according to the Federal Communications Commission (FCC) (F+02). It has to have a fractional bandwidth higher than 20 % or an absolute bandwidth larger than 500 MHz. The absolute bandwidth B_{abs} given in equation (3.5) is defined by the range between upper and lower frequency of the $-10\,\mathrm{dB}$ emission points f_H and f_L respectively. The $-10\,\mathrm{dB}$ emission point describes the frequency where the signal strength is 10 dB lower than the maximum signal strength over the whole used spectrum. This can be visualized given the power spectral density over occupied frequency in figure 3.10.

$$B_{abs} = f_H - f_L \tag{3.5}$$

The fractional bandwidth B_{frac} is given in equation (3.6) and defined as the relation between absolute bandwidth B_{abs} and center frequency f_c of the UWB signal. The center frequency f_c in equation (3.7) is defined as the frequency in the middle of the signals occupied spectrum given by the upper and lower $-10\,\mathrm{dB}$ emission points.

$$B_{frac} = \frac{B_{abs}}{f_c} \tag{3.6}$$

$$f_c = \frac{f_H + f_L}{2} \tag{3.7}$$

Substituting (3.5) and (3.7) into equation (3.6) the fractional bandwidth B_{frac} can be ex-

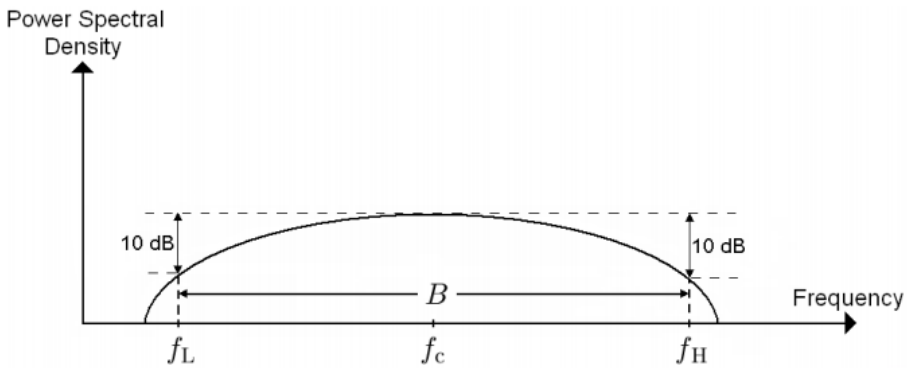

Figure 3.10: Schematic visualization of the power spectral density over frequency for an UWB signal. The upper and lower −10 dB emission points are indicated at the borders of the occupied spectrum. (GP09)

pressed as in equation (3.8), dependent only on the upper and lower −10 dB emission points.

$$B_{frac} = \frac{2(f_H - f_L)}{f_H + f_L} \tag{3.8}$$

The two requirements to meet the regulations for being an UWB signal by definition result in a minimum bandwidth only depending on the center frequency of the signal and the given fractional bandwidth in the lower part of the spectrum and the constant minimum absolute bandwidth for the upper part of the spectrum. The dependency is visualized in figure 3.11 providing the minimum required absolute bandwidth B_{abs} over center frequency f_c.

The high bandwidth used for an UWB signal results in a very short duration of the waveform. For communication the signals can be used as a continuous wave or a sequence of pulses. Using a short duration pulsed waveform is called impulse radio (IR) UWB (WS98). The transmitted pulse is often referred to as a monocycle. Figure 3.12 shows a second derivative of the Gaussian monocycle described in equation (3.9). Other monocycle shapes based on Gaussian pulse, Hermite polynomials or wavelet pulses can be found in (RMS98), (GSKP06) and (BEJH06) respectively.

$$\omega(t) = A\left(1 - \frac{4\pi t^2}{\zeta^2}\right)\exp(-2\pi t^2/\zeta^2) \tag{3.9}$$

To realize communication with short pulses used in IR UWB systems a number of those pulses is transmitted to convey information between UWB modules. One way to provide meaningful information is utilizing the sequence of polarities of pulses shown in figure 3.13.

Not only can information be encoded in the sequence of IR UWB signals but also each pulse itself comprises information of the traveled time between UWB modules. This fact can be exploited for localization purposes where the shortest traveled path of the UWB signal is deduced from the received signals time at the receiving antenna. Figure 3.14 shows

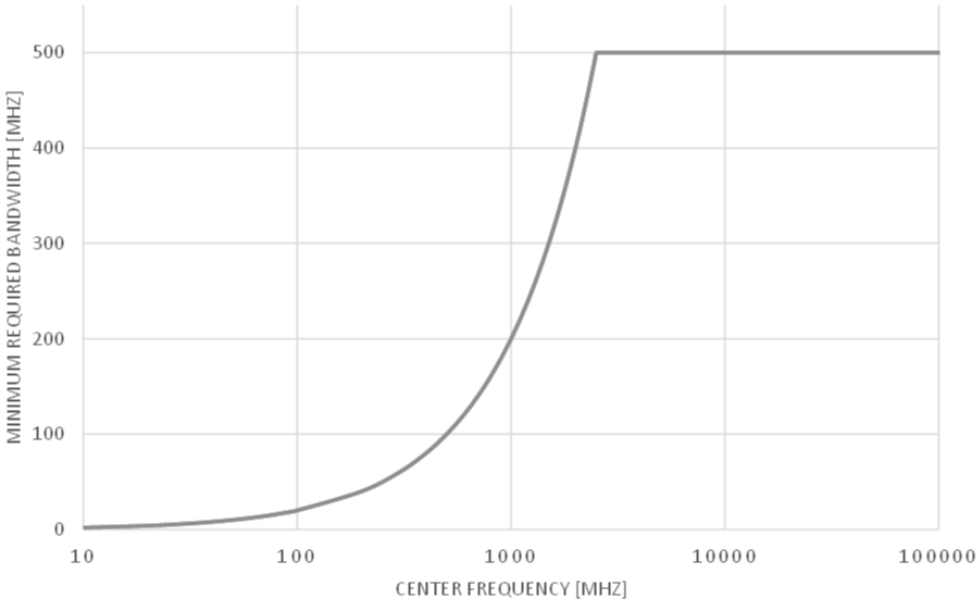

Figure 3.11: The UWB bandwidth requirement is defined by two functions that apply for different parts of the spectrum. Below 2.5 GHz the fractional bandwidth is the leading requirement. Above 2.5 GHz the minimum bandwidth is given by constant 500 MHz.

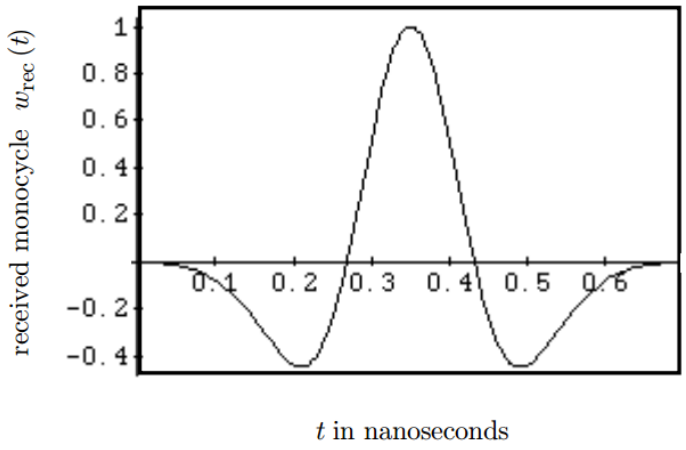

Figure 3.12: Amplitude of a second derivative of the Gaussian UWB monocycle over time. The pictured monocycle has a pulse width of about 0.7 ns. (WS98)

three scenarios of received IR UWB signals for different environmental effects. The first scenario visualizes one strong UWB signal in a direct line of sight situation where only minor multipath reflections occur. In this case it is sufficient to match the transmitted waveform with the one received at the UWB receiving antenna. In real world environment the response signal is overlayed by multipath reflections as shown in the second scenario. In this Case the strongest signal not necessarily represents the shortest path. It generates the need to be able to detect the first occurrence of a waveform independently from its amplitude by matching received signals with the expected waveform. The third scenario displays a signal additionally

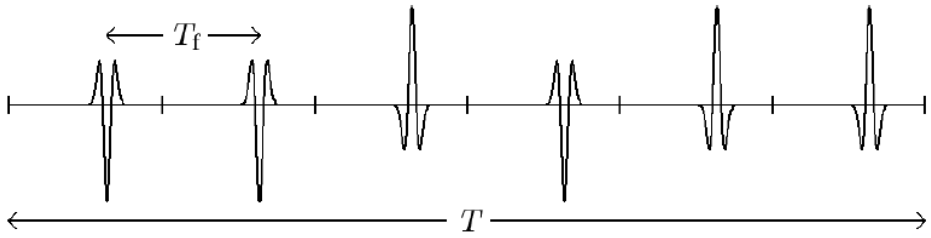

Figure 3.13: UWB signal consisting of short pulses with a low duty cycle, where T denotes the signal duration and T_f represents the pulse repetition rate. The polarization of each single pulse decodes one bit of information. (GP09)

disturbed by severe noise effects. Algorithms to detect the first arriving IR UWB signal can be found in (HS02), (GS05), (GSM$^+$05) and (YG05) respectively.

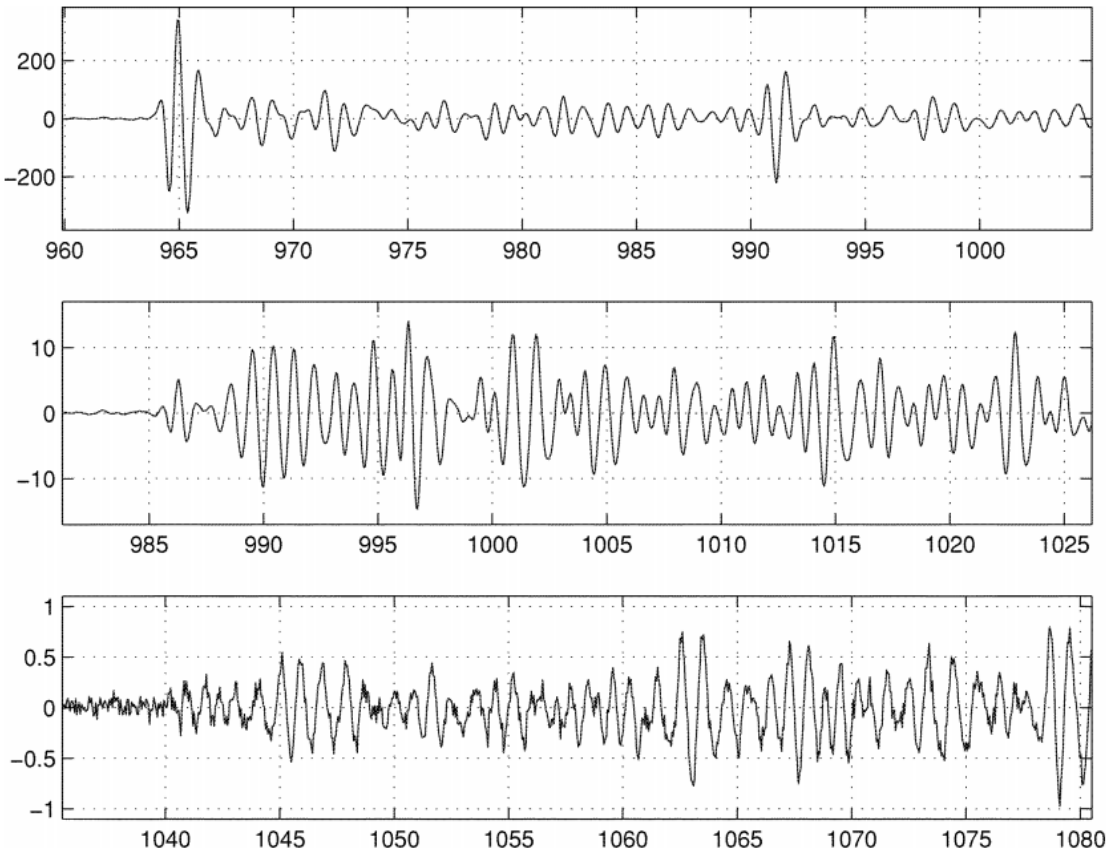

Figure 3.14: Examples of received IR UWB signals in three environment scenarios. The vertical axis provides the signal strength, whereas the horizontal axis indicates the time. In the first scenario a strong line of sight path is available for the signal to travel with only little noise and multipath signals. In the second scenario strong multipath signals occur at the receiving UWB module due to reflections caused by the environment. In a multipath scenario the direct line of sight signal is not necessarily the strongest signal received. The third scenario shows a received signal with strong noise influence and severe multipath signals received. (LS02)

3.2.1 UWB regulations

Another important aspect of UWB for localization purpose is the regulatory environment that significantly prescribes the permitted bandwidth, radiated power and potentially required mitigation techniques. Similar to the regulatory status for UHF RFID, the regulations for UWB are defined individually for a number of countries or alliances. Figure 3.15 provides an overview of the permitted usage of UWB bands between 3.1 and 10.6 GHz for selected countries. Each band represents 500 MHz of spectrum and is indicated by color whether it can be used with or without mitigation techniques implemented or is prohibited for UWB usage.

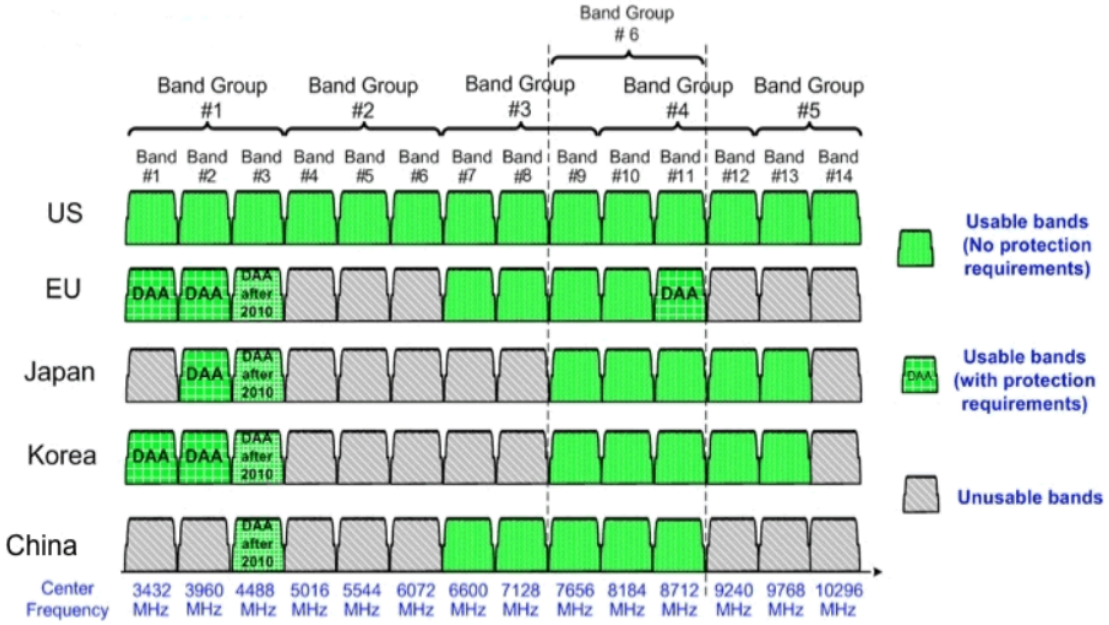

Figure 3.15: Overview of UWB regulations for selected countries over band group allocations based on table B.1. Permission to use one of the 14 UWB bands is indicated by color. Green describes UWB usage without mitigation techniques at −41.3 dBm. Green with text provides information on the required mitigation techniques to allow for an UWB usage with −41.3 dBm. Grey bands are restricted by very low power levels in the range of −53 dBm to −90 dBm dependent on the specific regulation for each country.

The first to come up with a regulation decision was the US administration FCC in 2002 with the first Report and Order in the matter of Revision of Part 15 of the Commission's Rules Regarding Ultra-Wideband Transmission Systems (F^+02). Figure 3.16 visualizes the FCC UWB mask from 800 MHz to 12 GHz and provides information on the upper limit for the allowed output power.

The FCC mask provides the most relaxed regulations worldwide with a frequency band from 3.1 to 10.6 GHz. The radiated power is limited to 41.3 dBm / MHz without any special mitigation technique required. This regulatory approach provides manufacturers of UWB systems with 7.5 GHz of continuous spectrum. In 2006 the ECC announced it's decision on UWB regulations for the EU. The ECC is part of the European Conference of Postal and

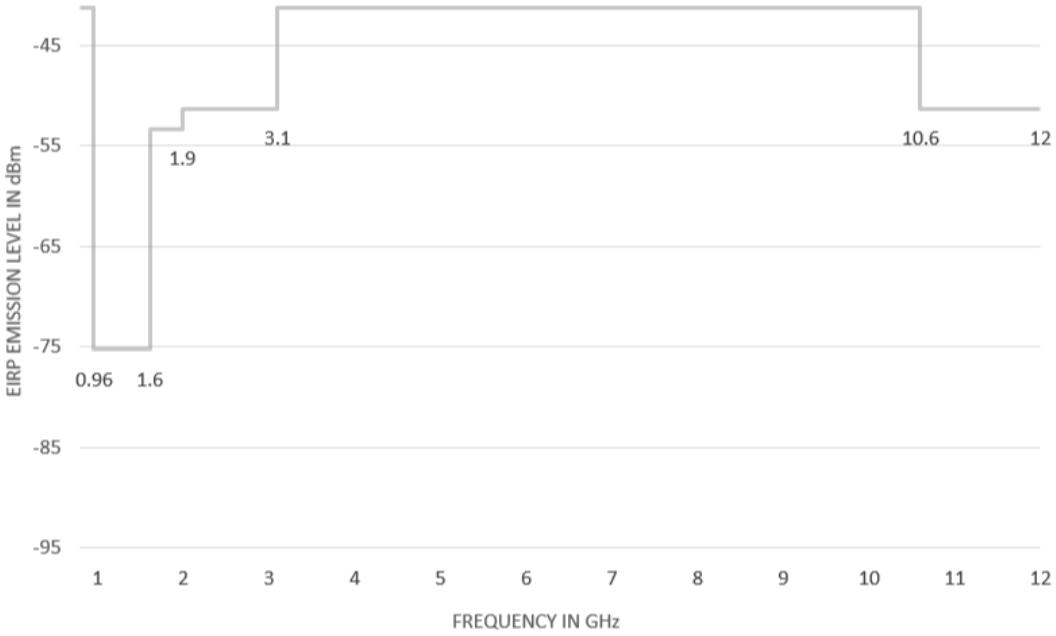

Figure 3.16: Regulatory mask for indoor UWB devices in the USA with a broad available frequency spectrum between 3.1 and 10.6 GHz without the need for mitigation techniques, based on table B.2.

Telecommunications Administrations (CEPT) and comprises 48 radio and telecommunications regulatory authorities of the CEPT member countries (Rah10). Regarding available spectrum for UWB systems, the ECC follows a more conservative approach than the FCC. Figure 3.17 shows the permitted mask for UWB systems in the EU.

It can easily be seen that the spectrum from 3.1 to 4.8 GHz is only available when required mitigation techniques are implemented. Using those techniques also enlarges the higher spectrum range by additionally making the band from from 8.5 GHz to 9 GHz available. To implement a Low Duty Cycle (LDC) as mitigation technique the following requirements have to be met.

- T_{on} max = 5 ms
- T_{off} mean $\geq$ 38 ms (averaged over 1 second)
- $\sum T_{\text{off}} >$ 950 ms per second
- $\sum T_{\text{on}} <$ 18 s per hour

Detect and Avoid (DAA) is described by the ECC to be a technique that continuously detects other radio systems in the nearby RF environment and assigns the power level of the detected signal to three zones depending on given signal detection thresholds. The proposed approach is to react to each zone, e.g. by switching to allowed power emission levels. In depth details can be found in table B.4.

Regulations in other countries adopt or closely align to the two implementations in the USA and Europe or modifications of them. Most countries are more strict with their allowed UWB

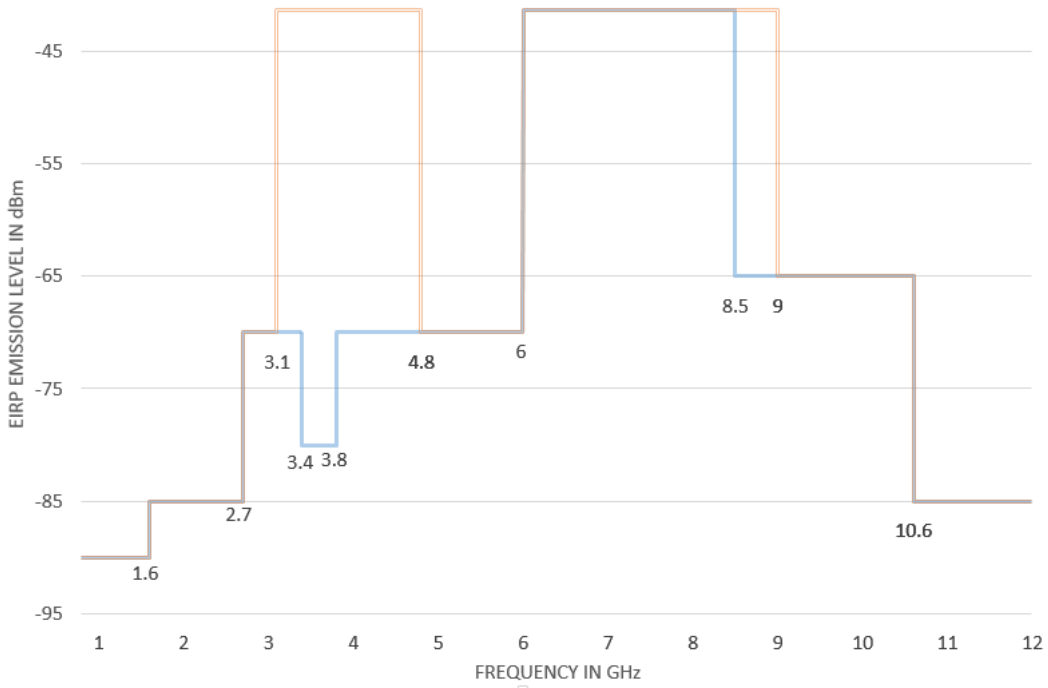

Figure 3.17: Regulatory mask for UWB devices in the EU with two graphs indicating the allowed radiated power levels based on table B.3. The blue graph describes the UWB mask applicable when no mitigation techniques are implemented. It provides a continuous spectrum of 2.5 GHz between 6 GHz and 8.5 GHz with −41.3 dBm allowed. The orange graph indicates the allowed emission levels when mitigation techniques like Low Duty Cycle (LDC) or Detect and Avoid (DAA) are implemented. Two separated regions with 1.7 GHz and 3 GHz of continuous spectrum are available with −41.3 dBm.

masks than the FCC. Mitigation techniques like LDC and DAA are also required in many countries to be permitted to use UWB systems at full power level. Examples for important regulations can be found in the annex figures B.1, B.2 and B.3. For manufacturers of UWB systems it is essential to find a frequency band or a range of bands that are permitted in all countries they want to use their systems in. From figure 3.15 can be seen that band #3 with center frequency of 4.488 GHz is available throughout all considered countries. A wider cross-country region is available from band #9 to #11 providing 1.5 GHz of continuous spectrum.

3.2.2 Available UWB localization systems

There is a growing interest in Ultra wideband (UWB) to realize accurate and precise localization for more than a decade (GTG+05). (SGK05) presents an UWB localization system with the focus on low-cost hardware. Experiments were conducted both in a laboratory environment and within an anechoic chamber. A mean error of 40 *cm* to 50 *cm* was achieved with a standard deviation of 43 *cm* to 55 *cm*. In (SRO06) a non-coherent IR-UWB demonstrator results in ±5 ns accuracy for 95 % of the cases. This leads to a range accuracy of

about 1.5 m. A two-way ranging approach with a pulse bandwidth of 1.5 GHz and resulting measurement accuracy of 260 ps or 3.9 cm is given in (FKML10). Fingerprinting approaches based on RSSI and Channel Impulse Response (CIR) are given in (WWB$^+$10) and (KS10). They provide position estimation errors of 0.33 m in an are of 1.2 m × 1.6 m and 4 cm in 6 fingerprinting regions of 28 cm × 28 cm respectively. Pietrzyk and von der Grün provide an UWB localization system with range estimation errors below 3 cm (PG10). (ÇNG$^+$12) presents a root mean square error (RMSE) of 7.4 cm in 2D for experiments in a 4.3 m^2 indoor environment with a ToA based UWB localization approach. (SPA$^+$14) conducts an experimental study scrutinizing an industrially available UWB positioning system positioned in a 60 m^2 industrial environment resulting in a 3D mean error and standard deviation of 0.4 m to 1.0 m and 5.4 cm to 8.0 cm, respectively. UWB localization experiments in a retail environment are presented in (CPMZ16). Measurements in a showroom environment with two UWB implementations lead to accuracy results of about 15 cm. In (TEW16) a UWB localization system based on TDoA ranging algorithms is provided and experimentally evaluated. 2D-Positioning results of a mobile robot are claimed to be under 20 cm most of the time.

To overcome the limitations of radio location systems one can fuse different sensor technologies like inertial sensors providing data on e. g. acceleration or angular velocity. Inertial sensors are prone to an integration drift over time to realize position and orientation data. This behavior restricts their usage in time for integrated results or to using the non-integrated values.
(SSGK08) uses a Kalman Filter to integrate UWB data and data from an inertial measurement unit (IMU). Experiments in a room of 4.8 m × 2.8 m with a moving person result in a RMSE of 320 mm.
(CCT08) combines an Ubisense UWB system with motion capturing based on inertial sensors. This results in an error of 140 mm for localizing a moving person for 3 m.

The combination of inertial sensors with a round-trip time (RTT)UWB positioning system using an extended Kalman Filter is shown by (DANS$^+$10). Experiments in an office resulted in a RMSE of 100 mm for a rectangular trajectory.

(HDL$^+$09) and (ZLZ$^+$13) provide qualitative graphical results for their tightly coupled approaches comprising UWB positioning and inertial measurements.

(KHS15) uses 10 UWB receiver and tightly couples them with IMUs. Experiments in an 8 × 6 × 2.5 m indoor environment give 30 mm, 30 mm and 23 mm RMSEs in x, y and z respectively.

There are several commercially available UWB localization system on the market. One of the first successful UWB positioning products is from Ubisense (Ubi17). It uses proprietary active tags that are battery powered and operate in the range of 6.5 to 8 GHz. The system uses TDoA and AoA algorithms to provide an overall accuracy of 15 cm. A second UWB localization product is Dart UWB by Zebra which uses a frequency range of 6.35 to 6.75 GHz and results in an accuracy better than 30 cm (Dar17). The PulsOn family by Time Domain

(Tim17) provides two implementations of UWB modules. The high-end version leads to range measurements with an accuracy of about 2 cm and a precision in the same range. The system uses a frequency range of 3.1 to 5.3 GHz for FCC and 3.1 to 4.8 GHz for ETSI regulations in the USA and Europe respectively. BeSpoon provides an UWB chip and a corresponding evaluation kit with ToA or TDoA ranging methods (BeS17). The UWB chip is claimed to cover the full FCC allowed frequency spectrum. Another UWB chip comes from Decawave and claims to reach an accuracy of under 10 cm (Dec17). (AMV16) presents an experimental validation of Decawave UWB modules in LOS and NLOS scenarios. It is very broad spread in the scientific community and often used as basis for products by various companies. Time Domain presented an UWB module implementing the Decawave DWM1000 chip in 2015. Quantitec combines the Decawave UWB module with inertial sensor data in their product Intranav and claims a ±3 cm accuracy (Qua17). There are several other partners of Decawave worldwide comprising Idolink in South Korea (Ido17), Redpoint Positioning in USA (Red17), Sewio in Czech Republic (Sew17) and Woxu in China (Wox17). In (JS16) two Decawave and Bespoon evaluation kits are compared in different measurement scenarios. Overall the Decawave UWB system leads to more accurate results in line of sight and non line of sight environments. The reported standard deviation in line of sight scenario is given with 11 cm for Bespoon and 5.5 cm for Decawave respectively.

3.3 Radio Technologies - Conclusions

Based on the thorough evaluation of RFID and UWB as two of the most promising radio technologies in the last two chapters and the desired goals of this thesis from chapter 2, a decision on the pursued radio type can be made. The combination of the required industrially available components and the desired localization accuracy to be able to develop beneficial applications suggests to prefer UWB over RFID. There are several UWB location products in the market with satisfying accuracy possibilities, whereas there are only few RFID products for radio location which provide poorer position estimation. Promising accuracies for RFID systems are only achieved in scientific demonstrators and not easily available for this thesis. In a collaboration with an RFID localization startup company we tried to look into more accurate RFID positioning. The pursued goal was promising but unfortunately did not lead to satisfying results.

Two other requirements are based on the dynamic, harsh and highly reflective medical environment and the need for line of sight. Both UWB and RFID radio location have an advantage over optical positioning systems when it comes to line of sight. Radio signals can penetrate more material than light which results in a robust line of sight for radio signals where optical light is already deteriorated or blocked. For medical environment it is crucial to consider the presence of shielded walls as well as numerous large devices in a crowded indoor environment. In such a highly reflective multipath environment the usage of broadband UWB systems covering gigahertz of spectrum over narrowband RFID is beneficial. With those very short UWB pulses it is possible to identify the first recognizable time of arrival

while neglecting signals arriving later due to reflections.

The power consumption including additional workflow improvement with passive components when there is no need to charge them and the costs of a localization system play a role when thinking ahead of this thesis. Here RFID, at least with passive transponders, has an advantage over UWB.

The worldwide regulations for bandwidth capacity is another important aspect when thinking one step ahead of the prototypal evaluation of the technology but looking into the possibility of developing a product based on this technology. UWB offers two interesting places in the frequency spectrum where usage is allowed almost all over the world. For UHF RFID it is needed to use at least two types of transponders since the frequency bands in the USA and Europe differ to much. The ISM band is already found out to be not applicable founded in possible interference due to the crowded frequency spectrum

When consolidating all the mentioned aspects, UWB is the option pursued in this thesis well-founded in its superiority over RFID for most requirements. The upcoming chapters on ranging and localization technologies will therefore mainly focus on UWB radio location.

4 Ranging Technologies

In this chapter four well-established ranging approaches for Ultra Wideband systems are introduced. In section 4.1 the received signal strength (RSS) is exploited based on the fact that electromagnetic signal attenuates proportional to the traveled distance. With the time based technique time of arrival (ToA), introduced in section 4.2, the duration of a signal traveling from sender to receiver is exploited. In section 4.3 a method using directional antennas or antenna arrays to estimate the angle of arrival (AoA) of an electromagnetic signal is described. One further technique to make use of the time of flight of a signal is Time Difference of Arrival in section 4.4.

4.1 Received Signal Strength

Every emitted radio signal is exposed to attenuation or signal pass loss due to propagation. This loss in signal strength can be translated into a function of the distance traveled by the emitted radio signal. When two radio location units, $unit_1$ and $unit_2$, are used in a range estimation setup the formula given in equation (4.1) represents the received signal strength P_2 at $unit_2$, where P_1 is the signal strength at $unit_1$, G_1 and G_2 give the antenna gain of each radio location unit in the direction of the signal sent and received respectively,the wavelength of the radio signal is represented by λ and the distance traveled by the signal is given by d.

$$P_2 = P_1 G_1 G_2 (\frac{\lambda}{4\pi d})^2 \tag{4.1}$$

It can easily be seen that the signal power decays with d^2 in an ideal environment with free-space propagation. The given equation represents a very specific path loss for an exemplary environment. Equation (4.2) introduces a factor n that characterizes the attenuation.

$$P_2 = P_1 G_1 G_2 (\frac{\lambda}{4\pi d})^n \tag{4.2}$$

(Rap09) gives the range for n with 1.6 to 1.8 in line of sight (LOS) indoor condition. For outdoor environment the factor ranges from 2 to 6. Other path-loss models like the attenuation factor model in equation (4.3) are empirically driven.

$$P_d = P_{d_o} + 20log_{10}(\frac{d}{d_0}) + \alpha d + FAF \tag{4.3}$$

The attenuation factor model uses a reference distance d_0 to describe the path loss P_d for the actual distance where α is a frequency channel attenuation factor and FAF represents the floor attenuation factor (LZHH12). With precise on-site adaption for the environment, RSS can give a good estimate for the range between two radio location units. However, once the propagation channel differs slightly, severe errors in range estimation can be made due to the influence of multipath fading or shadowing.

4.2 Time of Arrival

Time of Arrival or Time of Flight (TOF) techniques provide information about the distance traveled between sender and receiver. They makes use of the fact that an electromagnetic wave propagates with a constant velocity, the speed of light. Therefore with the given speed of light and the measured time of flight one can deduce the distance traveled as seen in equation (4.4).

$$v = \frac{s}{t}, with\ v = c\ and\ s = d\ \rightarrow d = c \cdot t \tag{4.4}$$

The TOA approach does not directly provide the time equivalent for the distance traveled, but the time of transmission comprising the time of flight between sensor nodes and the time of signal handling and transfer inside the UWB modules. Figure 4.1 gives an impression on the composition for ranging.

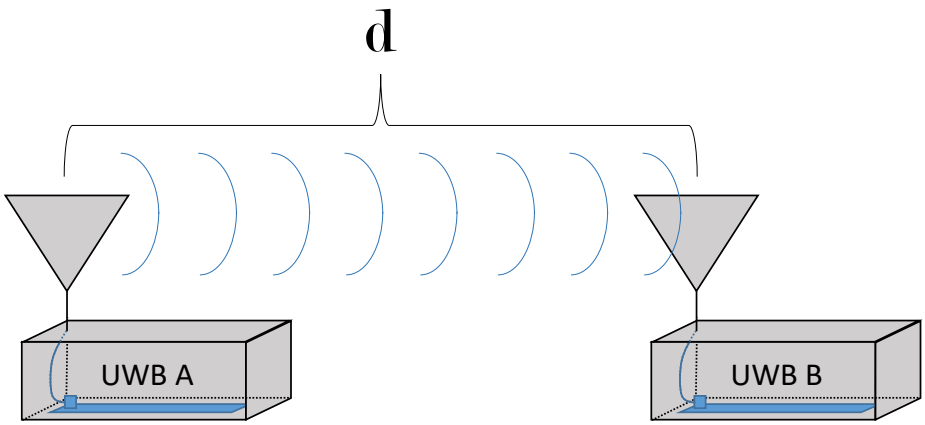

Figure 4.1: Time of Arrival setup with two UWB modules, A and B. UWB A sends a ranging request that is received by UWB B. In blue are highlighted the HF cable from Antenna to the connector on the electronic processing board and the connector and the electronic board itself. The distance between the UWB modules is described by d.

There are two types of TOA measurement schemes. The one way time of flight (OW-TOF) ranging method uses one UWB module as sender and one as receiver. For one way estimation of the time of flight, precisely synchronized clocks in the sensor nodes are required since one

nanosecond error in time converts to approximately 30 cm error in distance estimation. The UWB module that starts the range request sends a timestamp from the point in time in initializes the message to the receiving UWB node. Equation (4.5) gives an idea of parameters that influence the measured time.

$$t_{OW-TOF} = t_{distance} + t_{cable} + t_{process} \tag{4.5}$$

The goal is to extract the information of $t_{distance}$ from the measured time t_{OW-TOF}. Therefore parameters like the duration of the signal traveling from the antenna to the electronics for processing have to be calibrated or at least estimated based on e.g. the cable length. Figure 4.2 gives a schematic impression on the signal traveling between UWB modules to estimate the TOA in the OW-TOF setup.

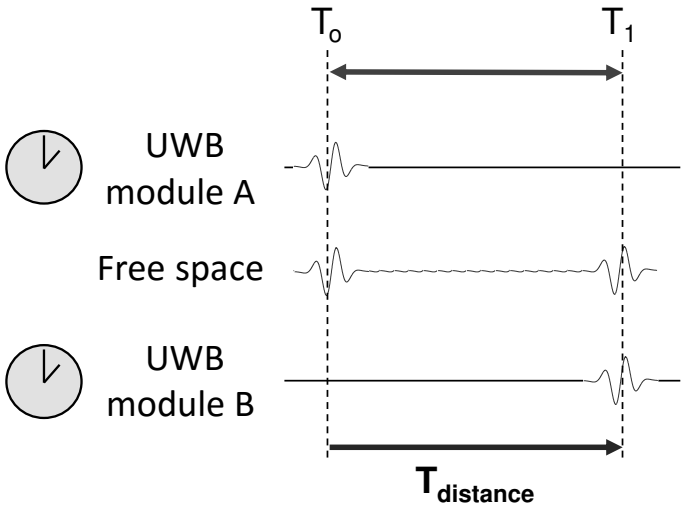

Figure 4.2: One way time of flight ranging scheme with sketched signal sequence at both UWB modules and in free space between the modules. The time consumed inside the receiving UWB module B is not part of this figure.

The second estimation scheme to compute the TOA between UWB modules is two way time of flight (TW-TOF) ranging. For this method the signal is not only sent from request UWB module to receiving module but processed there and sent back to the requesting UWB node. With this approach the distance between UWB modules is traveled twice. The main advantage over the OW-TOF approach is that there is no need for precisely synchronized clocks. Figure 4.3 gives an overview of the TW-TOF technique.

It can easily be derived that the total amount of time needed for a range measurement increases with TW-TOF. The time to travel the distance between nodes twice is one major influence on this gain. The resulting total time measured at UWB module A is sketched in equation (4.6).

$$t_{TW-TOF} = 2 \cdot t_{distance} + t_{reply} + t_{cable} + t_{process} \tag{4.6}$$

The parameter t_{reply} includes the times t_{cable} and $t_{process}$ when receiving the signal at UWB

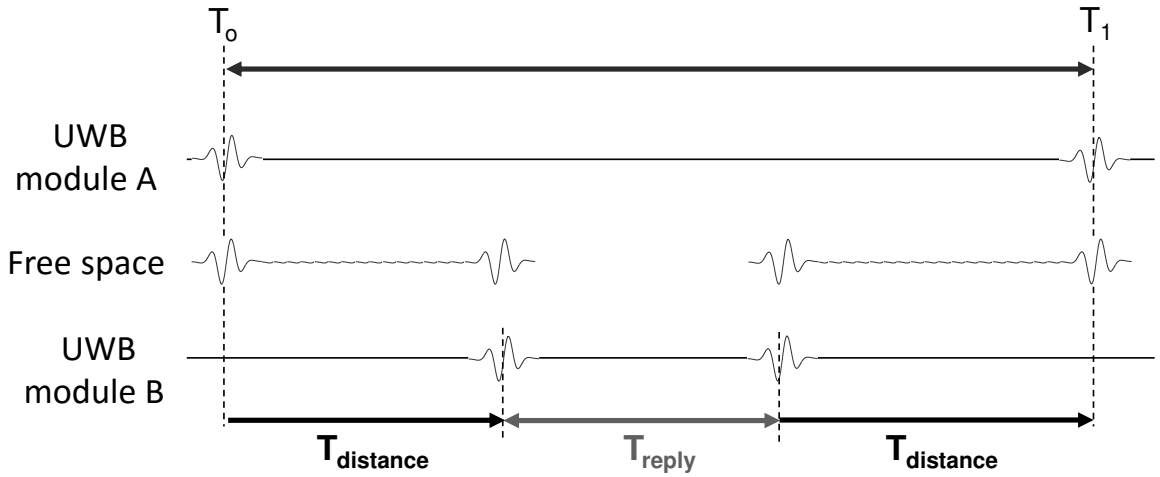

Figure 4.3: Two way time of flight ranging scheme with sketched signal sequence at both UWB modules and in free space between the modules. The time inside UWB module B to receive, process and transmit the signal again is given by parameter T_{reply}. The time consumed inside the receiving UWB module A is not part of this figure.

modul B plus the time for sending the signal back to UWB module A. The information on t_{reply} is sent back to UWB A with the ranging answer to be able to compute the sheer time of flight for the round-trip.

Assume the received impulse radio UWB signal to be described by the simplified example in equation (4.7), where τ reflects the time of arrival (TOA), s represents the signal template, and η is a Gaussian white noise with zero mean and a spectral density of $N_0/2$.

$$r(t) = s(t - \tau) + \eta(t) \tag{4.7}$$

A simple correlation algorithm searches for the largest value of correlation between $r(t)$ and a signal template $s(t - \hat{\tau})$ and results in $\hat{\tau}$ representing the TOA. To visualize the relation between UWB signal bandwidth and reachable range estimation the Cramer Rao lower bound (CRLB) can be calculated by equation (4.8) (GP09), where $\hat{\tau}$ is the TOA estimate, SNR is the signal to noise ratio, and β is the effective signal bandwidth. The achievable ranging accuracy over the SNR for different bandwidths based on the CRLB is shown in figure 4.4.

$$\sqrt{Var(\hat{\tau})} \geq \frac{1}{2\sqrt{2\pi}\sqrt{SNR}\beta} \tag{4.8}$$

It can easily be seen that the available bandwidth as well as the reachable SNR have an immense influence on the achievable ranging accuracy. For good SNR situations a ranging accuracy in the low cm up to millimeter range is achievable based on theoretical limits.

TOA or TOF methods are widely used in academic and commercially available UWB prototypes and products. Crucial tasks are the calibration of the system due to time delays

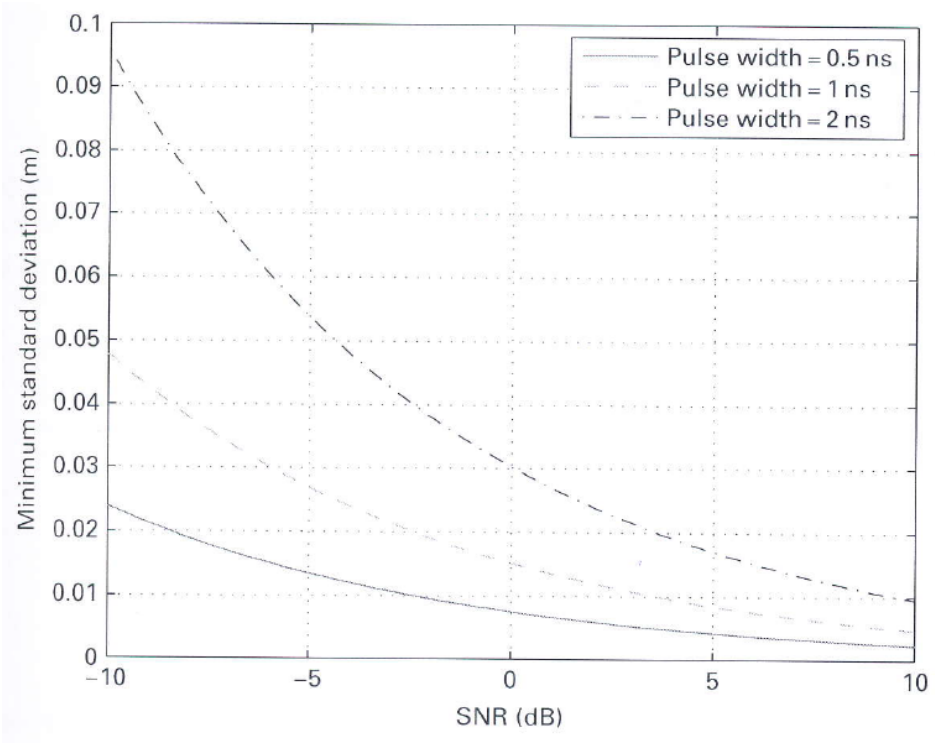

Figure 4.4: Cramer Rao lower bound for IR UWB Time of Arrival ranging scheme. It provides the minimum standard deviation over the SNR for three exemplary bandwidths or pulse widths. (GP09)

for the signal traveling through cables and the signal processing and to distinguish between the right and first signal representing the shortest path between UWB modules and reflected multi-path signals.

4.3 Angle of Arrival

Unlike RSS and ToA, Angle of Arrival does not result in a distance measure to represent ranging, but yields information on the direction of a signal incoming. To realize the angle information, antenna arrays can be employed that comprise of at least two antenna elements with known geometric proportions with respect to the array center. For each antenna element in the array, the time of arrival or the RSS can be estimated. By exploiting the differences between the used measures at each antenna element the angle of arrival can be calculated. The basic principle of AoA localization works for RFID the same way as for UWB. (ZZM11) provides an AoA setup with UHF RFID exploiting the phase of the received waves. (KKL$^+$11) implemented AoA measurements in a UHF RFID phased array with electronic beam steering mechanism. Figure 4.3 gives a 2D example for an antenna array with known geometry and an incoming signal. It can be assumed that the incoming signal resembles a planar wave-front since the signal source is sufficiently far away.

From figure 4.3 one can easily derive equation (4.9) with l being the spacing between two

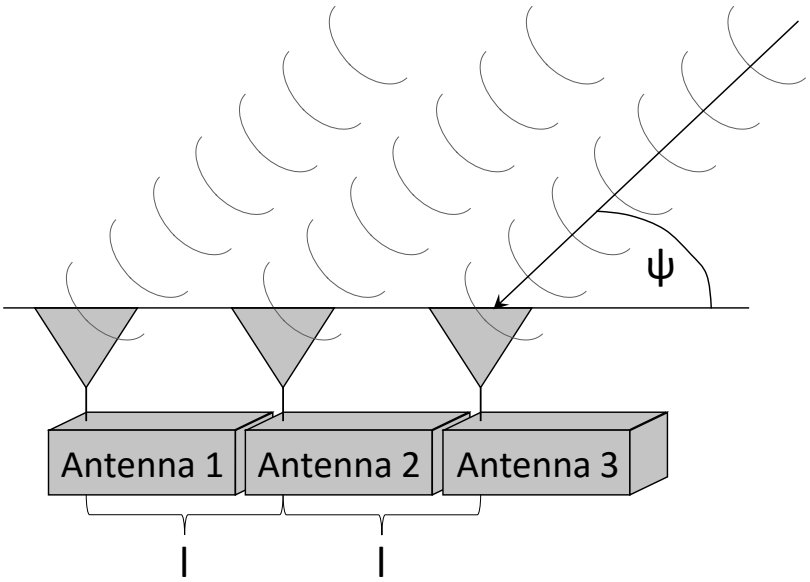

Figure 4.5: Angle of Arrival for an equidistant antenna array with three antennas and the spacing l between them. Parameter ψ denotes the angle of arrival of the request signal. The setup could also comprise more than one antenna on an UWB module or a two-dimensional array. This depends on the used hardware.

antenna elements, ψ the AoA and c the speed of light.

$$l = \sin(\frac{\psi}{c}) \tag{4.9}$$

The AoA can also be estimated for 3D ranging information with a two dimensional antenna array as prerequisite. Since two lines in 3D can be skew-whiff and therefore do not necessarily intersect like two lines in 2D, the corresponding system of equations does not necessarily have one single solution. With this over-determined system one can try to estimate the measurement error.

Analogous to ToA, assume the received IR UWB signal to be described by the simplified example in equation (4.10) for $i = 1, \ldots, n$, where n is the number of antenna elements, τ_i reflects the time of arrival (ToA) at the ith antenna element, s represents the signal template, and η_i is a Gaussian white noise with zero mean and a spectral density of $N_0/2$ at the ith antenna element.

$$r_i(t) = s(t - \tau_i) + \eta_i(t) \tag{4.10}$$

According to (GP09) the CRLB for AOA methods can be calculated with equation (4.11) and results in figure 4.6.

$$\sqrt{Var(\hat{\psi})} \geq \frac{\sqrt{2}c}{\sqrt{2}\pi\sqrt{SNR}\sqrt{n(n^2-l)}l\cos\psi} \tag{4.11}$$

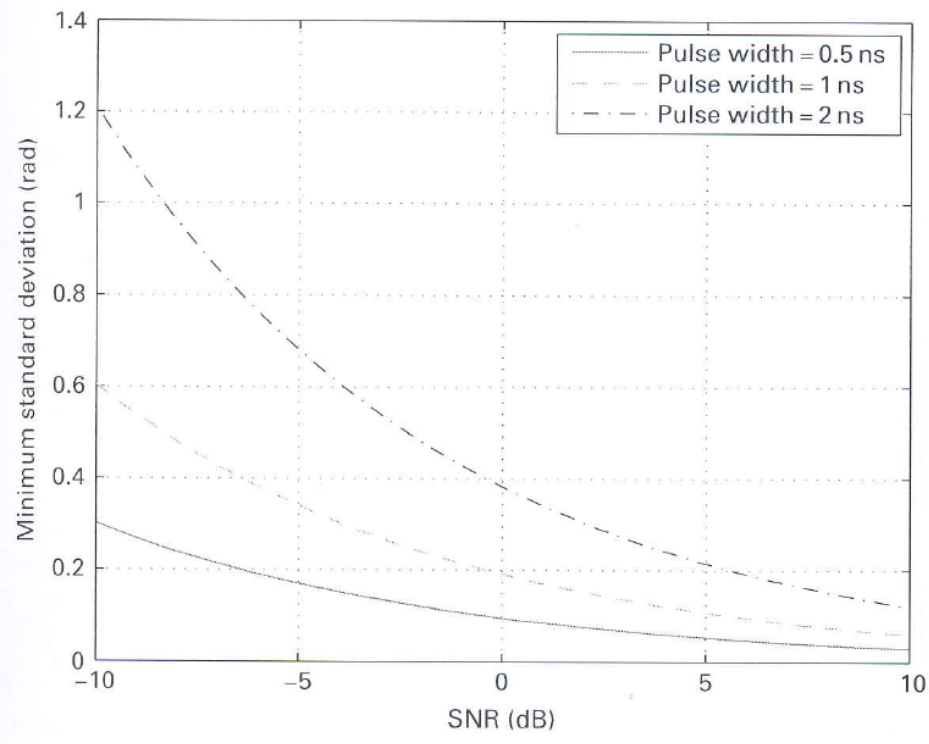

Figure 4.6: Cramer Rao lower bound for IR UWB Angle of Arrival ranging scheme. It provides the minimum standard deviation over the SNR for three exemplary bandwidths or pulse widths. (GP09)

The achievable accuracy for AoA techniques is influenced by the available bandwidth and the reachable SNR. Compared to the ToA approach the theoretically achievable accuracy for good SNR conditions lies one magnitude below, at only decimeter to centimeter range.

4.4 Time Difference of Arrival

The Time Difference of Arrival (TDoA) approach provides information on the time difference of signals arriving between one UWB module to be localized and UWB reference nodes. Like ToA, it also makes use of the fact that the distance between nodes directly corresponds to the time an electromagnetic signal needs to travel this distance. TDoA requires precisely time synchronized UWB reference modules like the OW-TOF method from section 4.2. Opposite to that approach, the mobile UWB module does not need to have a synchronized clock with the other UWB modules. There are two different approaches of signal flow for TDoA, the central and peripheral one that are shown in figure 4.7.

To better understand the signaling flow, figure 4.8 clearly shows what information is needed for the TDoA arrival approach and what information can be discarded.

The total time of flight of the ranging signal is not of interest for this approach. Therefore, an arbitrary reference time T_0 can be chosen. The outcome of interest is given in equation (4.12).

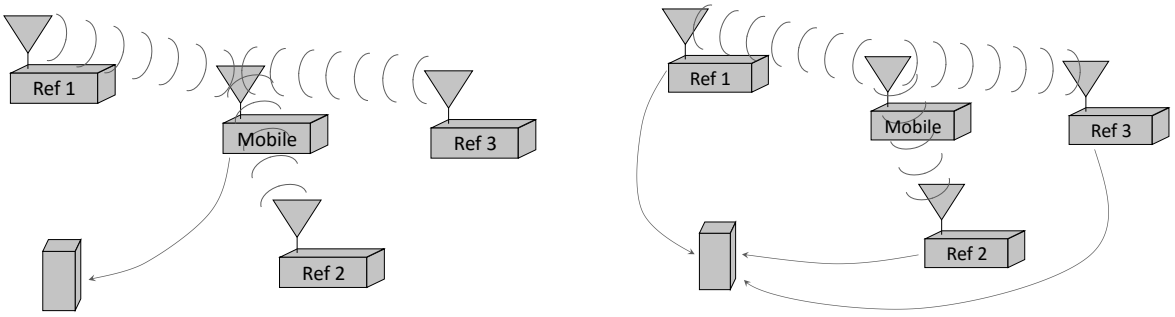

(a) Central approach (b) Peripheral approach

Figure 4.7: Time Difference of Arrival signaling approaches. With the central approach the mobile UWB node receives ranging request signals from each UWB reference module with a corresponding timestamp. The collected data is provided to a processing station that can also be integrated into the mobile UWB node. For the peripheral approach the mobile UWB node sends a ranging request that is received by all UWB reference modules. The measured time of receiving the signal is send to a processing station.

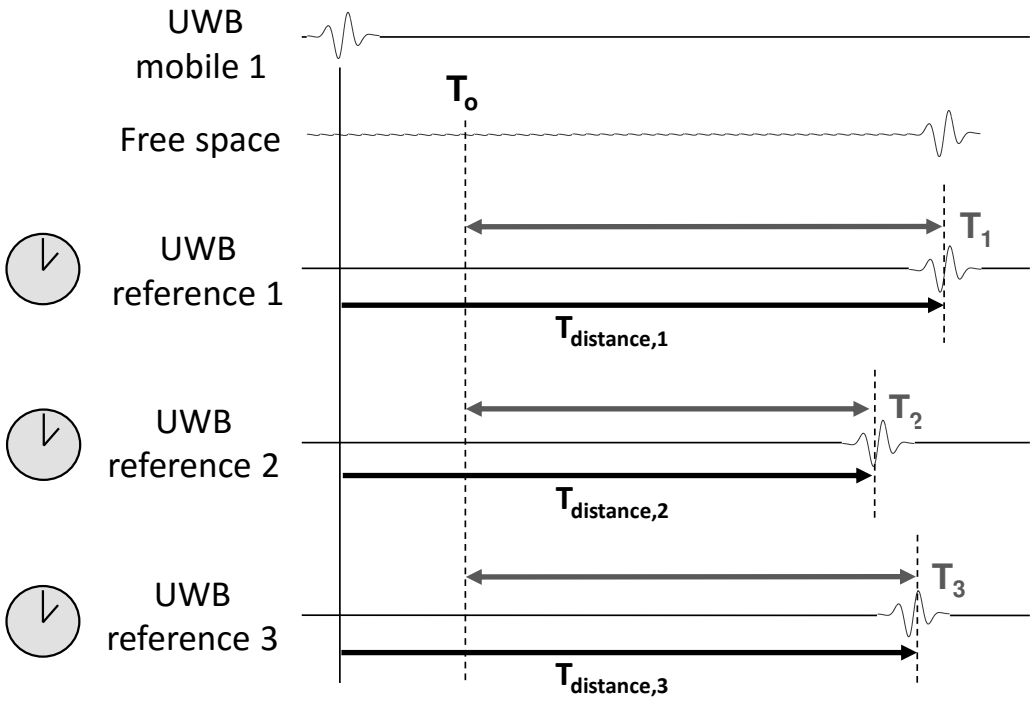

Figure 4.8: Time Difference of Arrival ranging scheme with a peripheral approach and one mobile UWB node sending the range request to the reference nodes. The reference UWB nodes need to be precisely synchronized and receive the signal depending on the distance traveled between each pair of nodes. T_0 describes an arbitrary point in time that is used as reference point.

$$T_{1-2} = T_1 - T_2,\ T_{1-3} = T_1 - T_3 \ and\ T_{2-3} = T_2 - T_3 \tag{4.12}$$

These time differences give information which UWB reference node is located nearer or farther away from the mobile UWB node. A time difference of 0 means that the mobile UWB node lies directly in the middle between the corresponding two reference modules.

The TDoA ranging scheme, comparable to ToA, is widely used in academic and industrial implementations. For instance, the global positioning system (GPS) makes use of this approach with having synchronized satellites in space that provide ranging signals in a central TDoA approach.

5 Localization Technologies

This chapter comprises three well-known localization techniques for ranging systems like UWB. They all make use of one or the other ranging result from the methods introduced in chapter 4. In section 5.1 we shed a light on the angle based triangulation approach. Trilateration and Multilateration are two well-known localization methods. In literature trilateration is often associated with absolute range based sensor data, whereas it is spoken of multilateration when range differences are obtained. This is misleading since the prefixes „tri“ and „multi“ give an information on the number of available signals for the calculation and not for the type of range information. In this thesis it will be spoken of trilateration when three references are given and multilateration when there are at least four reference nodes. It will be further divided into spherical algorithms based on absolute range measurements and hyperboloidal algorithms based on range difference measurements. Section 5.2 describes a spherical trilateration approach in 5.2.1 and a spherical multilateration algorithm in 5.2.2. One further localization technique that makes use of a hyperboloidal method is introduced in section 5.3.

5.1 Triangulation

Having a sensor setup that provides angular measurements or estimates often results in the use of triangulation to realizes meaningful localization information. Triangulation is based on the idea that by knowing the baseline between two measurement points and the corresponding angle information from theses points to the point of interest, the position of this point of interest can be deduced. Figure 5.1 gives an idea on how the triangulation approach works with two measurement nodes and one node of interest in a 2D environment.

To find a very easy geometric solution for the triangulation method one can define the first UWB reference node as origin of a coordinate frame. The second reference module is positioned in a distance of l_{base} in x-direction. The distance from the reference nodes to the mobile UWB module can be seen as legs of a triangle. Mathematically they can be represented in point-slope form as given in equation (5.1).

$$y - y_p = m_p \cdot (x - x_p), \text{with } (x_p, y_p) \text{ denoting one point p on the line} \tag{5.1}$$

We set x_1 and y_1 to 0 for the first reference node and deduce the slope m from the angle of arrival ψ_1 using equation (5.2).

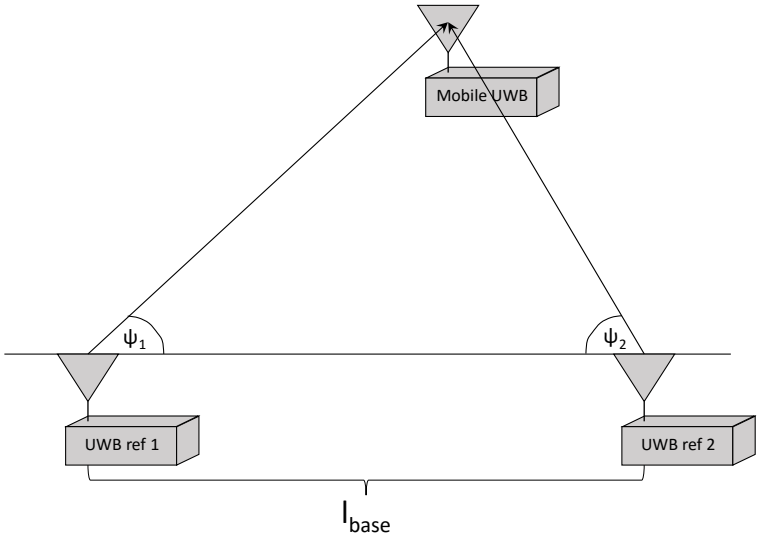

Figure 5.1: Schematic representation of the triangulation method in a 2D scenario with two UWB reference modules at known distance l_{base} to each other. From each reference node the angles ψ_1 and ψ_2 to the mobile UWB module are known from an AOA approach. With these three information the position of the mobile UWB node can be computed.

$$\tan \psi_p = m \tag{5.2}$$

For the second reference node, x_2 is represented by l_{base} and y_2 is 0. Combining these information results in equation (5.3) for the x-component of the intersection of the lines where the mobile UWB module is located.

$$x = -\frac{\tan \psi_2 \cdot l_{base}}{\tan \psi_1 - \tan \psi_2} \tag{5.3}$$

The y-component can easily be deduced from the point-slope equation in (5.1) used for one of the legs of the triangle. It can be seen that for the 2D case two angular measurements from two reference nodes are needed. To find a triangulation solution in 3D at least three reference stations are required. Unlike the 2D case the lines do not always intersect in the 3D case. Due to measurement noise the lines will most likely be skew and therefore do not allow for one single position solution. To solve for a 3D case, a least squares solution can be found to solve this overdetermined system of equations.

5.2 Spherical Tri- and Multilateration

Spherical lateration is a mathematical approach to provide position information from range measurements. In our setup it could take results form RSS or TOA ranging technologies as input. By using the geometry of circles in 2D or spheres in 3D and the intersections between

them, the position of an object can be estimated. Figure 5.2 shows a setup of 3D localization with two spheres intersecting in a circle. The position of the object to be estimated can be located anywhere on the circle and has to be further specified by more range measurement inputs resulting in more spheres.

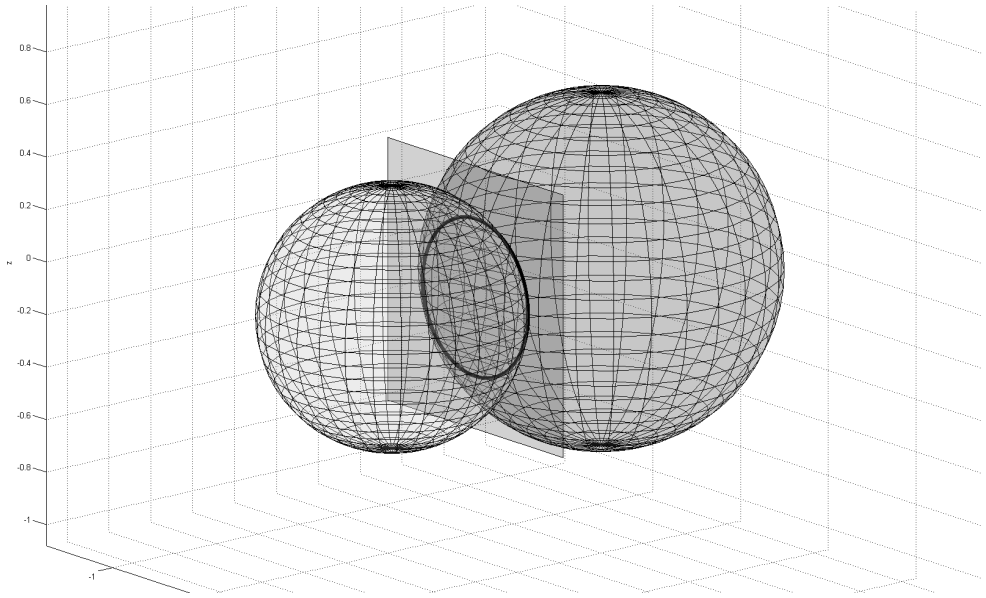

Figure 5.2: Schematic representation of the spherical lateration method in a 3D scenario with two spheres representing range measurements from two sensors. With these information the position of the mobile UWB node can be computed to be located on the highlighted circle that results from the two spheres intersecting.

To find a unique position in 3D, four reference modules are needed. Two spheres intersect in a circle that intersects with the third sphere in two points. The fourth sphere intersects with one of these two points. It is also possible that the third sphere and the circle intersection from the first two spheres only intersect in one point. In this special case, the fourth sphere only confirms the position estimation.

A system with overall four UWB modules would be under-determined, since only three UWB modules can be used as references and therefore the last step of finding the proper intersection of the remaining two candidates can not be provided. This is called trilateration. In section 5.2.1 a geometric approach for a trilateration situation with three reference nodes is introduced. Section 5.2.2 points out an algorithm for a well-determined or multilateration scenario with at least four reference nodes.

5.2.1 Spherical Trilateration

In the under-determined or trilateration scenario two solutions are obtained. To get the valid position solution, plausibility measures have to be implemented. This can work in the way that one solution always is outside of the volume of interest. Figure 5.3 shows a 2D setup of four UWB nodes with three of them used as references and one as localization object.

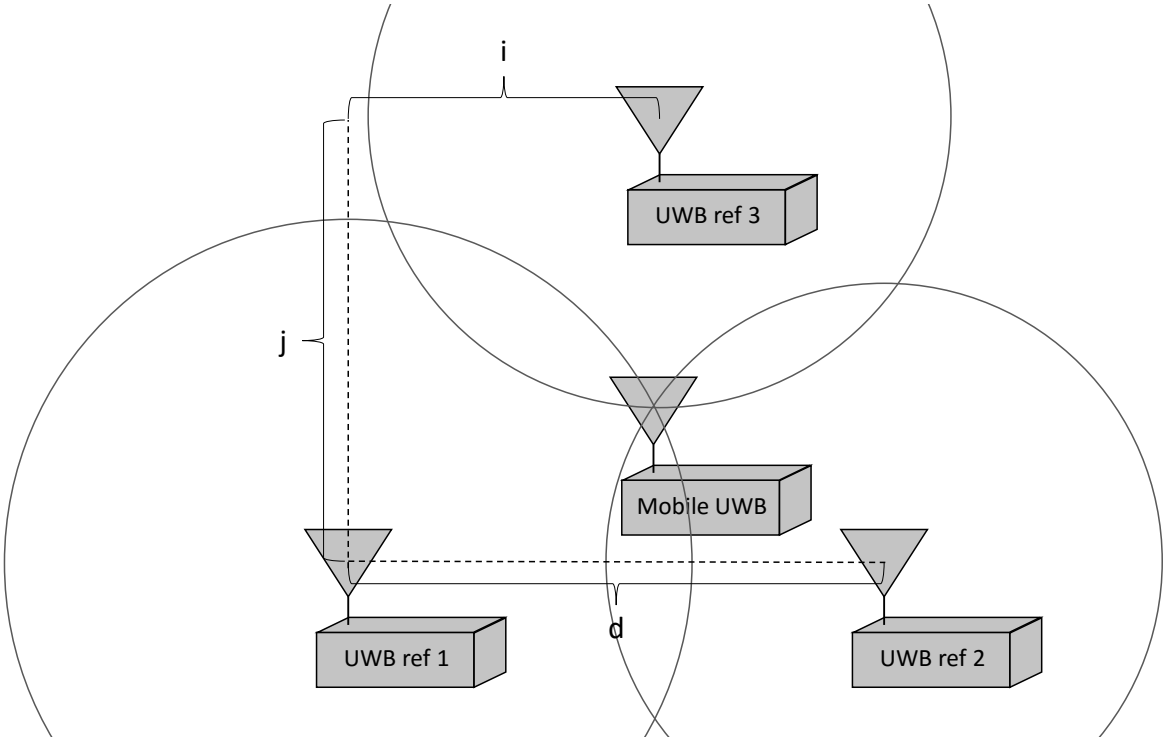

Figure 5.3: Schematic representation of the spherical trilateration method in a 2D scenario with three UWB reference modules at known positions. The location of the mobile UWB node can be derived from the ranging information of the reference nodes. The variables d, i and j give relative distances regarding the first reference nodes which is situated in the point of origin.

The presented algorithm based on spherical trilateration is not unambiguous. With three reference modules in a 3D setup it results in two solutions for the location of the mobile UWB node. We can use the location of the reference nodes for a plausibility check. Assuming ceiling mounted UWB reference modules, they form a plane that lies approximately in parallel to the ceiling. One result of the equation lies above and one below this plane. Therefore, the solution outside the room can be neglected. Three UWB reference nodes (UWB ref 1, 2 and 3) result in three equations for the corresponding spheres, where r denotes the range from reference node to mobile node and therefore the radius of the sphere, and the distance variables shown in figure 5.3:

$$r_1^2 = x^2 + y^2 + z^2 \tag{5.4}$$

$$r_2^2 = (x - d)^2 + y^2 + z^2 \tag{5.5}$$

$$r_3^2 = (x - i)^2 + (y - j)^2 + z^2 \tag{5.6}$$

Rearranging (5.4) and (5.5) leads to:

$$x = \frac{r_1^2 - r_2^2 + d^2}{2d} \tag{5.7}$$

Some further rearrangement based on (5.4) and (5.6) leds to:

$$y = \frac{r_1^2 - r_3^2 + i^2 + j^2 - 2ix}{2j} \tag{5.8}$$

Using equation (5.4) one can find:

$$z = \pm\sqrt{r_1^2 - x^2 - y^2} \tag{5.9}$$

The location of the mobile UWB node is represented by the intersection (x, y, z) of the three spheres.

5.2.2 Spherical Multilateration

The spherical multilateration scenario is defined by the availability of at least four reference nodes that contribute to localize a mobile UWB node. The introduced approach to solve this spherical multilateration problem is derived from (SPA+14). With four reference nodes at known positions, the sphere equations are represented in (5.10) i denotes the index of the reference node.

$$(x - x_i)^2 + (y - y_i)^2 + (z - z_i)^2 = r_i^2 \tag{5.10}$$

The estimated position of the mobile UWB node is given by (x, y, z), where (x_i, y_i, z_i), $i = \{1, 2, 3, 4\}$ represent the reference node positions and r_i represents the range from mobile node to reference node. These four equations can be reformulated to fit into a linear system of equations represented in (5.11).

$$\mathbf{Ax} = \mathbf{b} \tag{5.11}$$

The reformulation leads to the explicit representation in (5.12) and (5.13).

$$\mathbf{A} = 2\begin{bmatrix} (x_n - x_1) & (y_n - y_1) & (z_n - z_1) \\ (x_n - x_2) & (y_n - y_2) & (z_n - z_2) \\ \vdots & \vdots & \vdots \\ (x_n - x_{n-1}) & (y_n - y_{n-1}) & (z_n - z_{n-1}) \end{bmatrix} \tag{5.12}$$

$$\mathbf{b} = \begin{bmatrix} r_1^2 - r_n^2 - x_1^2 - y_1^2 + x_n^2 + y_n^2 - z_1^2 + z_n^2 \\ r_2^2 - r_n^2 - x_2^2 - y_2^2 + x_n^2 + y_n^2 - z_2^2 + z_n^2 \\ \vdots \\ r_{n-1}^2 - r_n^2 - x_{n-1}^2 - y_{n-1}^2 + x_n^2 + y_n^2 - z_{n-1}^2 + z_n^2 \end{bmatrix} \tag{5.13}$$

This system of linear equations can be solved by finding the least square solution for $\mathbf{x}$ subject to $\mathbf{Ax} = \mathbf{b}$. With equation (5.14) the minimum residual for the provided set of linear

equations can be found. The corresponding position $\mathbf{x}$ represents the least square solution.

$$min \left\| r \right\|_1 = \left\| \mathbf{Ax} - \mathbf{b} \right\|^2 \tag{5.14}$$

To calculate position $\mathbf{x}$ of the mobile UWB module, equation (5.15) can be used.

$$\mathbf{x} = (\mathbf{A}^T\mathbf{A})^{-1}\mathbf{A}^T\mathbf{b} \tag{5.15}$$

This approach can be extended to any number of reference modules in a spherical multilateration scenario with this mathematical formulation.

5.3 Hyperboloidal Trilateration

To handle time or range difference results from a sensor system, hyperboloidal lateration is an appropriate mathematical approach. It is comparable to spherical techniques in a sense that it combines range measurement results from several sensor inputs and combines them to calculate a position information. It differs in the underlying information from the sensors. Whereas spherical approaches make use of absolute range information, hyperboloidal techniques work with range differences regarding a pair of reference stations and the mobile module to be located. This results in different geometric forms that represent the position of the mobile node. Figure 5.4 shows the underlying principle with range differences that provide a hyperbola in a $2\,D$ environment.

Following (Fan90), Hyperboloidal problem formulation can be solved by finding hyperbolas and intersecting them. Figure 5.5 shows a hyperboloidal solution with three reference nodes in a $2D$ scenario. Reference module 1 is placed in the origin of the coordinate frame. Reference node 2 is positioned along the x-axis. The y-axis is orthogonal to these two modules. Variables d, i, j represent the position of UWB ref 2 and 3, whereas $t_{k,l}$ represent the hyperbola between reference node k and l.

With v representing the signal velocity and $r_{k,l}$ the range difference between node k and l, one can write:

$$\sqrt{x^2+y^2+z^2} - \sqrt{(x-d)^2+y^2+z^2} = \Delta t_{1,2} * v = r_{1,2} \tag{5.16}$$

$$\sqrt{x^2+y^2+z^2} - \sqrt{(x-i)^2+(y-j)^2+z^2} = \Delta t_{1,3} * v = r_{1,3} \tag{5.17}$$

Rearranging equation (5.16) and (5.17) one obtains:

$$r_{1,2}^2 - d^2 + 2d * x = 2r_{1,2}\sqrt{x^2+y^2+z^2} \tag{5.18}$$

$$r_{1,3}^2 - (i^2+j^2) + 2i * x + 2j * y = 2r_{1,3}\sqrt{x^2+y^2+z^2} \tag{5.19}$$

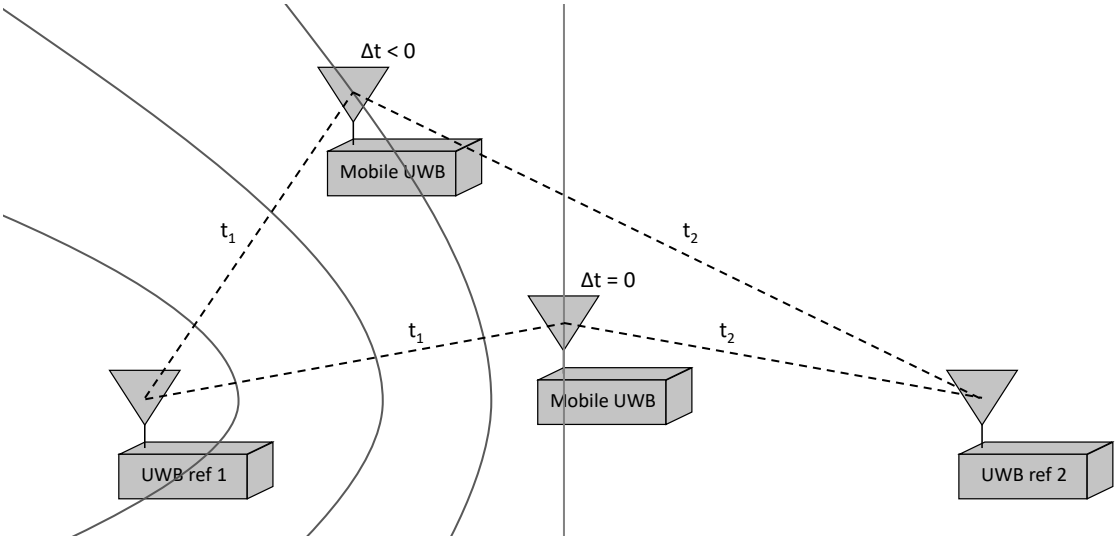

Figure 5.4: Schematic representation of the hyperboloidal working principle in a 2D scenario with two UWB reference modules at known positions and two representations of a mobile module to be localized. The variables t_1 and t_2 represent times of distance traveled from reference node to mobile node. This information is only given for a better understanding and is not directly needed for this approach. With the range difference information corresponding to Δt, the position of the mobile UWB node on a specifically shaped and positioned hyperbola can be computed.

Equation (5.18) and (5.19) represent two hyperboloids in $3D$. The intersection of those leads to a specific curve on a plane. Applying some reformulation as stated in (Fan90) one can obtain a plane equation (5.20):

$$y = g * x + h, \text{ where} \tag{5.20}$$

$$g = \frac{r_{1,3} * (d/r_{1,2}) - i}{j} \tag{5.21}$$

$$h = \frac{(i^2 + j^2) - r_{1,3}^2 + r_{1,3} * r_{1,2}(1 - (d/r_{1,2})^2)}{2j} \tag{5.22}$$

Substituting (5.20) into (5.18) leads to:

$$z = \pm\sqrt{s * x^2 + t * x + u}, \text{ where} \tag{5.23}$$

$$s = -(1 - (d/r_{1,2})^2 + g^2) \tag{5.24}$$

$$t = d * (1 - (d/r_{1,2})^2) - 2g * h \tag{5.25}$$

$$u = r_{1,2}^2/4 * (1 - (d/r_{1,2})^2)^2 - h^2 \tag{5.26}$$

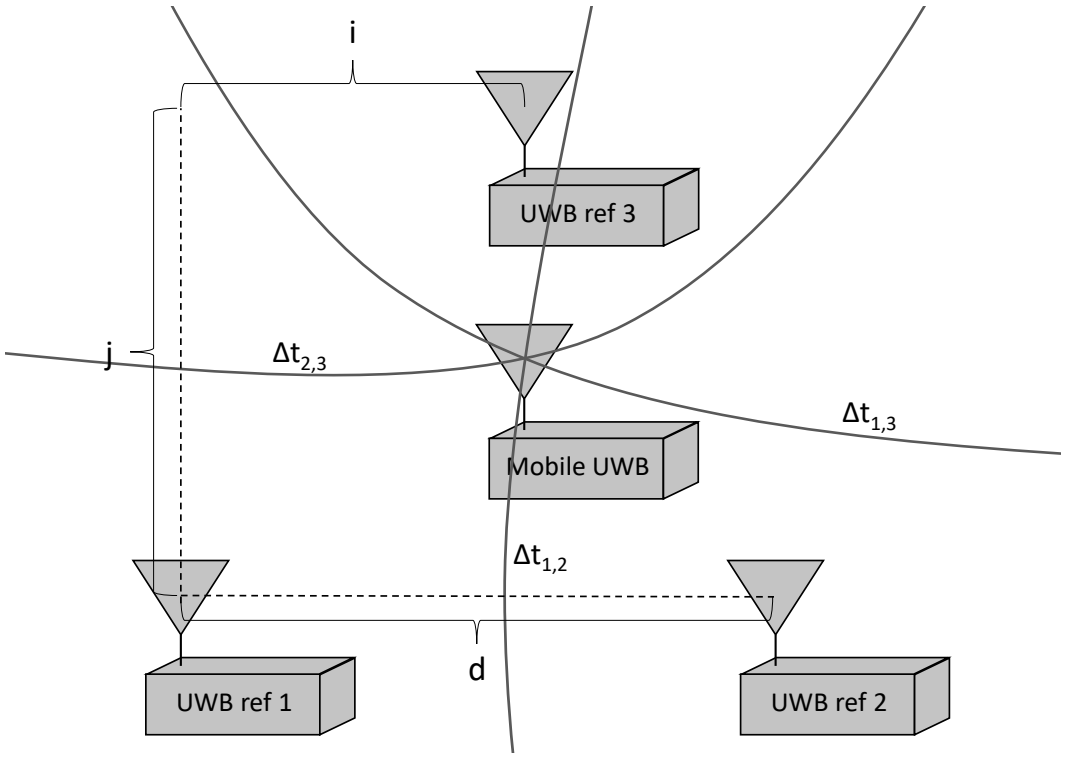

Figure 5.5: Schematic representation of the hyperboloidal position estimation in a 2D scenario with three UWB reference nodes at known positions and a mobile node to be located. With the range difference information of the mobile module between these three reference modules, the location of the mobile UWB node on the cross section of the corresponding three hyperbola can be computed. The variables $t_{k,l}$ represent the hyperbola between reference node k and l. In an ideal $2D$ scenario the hyperbola intersect in one single point.

Combining the formulations from equation (5.20) and (5.23) a vector representation of the mobile node only depending on one unknown variable can be found:

$$\begin{pmatrix} x \\ y \\ z \end{pmatrix} = \begin{pmatrix} x \\ g * x + h \\ \pm\sqrt{s * x^2 + t * x + u} \end{pmatrix} \tag{5.27}$$

Equation (5.27) represents the intersection curve of two hyperboloids created by reference modules 1 and 2 and modules 1 and 3 respectively. To achieve a quadratic solution with two possible positions of the mobile module, a third hyperboloid is needed. This could be achieved by a combination of reference modules 2 and 3. The intersection of three hyperboloids results in a set of two possible position solutions, where plausibility checks can help to discard one of the solutions. Like spherical localization algorithms, hyperboloidal techniques can be extended to more reference modules and therefore more information to obtain the position of a mobile node.

Part III

Radio Location Prototype

6 Technology Setup

Based on the input from part II, the underlying technologies to build a radio location system for medical environment are chosen and set up. As already discussed in chapter 3.3 Ultra wideband is the pursued radio technology since it best meets the defined requirements from chapter 2. Section 6.1 provides information on how the hardware and signal for the proposed UWB technology is implemented into the prototype and which ranging technology is used by this implementation. The utilized localization technology and insights on counter-measures for known errors are given in chapter 6.2.

6.1 Radio and Ranging Technology Setup

For all conducted experiments, the PulsON 410 (P410) UWB ranging module by Time Domain is used as industrially available UWB localization hardware. The P410 development kit comprises four uniform UWB modules that can be used as anchors and tags. Figure 6.1 shows a P410 UWB board with a broad band antenna attached.

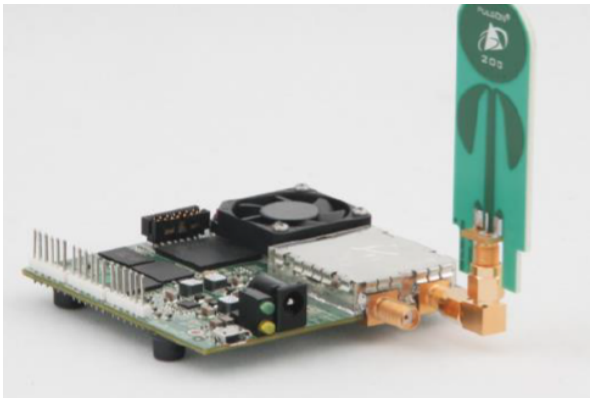

Figure 6.1: P410 UWB board with broad band antenna attached. (Tim17)

It can be seen that the board comprises two SMA antenna ports. It is useful for doing UWB radar measurements where one antenna sends off the signal and the other one receives the signal after reflections with the environment. In this work, only one antenna is used per UWB module since a point to point ranging scheme is pursued. The modules can be powered by a battery pack or power supply unit and provide some level of protection for the electronics by a plastic enclosure with polycarbonate cover. The UWB nodes transmit coherent RF signals compliant with the FCC emission limits. The signals span from 3.1 GHz to 5.3 GHz and a

maximum power level of −41.3 dBm/MHz which is . To emit the signal a planar elliptical dipole antenna with an omni-directional transmit and receive pattern is used. The antenna beam patterns are visualized in detail in figures C.1 and C.2. Figure 6.2 shows the antenna front and rear view with the respective phase centers that represent the points of localization.

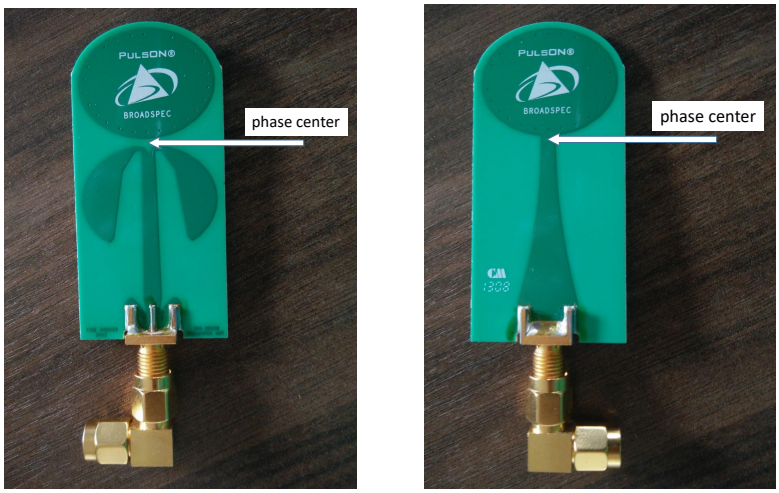

(a) Front side (b) Back side

Figure 6.2: Broadspec UWB antenna with phase center indicated on front and back side of the antenna. (Tim17)

The system works with a two-way time of flight ranging approach and is calibrated with an SMA right angle connector to represent the time of flight between phase centers of communicating UWB modules. For all conducted experiments four P410 UWB modules with the provided Broadspec antenna and the right angle SMA connectors are used. The transmitted UWB signal has a 1 n sec waveform show in figure 6.3.

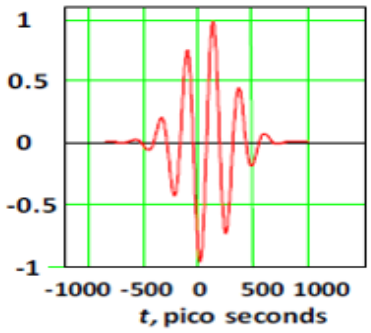

Figure 6.3: Waveform of the 1 n sec signal. (Tim17)

With this provided signal waveform and the used signal detection on the P410 UWB modules, Time Domain claims a ranging accuracy of 2.1 cm and a precision of 2.3 cm (Tim17).

6.2 Localization Technology Setup

With the four P410 UWB modules three ranges between one dedicated mobile node and three UWB anchor nodes can be measured. These ranges are the basis for the localization technique. For this under-constrained localization setup the spherical trilateration approach described in chapter 5.2.1 is suitable and therefore pursued. To get reasonable results from noisy measurement two countermeasures are implemented. Outliers in the UWB raw measurements are discarded using a velocity filter with threshold v_{max} between two update steps. If the calculated velocity exceeds the predefined value the measurement is discarded. To overcome noise effects in the provided raw distance measurements a second measure is pursued. Figure 6.4 shows an error case that results from too short raw distance information. The three spheres representing the range measurements do not intersect. Two spheres from a pair of UWB reference nodes intersect in a circle, but for any combination the third sphere does not intersect this circle at all.

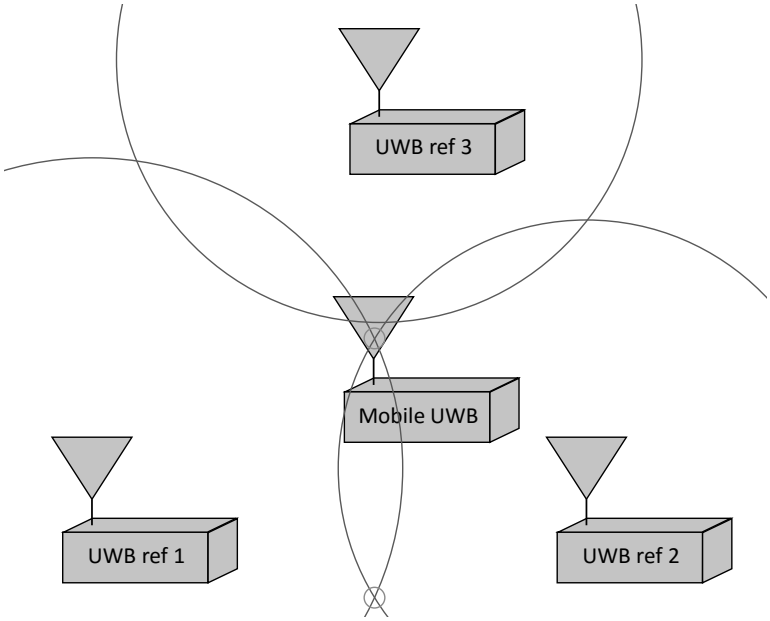

Figure 6.4: Schematic representation of the trilateration approach for an erroneous underdetermined scenarios in a 2 D view with three UWB reference modules at known positions. The raw distance measurements provide distance information that are shorter than the real distances between UWB modules. In this case, UWB reference modules 1 and 2 intersect in a circle, represented by two intersection points (highlighted by orange circles) in this 2 D view. The distance sphere from UWB reference 3 does not intersect with the circle from ref 1 and 2.

One way is to anticipate wrong measurements when no intersection occurs and to adapt the ranging results. (KEO09) proposes an approach to account for range measurement errors. Each raw range measurement can be adapted by a certain additional range to find a suitable intersection. With the adapted range data the trilateration algorithm can be again executed. For the experiments conducted a range adaption algorithm to account for range measurement errors is implemented.

7 Tracking Filter

Raw data results of measurement system are often prone to noise or misreading which result in outliers. Filter methods are commonly used to improve the results of localization systems. With the measurement system providing positioning or localization information filters often are used to keep track on the position over time and therefore are named tracking filters. This chapter introduces three tracking filter approaches with different complexity beginning with a Moving Average Filter in section 7.1. Section 7.2 sheds a light on the Particle Filter approach. The Kalman Filter is described in section 7.3.

7.1 Moving Average Filter

The Moving Average Filter is an approach to compute the mean value over a fixed and predefined number of the last N measurements. In the case of this UWB localization system it averages over distance measurements that contribute to the trilateration algorithm. To obtain the average location estimate at measurement step k equation (7.1) is used.

$$(\bar{x}_k, \bar{y}_k, \bar{z}_k) = \frac{1}{N} \sum_{n=0}^{N} \{(x_{k-n}, y_{k-n}, z_{k-n})\} \tag{7.1}$$

From an implementation perspective a moving average filter can be obtained by implementing a circular or ring buffer. This approach is visualized in figure 7.1 with a moving average filter of size $N = 10$.

Once the ring-buffer is filled, it always provides the mean value of the last N provided measurements. For larger N, the precision of the position estimate in a static scenario improves. Noise in the measurement data is leveled out whereas the inert aspect of the filter increases with larger N. In a dynamic scenario where the real position of the tracked object changes the mean position using N values is slow to follow.

7.2 Particle Filter

The Particle Filter is an efficient tool to model non-Gaussian distributions. It can be characterized as a sequential Monte-Carlo Bayesian filter (LC98). It uses a set of particles and

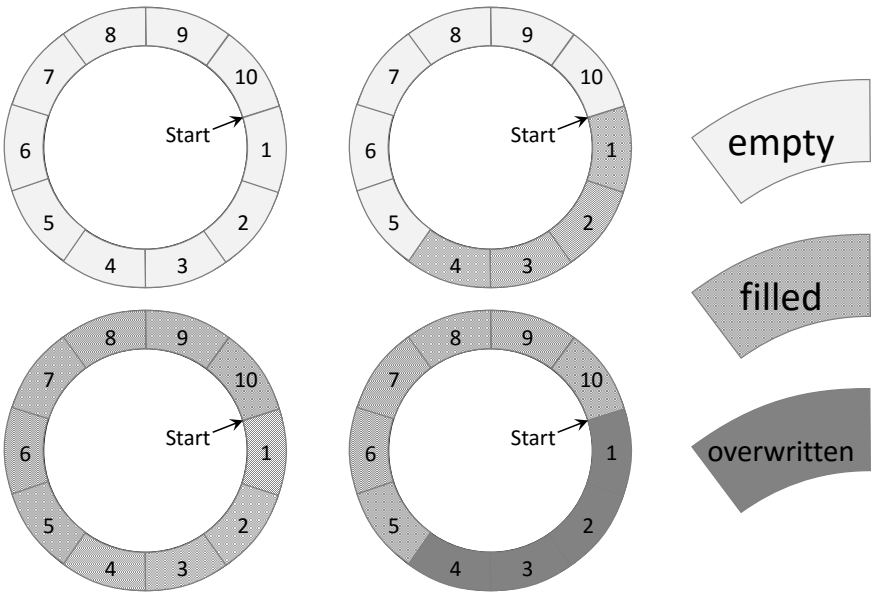

Figure 7.1: Ring buffer implementation to obtain a moving average filter. The presented ring buffer provides ten data cells. In the beginning all cells are empty. With incoming information, the cells are filled one after the other beginning with cell 1. Once all cells of the ring buffer are filled with information, cells are overwritten starting with the first one.

the state of the particle where each particle carries a set of information, but with individual values. In this UWB localization system $x_k = (x, y, z, \bar{x}, \bar{y}, \bar{z})$ represent the state of the particles, representing UWB nodes. The triplet (x, y, z) represents the estimated location whereas $(\bar{x}, \bar{y}, \bar{z})$ can be interpreted as movement direction (BKR15). A region of interest is defined and populated with $n = 1000$ initial particles that are distributed randomly (BKR15). Figure 7.2 shows 1000 randomly distributed particles in a given range.

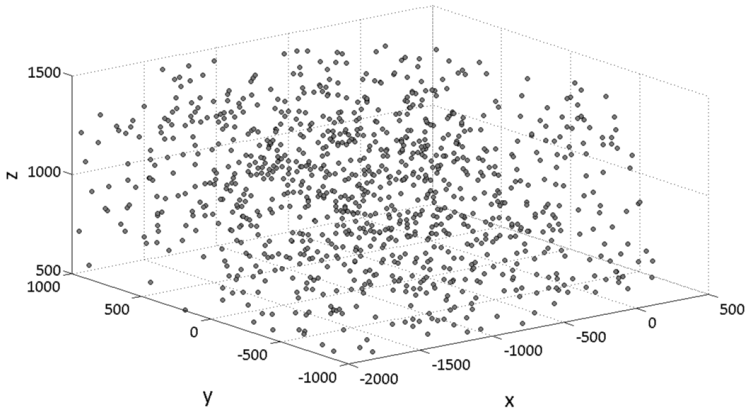

Figure 7.2: Initial Particle distribution with 1000 particles in a range of x from -2000 to 500 mm, y from -1000 to 1000 mm and z from 500 to 1500 mm.

For each particle a likelihood p is calculated which represents the probability of this particle to represent the mobile UWB node's real location. To compute the likelihood the multivariate normal distribution from equation (7.2) is used.

$$p = \frac{1}{\sqrt{(2\pi)^3|\Sigma|}} exp(-\frac{1}{2}(x-\mu)^T\Sigma^{-1}(x-\mu)) \tag{7.2}$$

In equation (7.2), „x is the position of the current particle, μ represents the trilaterated position of the UWB measurement and Σ is the covariance matrix of the distribution, with $|\Sigma|$ being its determinant. Based on the calculated likelihood for all n particles a resampling step is performed“(BKR15). In the resampling step each particle is chosen based on its likelihood to be a candidate for the real position. It is also possible for a particle to be chosen more than once, since the resampling phase represents a sampling with replacement. The closer the particle information is compared to the estimated information, the more likely it is for this particle to be resampled. This leads to a concentration of particles in the area of the real position of the mobile UWB node. Figure 7.3 visualizes 1000 particles with the initial distribution from figure 7.2 after 10 and 100 resampling steps. It can be seen that the particles are more and more crowded in one area.

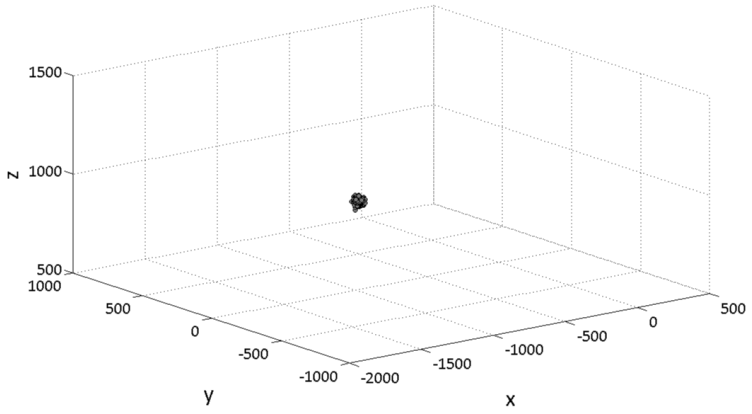

(a) after 10 resampling steps

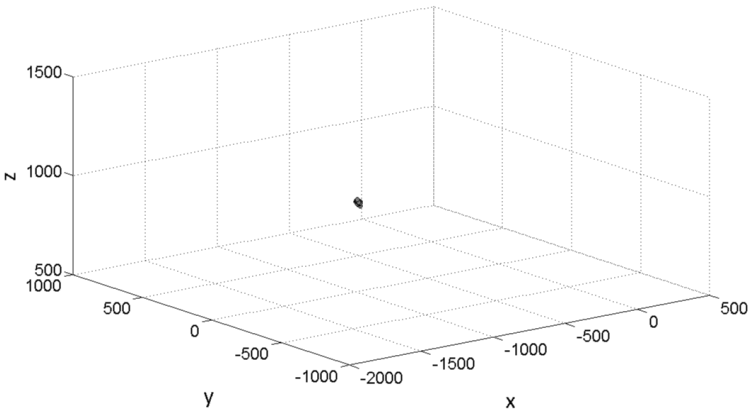

(b) after 100 resampling steps

Figure 7.3: Particle distribution of 1000 particles after 10 and 100 resampling steps in a range of x from -2000 to 500 mm, y from -1000 to 1000 mm and z from 500 to 1500 mm.

To account for movement of the mobile UWB node during the resampling step the heading direction of the newly created particles is set randomly whereas the velocity σ_v is normally distributed. If the mobile UWB module moves in between measurement steps, it is likely that one of the particles represents a movement close to the real performed one. Figure 7.4 shows the area of the concentrated particles in detail. It can be seen that the particles are spacially distributed in an area of 800 cm^3 and 50 cm^3 after 10 and 100 resampling steps and movement predictions respectively. It can be seen that after 100 resampling steps the particle set comprises more duplicated particles in a more selective area since the results become more robust.

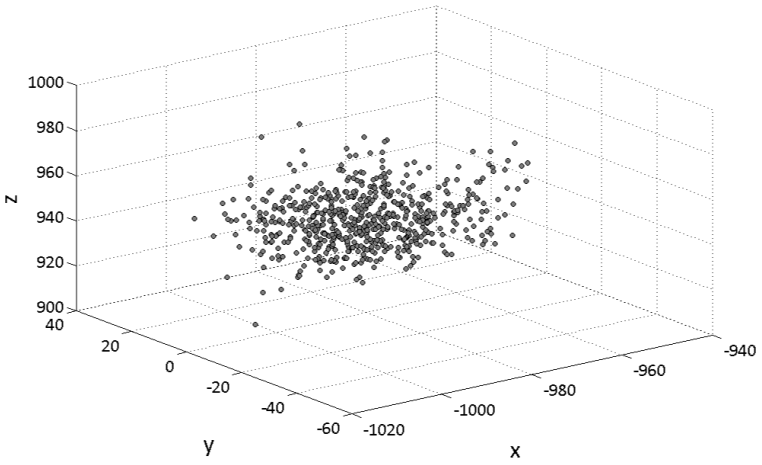

(a) after 10 resampling steps

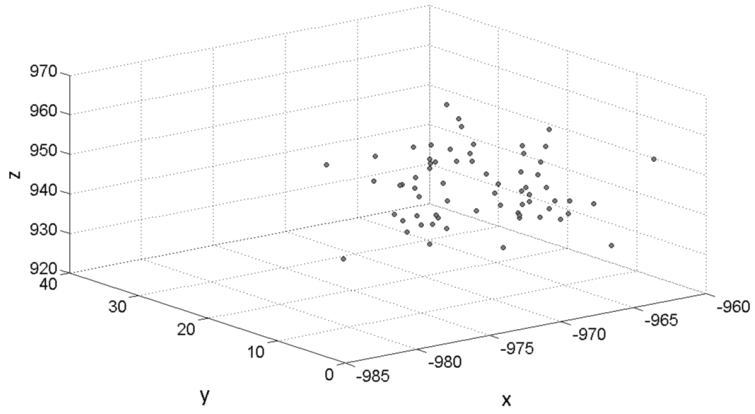

(b) after 100 resampling steps

Figure 7.4: Zoom into two particle distributions of 1000 particles after 10 and 100 resampling steps in a range of x from -1020 to −920 mm, y from -60 to 40 mm and t from 900 to 1000 mm for 10 resampling steps and x from -985 to −960 mm, y from 0 to 40 mm and z from 920 to 970 mm for 100 resampling steps respectively.

The limiting factor for using the particle filter in a dynamic scenario with a large volume of interest is speed of computation of the likelihood for a large number of particles. On the one hand, the more particles are used, the more precise and robust the result gets. On the other

hand this leads the particle filter to be slow. One measure to overcome this drawback is to dynamically adapt the width of the multivariate normal distribution when a new UWB node is found or the particle filter is initially started. Figure 7.5 shows three qualitative normal distributions with different standard deviations σ.

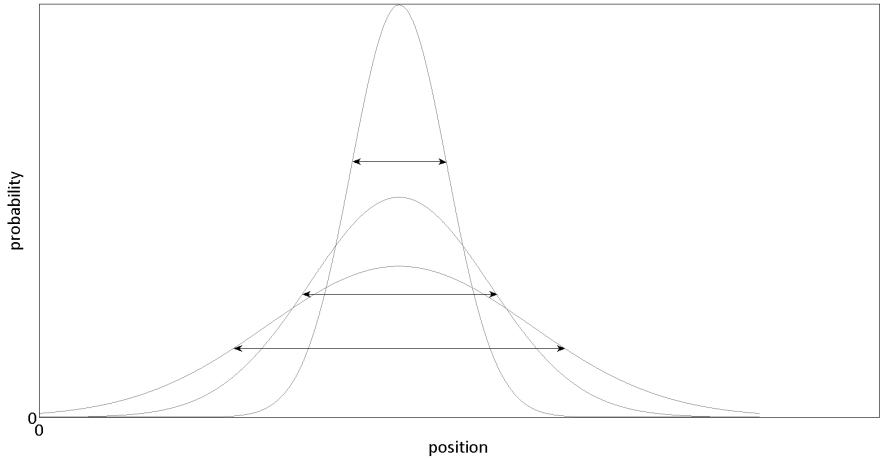

Figure 7.5: Adapted normal distribution with three different standard deviations σ. In the beginning when the uncertainty is high, the normal distribution with a high standard deviation is used. This leads to reasonable probability results even when sparsely distributed particles. After some resampling steps a lower standard deviation is chosen since most particles are in an area close to the real position. This leads to more precise results since the likelihood is computed more selective.

With this measure being implemented the number of particles can be reduced to an amount that provides decent speed of the filter. In the beginning of a measurement a large width is used for the multivariate normal distribution, such that we still find the particles closest to the real position despite of the sparse particle distribution. After a number of resampling steps the filter width is reduced. This leads to more selective resampling results. For this approach a descending function from equation (7.3) can be chosen.

$$filterWidth_i = maxWidth/i, \quad for\ i = 1 \dots n \tag{7.3}$$

For the first n measurements the ith filter width is computed from a maximum value divided by the current count i of the measurements. After n measurements the filter width remains on a constant value.

7.3 Kalman Filter

The Kalman Filter is an optimal recursive filter to find efficient and unbiased estimates for a dynamic system from noisy measurements. In section 7.3.1 the basic formulation of the Kalman Filter is described. An overview of how parts of the Kalman Filter are modeled is given in Section 7.3.2. Section 7.3.3 introduces an adaptive covariance variation of the Kalman Filter.

7.3.1 Basics

The Kalman Filter was derived in 1960 by Rudolf Emil Kalman (Kal60). To find the optimal least squares solution with a Kalman Filter, normally distributed and zero mean white noise is presupposed for the measurements and the modeled system. It is also assumed that the state evolution of the dynamic system is linear. By sequentially using the noisy measurement data, the state of the linear dynamic system and the associated covariance matrix are estimated. The standard state-space formulation of a Kalman Filter is represented in a continuous way in (7.4)

$$\dot{x}(t) = F(t)x(t) + B(t)u(t) + w(t), \text{ where} \tag{7.4}$$

$x(t)$ is the state vector of interest,

$u(t)$ is a known control input,

$w(t)$ is a zero mean normal distributed process noise vector describing uncertainty in the evolution of the state,

$F(t)$ is the $n \times n$ state model matrix,

$B(t)$ is the $n \times s$ input matrix,

s is the number of input signals.

It can be seen that the predicted state is estimated by combining the current state, known input data and modeled system noise. To describe the influence of measurements on the state-space, an observation model is incorporated with (7.5)

$$z(t) = H(t)x(t) + v(t), \text{ where} \tag{7.5}$$

$z(t)$ is the observation vector,

$x(t)$ is the state vector,

$v(t)$ is a zero mean normal distributed measurement noise vector describing uncertainty in the observation,

$H(t)$ is the $m \times n$ observation model matrix,

m is the number of states observed,

The state vector is updated by combining observations applied through the observation model and the corresponding measurement noise. With a discrete-time set $t = t_0, t_1, \cdots, t_k, \cdots$ and the assumption that during each time step the system behaves in a linear way, a discrete-time formulation can be found in (7.6). For notation purpose it is assumed that every time-step is of same length so the time argument can be exchanged by an index variable referring to the sample number. When implementing the Kalman Filter, the length for each time-step can be estimated and used for calculation.

$$x_k = F_{k-1}x_{k-1} + B_{k-1}u_{k-1} + w_{k-1}. \tag{7.6}$$

The process noise w can be rewritten as $w \sim N(0, Q)$ to mathematically represent an independent white noise with normal probability distribution. The corresponding covariance matrix of the state is predicted by equation (7.7)

$$P_k = F_k P_{k-1} F_k^T + Q_k, \ where \tag{7.7}$$

Q_k is the process noise covariance matrix,

P_k is the coavariance matrix at time-step k.

Equivalently the observation model can be described for a discrete-time set as (7.8). The observation model is often reformulated to represent the difference between measurement and estimated state shown in (7.9).

$$z_k = H_k x_k + v_k. \tag{7.8}$$

$$y_k = z_k - H_k x_k. \tag{7.9}$$

The measurement noise v can be rewritten as $v \sim N(0, R)$ to mathematically represent an independent normally distributed white noise. The corresponding covariance adaption is given in (7.12) respectively. To compute the covariance matrix update, the Kalman covariance innovation S in (7.10) and the Kalman gain K in (7.11) are required.

$$S_k = H_k P_{k-1} H_k^T + R \tag{7.10}$$

$$K_k = P_{k-1} H_k^T S^{-1} \tag{7.11}$$

$$P_k = (I - K_k H_k) P_{k-1} \tag{7.12}$$

Figure 7.3.1 shows how the predict and update functions of the Kalman Filter are conducted in a loop to track the state of an object. It is also possible to not sequentially alternate between predict and update phase every time. Whenever an observation is available, the update phase can be conducted. Between two measurements the predict phase can be used in fixed time-steps to continually estimate the current state of the system.

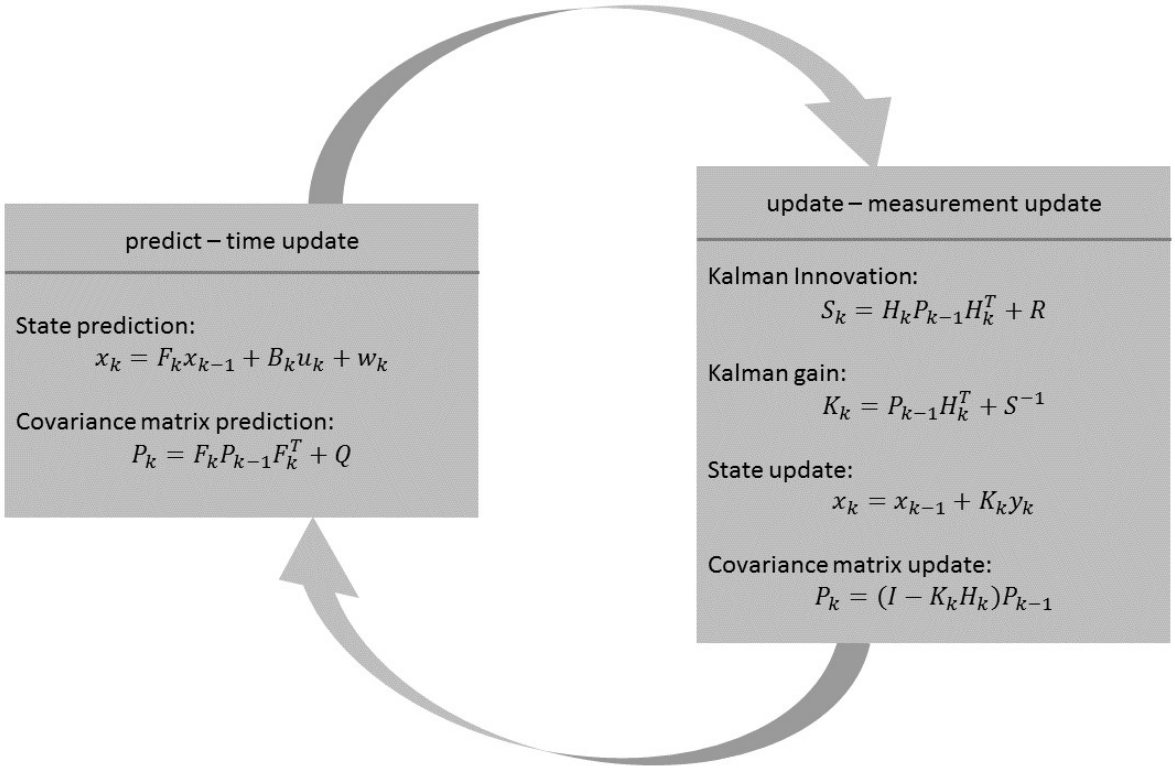

Figure 7.6: Kalman Filter loop with predict and update phase alternating.

For modeling a tracking filter based on UWB localization signals no control inputs are modeled since we have no knowledge of the influence on the state space behavior. There are two options for the system noise model. Examples how to implement a gaussian distributed system noise model for different state models and influence parameters are given in section 7.3.2. Another approach is to discard the system noise level since we have no information on the system noise which would lead to best guess the values applied. In this potion one has to find another way of accounting for noise behavior which is provided in section 7.3.3. The resulting representation for the state estimations without system noise implemented is given in (7.13).

$$x_k = F_k x_{k-1}. \tag{7.13}$$

The update phase used for a tracking filter based on UWB localization signals can be formulated as (7.14) where the updated system state is computed using the current system state, the Kalman gain from (7.11) and the reformulated observation model (7.9).

$$x_k = x_{k-1} + K_k y_k \tag{7.14}$$

7.3.2 Model

The state space of a UWB module can be modeled with different specifications. An essential component is the position of the UWB module give by three coordinates x, y, z. A second and third part of the state model can represent the motion of the UWB module. We consider three different motion models for the behavior of the UWB modules and therefore three different state space models:

static model	$\mathbf{x_k} = (x, y, z)$
constant velocity model	$\mathbf{x_k} = (x, y, z, \dot{x}, \dot{y}, \dot{z})$
constant acceleration model	$\mathbf{x_k} = (x_k, y_k, z_k, \dot{x}_k, \dot{y}_k, \dot{z}_k, \ddot{x}_k, \ddot{y}_k, \ddot{z}_k)$

In the static model, the position is assumed to be constant and no motion is used. The constant velocity and constant acceleration model describe motions with constant velocity and constant acceleration respectively. For each of the state models the state model matrices and observation model matrices have to be created. Furthermore, the corresponding zero mean normal distributed process noise has to be modeled. The 3×3 version of the static state model matrix is given in (7.15). The 6×6 version for the constant velocity and the 9×9 acceleration state model are given in (7.16) and (7.17) respectively.

$$F_{static} = \begin{pmatrix} 1 & 0 & 0 \\ 0 & 1 & 0 \\ 0 & 0 & 1 \end{pmatrix} \tag{7.15}$$

$$F_{constvel} = \begin{pmatrix} 1 & 0 & 0 & dt & 0 & 0 \\ 0 & 1 & 0 & 0 & dt & 0 \\ 0 & 0 & 1 & 0 & 0 & dt \\ 0 & 0 & 0 & 1 & 0 & 0 \\ 0 & 0 & 0 & 0 & 1 & 0 \\ 0 & 0 & 0 & 0 & 0 & 1 \end{pmatrix} \tag{7.16}$$

$$F_{constacc} = \begin{pmatrix} 1 & 0 & 0 & dt & 0 & 0 & \frac{dt^2}{2} & 0 & 0 \\ 0 & 1 & 0 & 0 & dt & 0 & 0 & \frac{dt^2}{2} & 0 \\ 0 & 0 & 1 & 0 & 0 & dt & 0 & 0 & \frac{dt^2}{2} \\ 0 & 0 & 0 & 1 & 0 & 0 & dt & 0 & 0 \\ 0 & 0 & 0 & 0 & 1 & 0 & 0 & dt & 0 \\ 0 & 0 & 0 & 0 & 0 & 1 & 0 & 0 & dt \\ 0 & 0 & 0 & 0 & 0 & 0 & 1 & 0 & 0 \\ 0 & 0 & 0 & 0 & 0 & 0 & 0 & 1 & 0 \\ 0 & 0 & 0 & 0 & 0 & 0 & 0 & 0 & 1 \end{pmatrix} \tag{7.17}$$

The observation model of a UWB localization system is described by the 3×3 matrix in (7.18) for the static state model, by a 3×6 matrix in (7.19) and a 3×9 matrix in (7.20) for the

constant velocity and acceleration model respectively. The equations show position data as the output of the UWB measurement system which therefore yields only direct influence to the position part of the system state but not the velocity and acceleration information.

$$H(k) = \begin{pmatrix} 1 & 0 & 0 \\ 0 & 1 & 0 \\ 0 & 0 & 1 \end{pmatrix} \tag{7.18}$$

$$H(k) = \begin{pmatrix} 1 & 0 & 0 & 0 & 0 & 0 \\ 0 & 1 & 0 & 0 & 0 & 0 \\ 0 & 0 & 1 & 0 & 0 & 0 \end{pmatrix} \tag{7.19}$$

$$H(k) = \begin{pmatrix} 1 & 0 & 0 & 0 & 0 & 0 & 0 & 0 & 0 \\ 0 & 1 & 0 & 0 & 0 & 0 & 0 & 0 & 0 \\ 0 & 0 & 1 & 0 & 0 & 0 & 0 & 0 & 0 \end{pmatrix} \tag{7.20}$$

To model the uncertainty in the evolution of the state we can assume different influences between $k-1$ and k. In equation (7.21) and (7.22) for a static state model we compose a position error and a velocity error respectively. Matrix G applies the unknown influence to the used state space model.

$$w_{static,pos} = Q = GG^T\sigma^2 = \begin{pmatrix} 1 \\ 1 \\ 1 \end{pmatrix} \begin{pmatrix} 1 & 1 & 1 \end{pmatrix} \begin{pmatrix} \sigma^2_{x_{sys}} \\ \sigma^2_{y_{sys}} \\ \sigma^2_{z_{sys}} \end{pmatrix} \tag{7.21}$$

$$w_{static,vel} = Q = GG^T\sigma^2 = \begin{pmatrix} dt \\ dt \\ dt \end{pmatrix} \begin{pmatrix} dt & dt & dt \end{pmatrix} \begin{pmatrix} \sigma^2_{x_{sys}} \\ \sigma^2_{y_{sys}} \\ \sigma^2_{z_{sys}} \end{pmatrix} \tag{7.22}$$

In equation (7.23) and (7.24) velocity and acceleration noise for a constant velocity state space model are given. Equation (7.25) gives an example for a combined velocity and acceleration uncertainty in the state evolution for a constant acceleration state space model.

$$w_{const\_vel,vel} = Q = GG^T\sigma^2 = \begin{pmatrix} dt \\ dt \\ dt \\ 1 \\ 1 \\ 1 \end{pmatrix} \begin{pmatrix} dt & dt & dt & 1 & 1 & 1 \end{pmatrix} \begin{pmatrix} \sigma^2_{x_{sys}} \\ \sigma^2_{y_{sys}} \\ \sigma^2_{z_{sys}} \\ \sigma^2_{x_{sys}} \\ \sigma^2_{y_{sys}} \\ \sigma^2_{z_{sys}} \end{pmatrix} \tag{7.23}$$

$$w_{const\_vel,acc} = Q = GG^T\sigma^2 = \begin{pmatrix} \frac{dt^2}{2} \\ \frac{dt^2}{2} \\ \frac{dt^2}{2} \\ dt \\ dt \\ dt \end{pmatrix} \begin{pmatrix} \frac{dt^2}{2} & \frac{dt^2}{2} & \frac{dt^2}{2} & dt & dt & dt \end{pmatrix} \begin{pmatrix} \sigma^2_{x_{sys}} \\ \sigma^2_{y_{sys}} \\ \sigma^2_{z_{sys}} \\ \sigma^2_{x_{sys}} \\ \sigma^2_{y_{sys}} \\ \sigma^2_{z_{sys}} \end{pmatrix} \tag{7.24}$$

$$w_{const\_acc,acc} = Q = GG^T\sigma^2 = \begin{pmatrix} \frac{dt^2}{2} \\ \frac{dt^2}{2} \\ \frac{dt^2}{2} \\ dt \\ dt \\ dt \\ 1 \\ 1 \\ 1 \end{pmatrix} \begin{pmatrix} \frac{dt^2}{2} & \frac{dt^2}{2} & \frac{dt^2}{2} & dt & dt & dt & 1 & 1 & 1 \end{pmatrix} \begin{pmatrix} \sigma^2_{x_{sys}} \\ \sigma^2_{y_{sys}} \\ \sigma^2_{z_{sys}} \\ \sigma^2_{x_{sys}} \\ \sigma^2_{y_{sys}} \\ \sigma^2_{z_{sys}} \\ \sigma^2_{x_{sys}} \\ \sigma^2_{y_{sys}} \\ \sigma^2_{z_{sys}} \end{pmatrix} \tag{7.25}$$

To represent the uncertainty for the initial state estimation when the Kalman Filter is performed for the first time, the diagonal values of the covariance matrix of the state are set to a very high value since the chosen initial position is artificial and arbitrary. An example is given in (7.26).

$$P_0 = \begin{pmatrix} 1000 & 0 & 0 & 0 & 0 & 0 \\ 0 & 1000 & 0 & 0 & 0 & 0 \\ 0 & 0 & 1000 & 0 & 0 & 0 \\ 0 & 0 & 0 & 1000 & 0 & 0 \\ 0 & 0 & 0 & 0 & 1000 & 0 \\ 0 & 0 & 0 & 0 & 0 & 1000 \end{pmatrix} \tag{7.26}$$

The measurement noise covariance matrix should represent the uncertainty in the measurement system. For the UWB localization system an uncorrelated error for the directions x, y, z is assumed.

$$R_k = \begin{pmatrix} \sigma^2_{x_m} & 0 & 0 \\ 0 & \sigma^2_{y_m} & 0 \\ 0 & 0 & \sigma^2_{z_m} \end{pmatrix} \tag{7.27}$$

The information gained by updating and predicting the system using a Kalman Filter are the state space x_k and the covariance matrix P_k. In every single step of the Kalman Filter they get innovated based on either predicting the kth state or using an observation to update the predicted state.

7.3.3 Bounded Covariance Kalman Filter

During the update phase of the Kalman Filter, an acquired observation from sensor data provides information on the current system state to calculate a system state update. Every time the filter gets a set of measurements, it becomes more certain about the state of the filter that represents the physical parameters of the mobile UWB node. This results in decreasing values of the of the covariance matrix' diagonal terms of the system state. In a static situation every measurement gives the same result except for the randomly distributed measurement noise leading to ever decreasing diagonal terms of the covariance matrix approaching zero. In a situation of sudden movement the current state would be weighted so high because of the low values in the covariance matrix that a new measurement with different position data would be assumed as false reading measurement or outlier. This effect can be judged as inert behavior for the Kalman Filter state where it is slow to follow movement in reality after a static phase.

To overcome this behavior the prediction phase can be utilized and some countermeasures can be implemented. First, an appropriate state model should be chosen that represents the process movement best. For the three introduced state models similar observations of an inert behavior can be made. With a static model the state is anyways expected to stay in a constant position. With the constant velocity and constant acceleration model the computed velocity and acceleration in a static case approach zero and therefore the system only slowly follows a movement in the beginning. Second, the covariance matrix Q of the process noise can be set to a distinct value trying to limit the state covariance matrix to approach zero, since it adds up to the current covariance matrix values and increases them in every prediction step. For processes where static states are more likely, low values for Q can be applied and when the localized object is more likely to have a dynamic behavior the values for Q can be set higher. This can be called an offline adaptation of the Kalman Filter to different kinds of dynamic behaviors in the system to model. Third, die covariance matrix of the Kalman state can be influenced directly instead of using Q. Implementing a lower bound for the diagonal terms of the Kalman covariance matrix limits them approaching zero. In equation (7.28) the covariance matrix with a lower bound ξ is given.

$$P_k = \begin{pmatrix} \geq \xi & & \dots \\ & \geq \xi & \\ \dots & & \geq \xi \end{pmatrix} \tag{7.28}$$

This approach avoids the indirection of the Kalman covariance matrix values by using the unknown environment covariance matrix Q of the system noise and directly influences the points of interest. It also adapts faster to a static phase after motion. When a static phase of the tracked object occurres directly after a dynamic movement phase the Kalman Filter returns faster to the minimum available diagonal terms and therefore maximum inert behavior. With a defined environment covariance matrix Q this adaptation takes longer.

8 Experiments

To handle various experiments including simulations and real measurements with divers configurations of the measurement system a suitable software framework is needed. The implemented C++ code of the UWB localization prototype is adapted for every situation using an xml configuration file. This file defines a bunch of important information to run the localization system in different modes and with different characteristics. First of all, it provides position information on the UWB infrastructure or anchor modules. Figure 8.1 shows the structure of anchor position configuration with x-, y- and z-values in mm and the corresponding unique anchor ID to identify the UWB module. The configuration is extendable to any number of anchor nodes.

```
5    <!--Set infrastructure Nodes for UWB setup-->
6    <!--<Node ID="..." x="..." y="..." z="..."/>-->
7
8    <!--UWB Testbay-->
9    <INode ID="100" x="1988.2" y="-809.6" z="2751.7"/>
10   <INode ID="101" x="-3541.5" y="-586.9" z="2982.2"/>
11   <INode ID="102" x="-1475.2" y="1923.8" z="2966.7"/>
```

Figure 8.1: Configuration of UWB anchor nodes

A second configurable parameter of the UWB localization prototype is the used tracking filter. Figure 8.2 provides an overview of the three implemented tracking filter types „Buffer“, „Kalman“ and „Particle“ that can be chosen and parametrized using the parameters provided in the configuration file.

```
17     <!--"Buffer" for RingBuffer-->
18     <!--"Kalman" for KalmanFilter-->
19     <!--"Particle" for ParticleFilter-->
20   <Filter type="Kalman">
21       <Buffer BufferSize="20" />
22       <Kalman BufferSize="1" KalmanMeasurementError="50.0"
23       KalmanSystemError="0.0" KalmanMinPvalue="0.5" MaxNodeSpeed="1000" />
24       <Particle BufferSize="1" NumberOfParticles="1000"
25       MaxParticleSpeed="0.3" FilterWidth="50" filename="particles.txt"/>
26   </Filter>
```

Figure 8.2: Configuration of UWB tracking filters

For the Moving Average Filter the „BufferSize“ N can be configured to create a dynamic or smooth filter behavior. The „BufferSize“ can also be set for the Kalman and Particle Filter approaches to realize combined filter types. To realize Kalman and Particle filters without ring-buffer influence the „BufferSize“ can be set to 1. Using a Moving Average Filter with $N = 1$ results in raw UWB positioning data without any filter effect.

For the Kalman filter four additional parameters can be set to characterize the filter behavior. The „KalmanMeasurementError“ indicates the expected error from measurements from the UWB positioning system in mm whereas the „KalmanSystemError“ represents the error of the environment in mm. The „KalmanMinPvalue“ represents the threshold ξ for tuning the Kalman covariance matrix' diagonal terms. The lower the threshold the more inert the filter behavior. The „MaxNodeSpeed“ indicates the parameter v_{max} in m/s introduced in section 6.2 to check for reasonable results from a trilateration calculation. If the estimated velocity of the mobile UWB module exceeds the „MaxNodeSpeed“ between two consecutive measurements it is counted as a measurement error and therefore discarded. The constant velocity model is used as fixed state model for the following experiments.

For the Particle filter another set of four specific parameters can be configured. The „NumberOfParticles“ indicates the number of particles used for the filter algorithms. The „MaxParticleSpeed“ provides the standard deviation of the absolute maximum speed of a particle between measurement steps in m/s. With the direction of each particle this speed defines the dynamic behavior of the particle set. The „FilterWidth“ indicates the shape of the used multivariate Gaussian distribution after the ramp phase at filter initialization or when a new UWB module is recognized. The „filename“ indicates where the randomly distributed initial particle set is recorded.

The type of conducted experiments is also configurable in the xml file. Figure 8.3 provides information on the three different experiment types „Real“, „SimArt“ and „SimReal“.

```
26      <!--"Real" for RealMeasurement-->
27      <!--"SimArt" for Simulation with artificial data-->
28      <!--"SimReal" for Simulation with external data input-->
29    <Measurement type="SimReal">
30        <Real>
31          <ComPort>COM6</ComPort>
32          <MeasurementNumberOfIterations>10000</MeasurementNumberOfIterations>
33        </Real>
34        <SimReal>
35          <!--"plain" for raw data-->
36          <!--"managed" for UWB and Optotrak data from MessageBus-->
37          <inputdata_type>plain</inputdata_type>
38          <inputdata>Test_Data_Simulation\particle_UWB.txt</inputdata>
39          <outputfolder>Test_Data_Simulation</outputfolder>
40        </SimReal>
41        <SimArt>
42          <SimulationDistanceNoise>10</SimulationDistanceNoise>
43          <SimulationPositionNoise>0</SimulationPositionNoise>
44          <SimulationNumberOfIterations>1000</SimulationNumberOfIterations>
45          <Node ID="200" x="-961.2" y="-1.5" z="948.8"/>
46        </SimArt>
47    </Measurement>
```

Figure 8.3: Configuration of UWB experiment type

In „Real“ measurement experiments with attached UWB hardware are conducted. The „ComPort“ indicates the ComPort the UWB system uses for communication with the lab PC.

„MeasurementNumberOfIterations“ is the number of trilateration data sets aggregated per run. This parameter makes it easy to realize experiments of same length. With every conducted real measurement campaign the raw measurements and the filter results are recorded.

„SimArt“ defines an artificial simulation with configurable noise behavior for distance measurements and position accuracy set in parameters „SimulationDistanceNoise“ and „SimulationPositionNoise“ respectively. The number of conducted simulated measurements is configured in „SimulationNumberOfIterations“. The artificial mobile UWB module is defined based on the definition of the UWB anchor nodes by ID and x-, y- and z-coordinates in mm.

In „SimReal“ formerly recorded measurement data from real measurements can be played back. This allows to apply different tracking filters with different parametrizations to the same real measurement. There are two „inputdata_type“ configurations for only UWB data and combined UWB and optical reference data. The folder for „inputdata“ and the „outputfolder“ can also be defined.

In the upcoming sections, the developed UWB localization prototype is scrutinized heavily. In section 8.1 the Moving Average, Particle and Kalman Filter are compared using the UWB simulation in a static measurement scenario. In section 8.2 the system setup for experiments in a medical environment is described. First measurements are conducted in section 8.3 to get a feeling on the effect of different filter configurations. A comparison of the presented radio location prototype implemented with the Moving Average, Particle and Kalman Filter based on real measurements in a medical environment is provided in section 8.4.

8.1 Simulation

To get a first impression on the tracking filter behavior for the implemented Moving Average Filter, Particle Filter and Kalman Filter, a simulation of a static measurement scenario with zero mean Gaussian distributed noise is conducted. Figure 8.4 shows unfiltered simulated raw data and results from an applied Moving Average Filter. Particle and Kalman Filter results are visualized in figure 8.5.

A qualitative analysis from the graphs shows that raw data results in the highest position estimation noise, whereas the Kalman filter settles to a state with low deviation after a starting phase. Particle and Moving Average filter reduce the noise but maintain quite high amplitudes. To get a more precise understanding of the simulation of the tracking filters the standard deviation σ in equation (8.1) and the root mean square error RMSE in equation (8.2) are calculated.

$$\sigma = \sqrt{\frac{\sum_{n=0}^{N} \left((\bar{x} - x_n)^2 + (\bar{y} - y_n)^2 + (\bar{z} - z_n)^2 \right)}{N}} \tag{8.1}$$

$$RMSE = \sqrt{\frac{\sum_{n=0}^{N} \left((\hat{x} - x_n)^2 + (\hat{y} - y_n)^2 + (\hat{z} - z_n)^2 \right)}{N}} \tag{8.2}$$

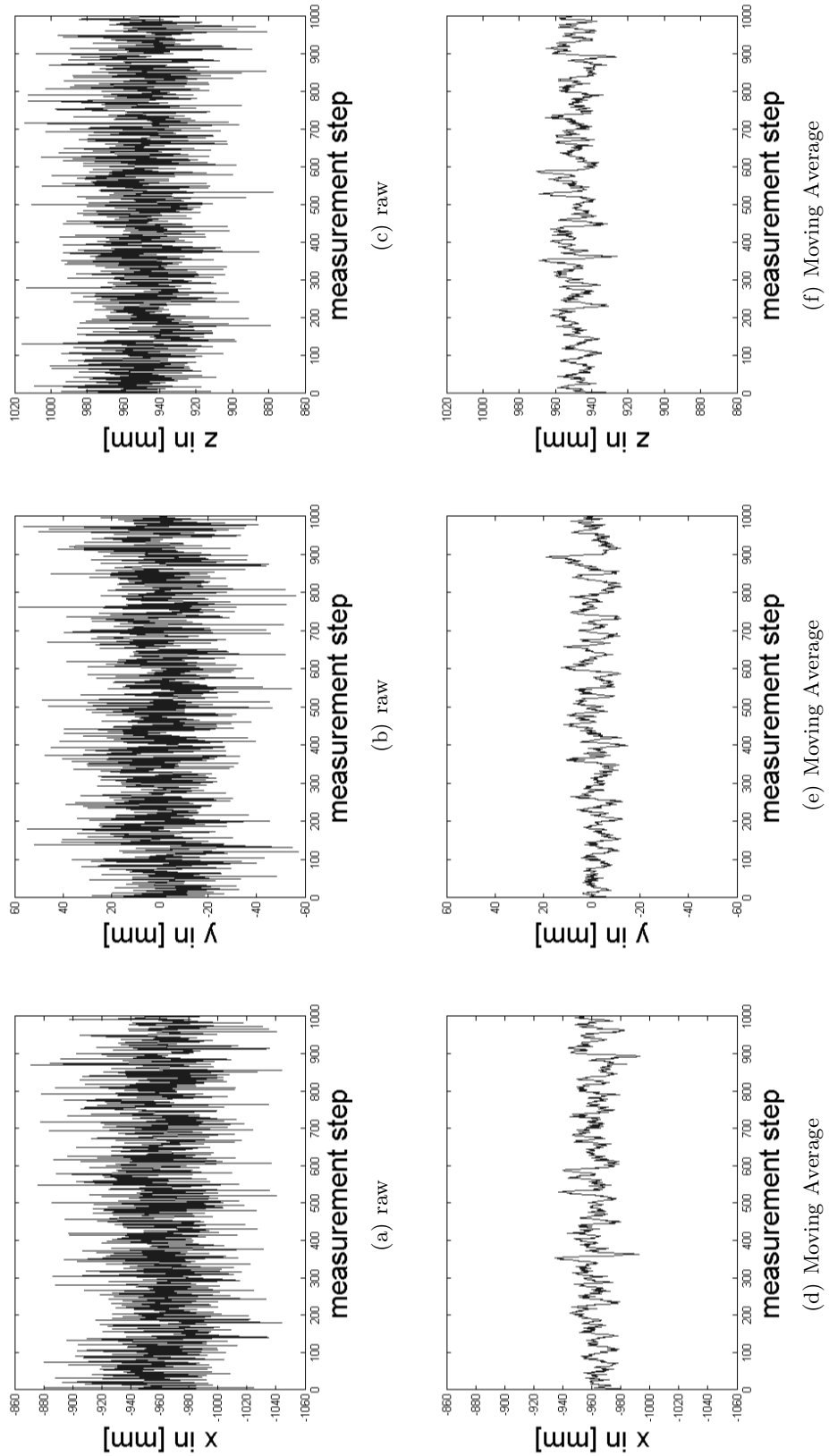

(a) raw (b) raw (c) raw

(d) Moving Average (e) Moving Average (f) Moving Average

Figure 8.4: UWB position data using simulated raw measurements with zero mean Gaussian distributed noise and an applied Moving Average Filter with size $N = 10$.

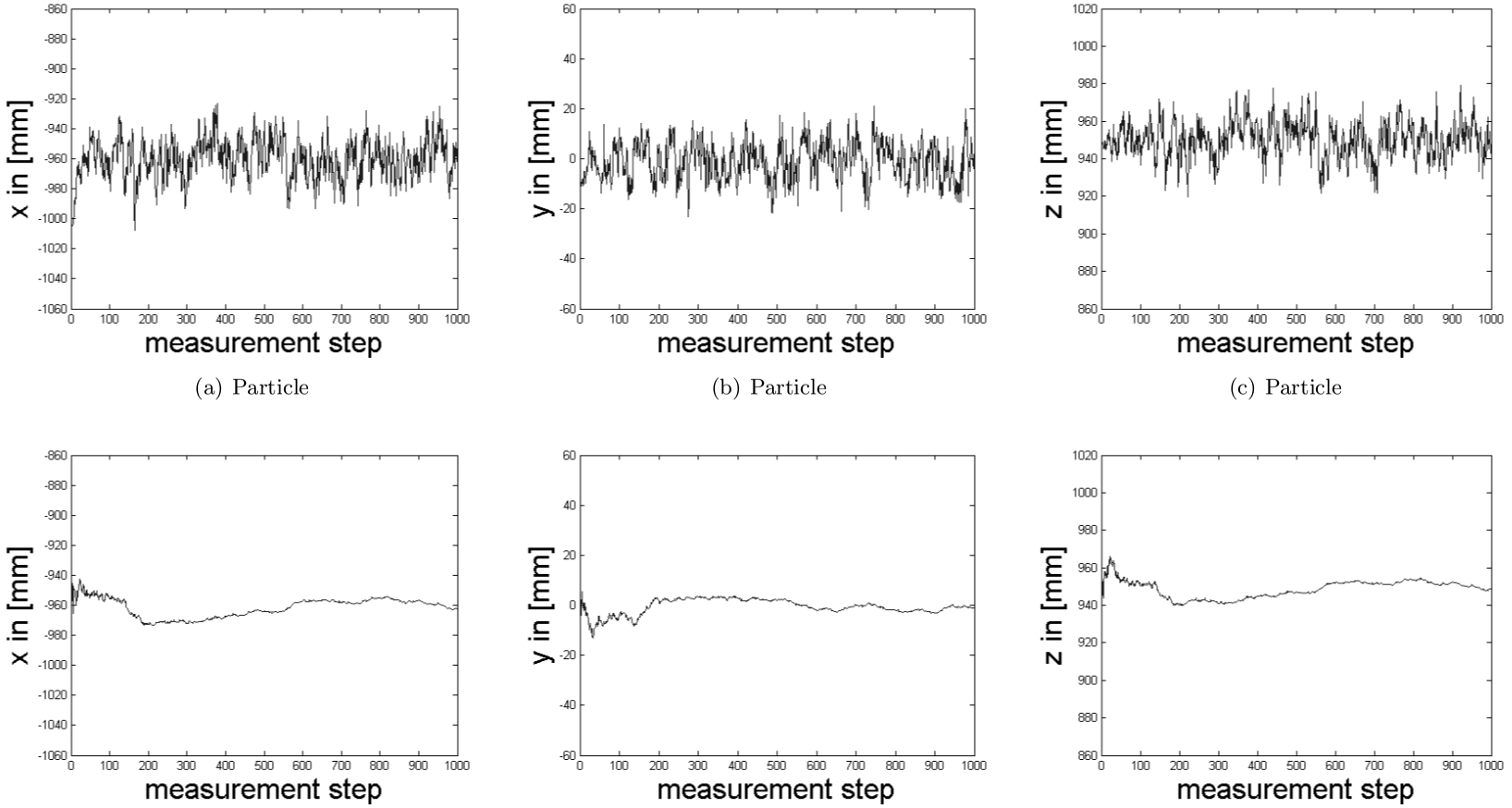

(a) Particle (b) Particle (c) Particle

(d) Kalman (e) Kalman (f) Kalman

Figure 8.5: UWB position data using simulated raw measurements with zero mean Gaussian distributed noise from figure 8.4 and applied Particle and Kalman Filter.

For the standard deviation the square error for each element of N measurements versus the mean value of all N measurements is calculated. On the contrary the RMSE uses the square error between each measurement element and the reference position. Table 8.1 and 8.2 provide the calculated RMSE and standard deviations for simulated raw measurements and applied filters.

Table 8.1: Accuracy of simulations with static scenario

	x [mm]	y [mm]	z [mm]	3D [mm]
Raw	30.6	18.8	23.5	43.0
Moving Average	8.7	5.3	7.2	12.4
Particle	13.5	7.6	9.9	18.4
Kalman	6.4	3.2	4.7	8.5

Table 8.2: Precision of simulations with static scenario

	x [mm]	y [mm]	z [mm]
Raw	30.6	18.8	23.5
Moving Average	8.6	5.3	7.1
Particle	13.5	7.6	9.8
Kalman	6.3	3.0	4.7

From the results it can be seen that the standard deviation and RMSE give the same values for all datasets. This effect means that the mean value of raw and filtered simulations lies close to the given reference position. Table 8.3 visualizes this result. It is not a surprise since the mean and reference values in this simulation experiment coincide. This is caused by the applied zero mean Gaussian distributed noise.

Table 8.3: Absolute position results of simulations with static scenario

	x [mm]	y [mm]	z [mm]
Reference	-961.2	-1.5	948.8
Raw	-961.2	-0.7	949.0
Moving Average	-961.6	-1.4	949.0
Particle	-960.3	-0.9	950.1
Kalman	-961.5	-0.6	948.7

Overall, all tracking filters improve the simulated raw measurements. The Kalman filter performs best under applied Gaussian noise in a static scenario. Further investigations are performed in real measurement experiments.

8.2 System Setup

The localization prototype is based on four industrially available PulsON 410 UWB modules by Time Domain (Tim17). Three UWB nodes are set up as ceiling-mounted anchors at fixed and known positions. The fourth UWB node represents the mobile object of interest that is localized using the reference nodes. Figure 8.6 shows a simulated setup of a medical environment. The green spheres represent the ceiling-mounted UWB anchor nodes. Multiple mobile nodes are shown with blue spheres at the display mount, on the patient table and on the trolley. The displayed values between the anchor nodes and one mobile node on the patient table represent range measurements in millimeter.

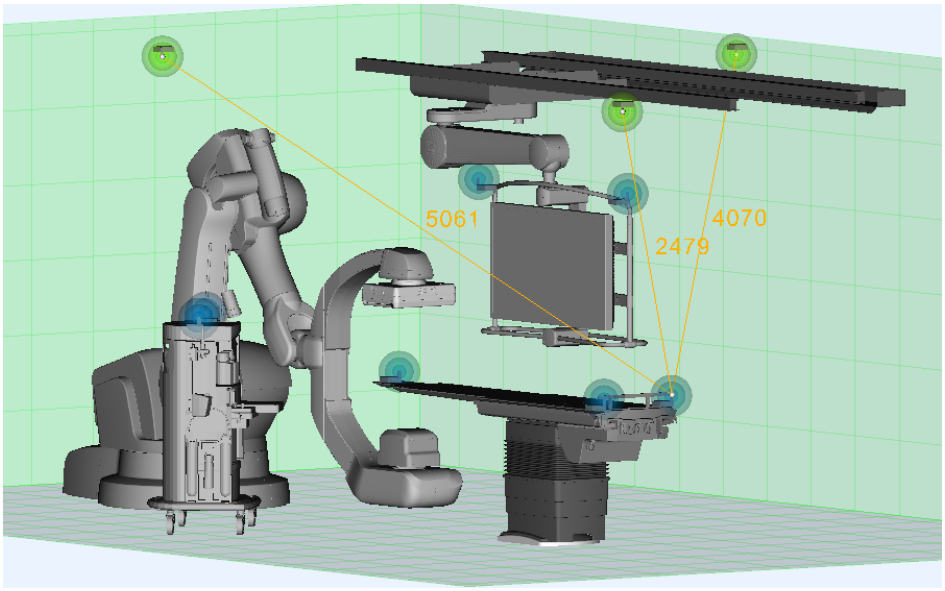

Figure 8.6: Simulated environment comprising a Siemens cone-beam system, medical table and medical display mounted on ceiling rails, an anesthesia cart. For localization purpose the reference is set up with three (green) UWB nodes at known locations and mobile (blue) UWB nodes are positioned on mobile objects. (BKR15) ©2015 IEEE

For the experiments the UWB prototype is located in an angiography test cabin comprising an Artis zeego robot-based cone-beam CT system, a large medical display that can be freely moved on ceiling mounted rails, several cupboards and the systems generator cabinet. Since the room is used for X-ray tests and experiments it is build of shielded walls and leaded glass. This results in reflections for radio signals on all surfaces and therefore severe multipath effects. The mobile UWB node is positioned on the tabletop of the patient table. Figures 8.7 and 8.8 show the UWB anchors in the X-ray test lab.

Sequentially, the range between the mobile node and each anchor is measured. With a full set of three measurements the location of the mobile UWB node is estimated based on the localization algorithm from section 5.2.1. With the obtained positioning measurements all introduced tracking filters are used. Figure 8.9 shows an NDI Optotrak Certus that is used as reference system with gold standard measurement. This stereo camera system provides a spatial accuracy of 0.1 mm with a resolution of 0.01 mm.

Figure 8.7: System setup for medical environment with two reference UWB anchors mounted at the ceiling.

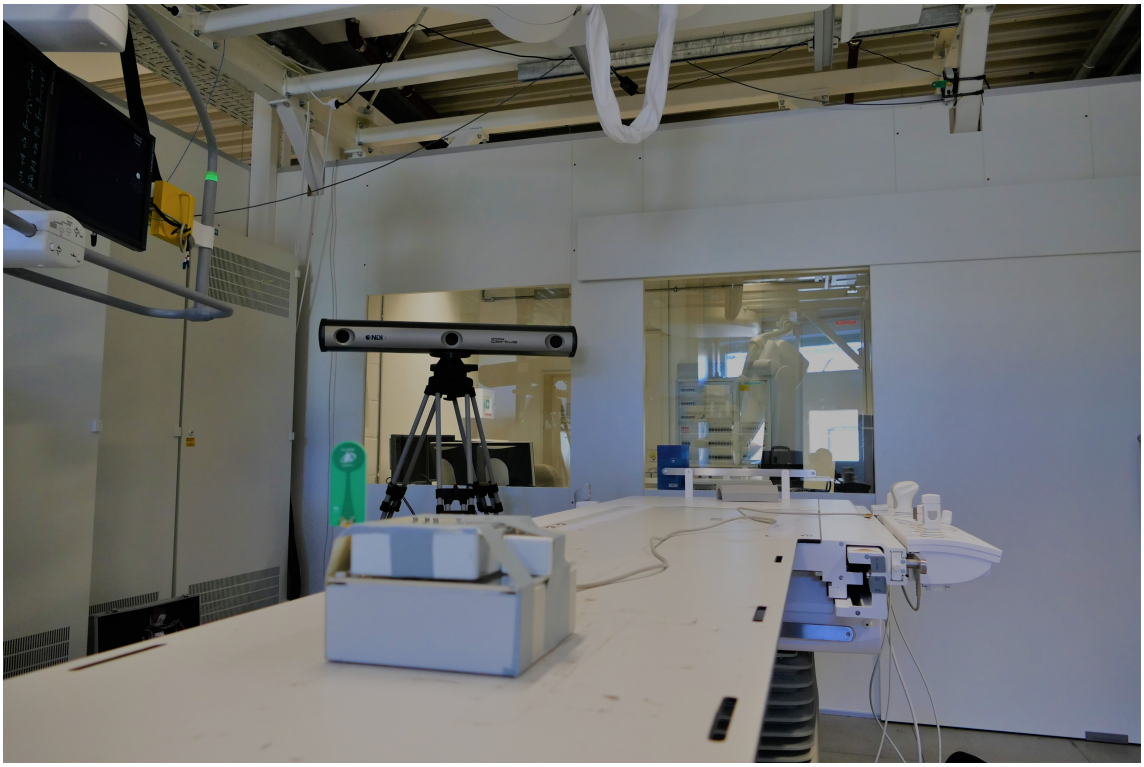

Figure 8.8: System setup for medical environment with the third reference UWB anchors mounted at the ceiling.

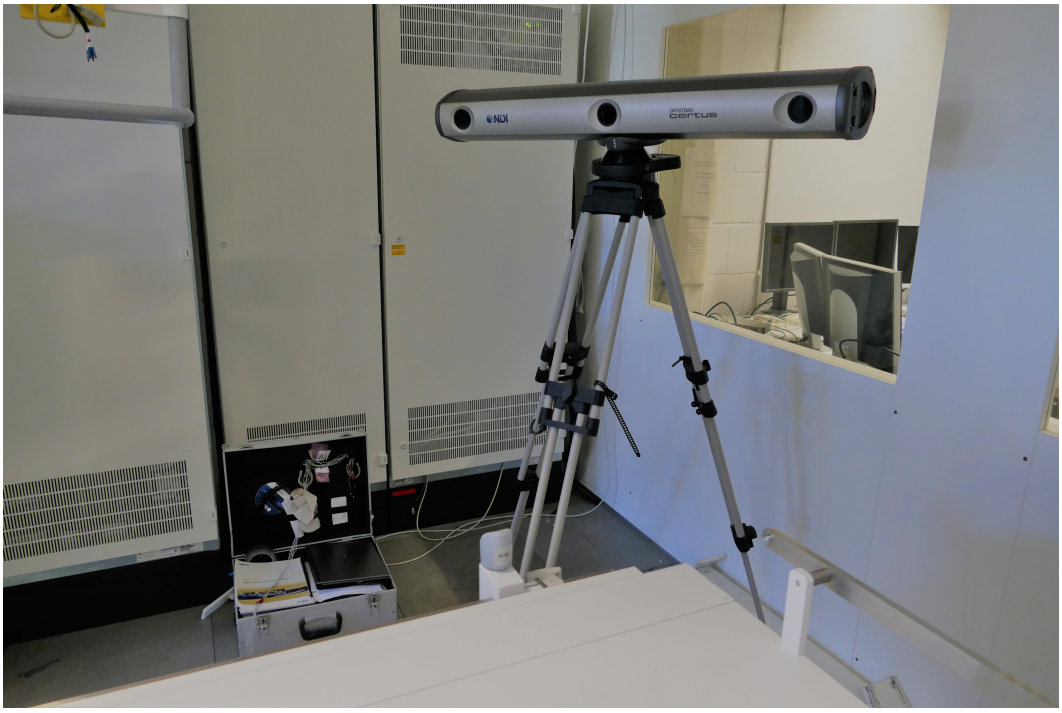

Figure 8.9: Ground truth optical tracking system Optotrak Certus by NDI positioned on a tripod in the angiography test cabin. (NDI17)

One wired active optical marker of the optical reference system is positioned in proximity to the phase center of the UWB antenna but not too close to impinge the UWB measurements. To realize both positioning systems working in the same coordinate frame they are co-registered with the Artis zeego system.

8.3 Filter Evaluation

This section describes experiments using the NDI Optotrak and the UWB localization system are conducted and the measurements are recorded respectively. Using the „SimReal“ function of the UWB framework the recorded raw measurements can be replayed with several configurations of the implemented tracking filters applied. The mobile UWB node and an Optotrak marker are located on the patient table which is moved in x- and z-direction in this experiment. The experiment comprises some movements but also static phases between movements. Figure 8.10 shows measurement results from the optical reference system and the UWB localization prototype without applied tracking filters.

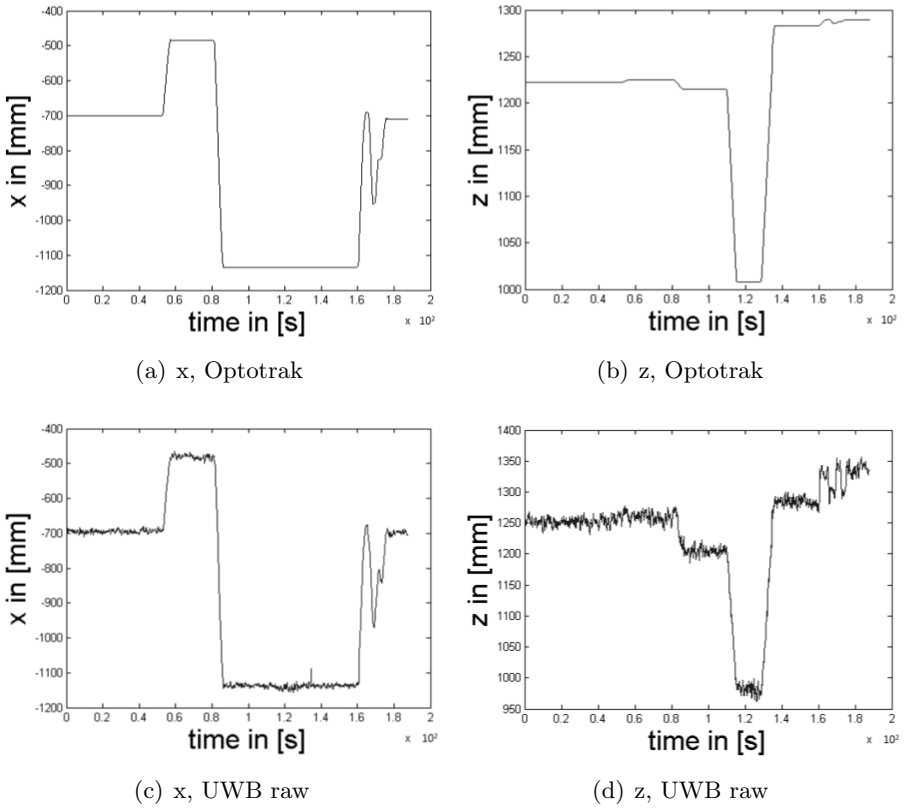

(a) x, Optotrak

(b) z, Optotrak

(c) x, UWB raw

(d) z, UWB raw

Figure 8.10: Measured NDI Optotrak and UWB raw position data.

Qualitatively it can be assumed that the UWB measurements provide the same position information in this scenario as the Optotrak but with higher measurement noise. At the same time it is can be seen that the accuracy of UWB localization results in x-direction matches the optical reference measurements better than in z-direction. This effect can be traced back to the localization approach using a spherical trilateration algorithm and the positioning of the UWB anchors at the ceiling. In this constellation the z-axis orthogonal to the anchor plane gives poorer estimation results than x- and y-axis.

For the Moving Average Filter evaluation the buffer size N is configured between 1 and 50, where 1 means UWB raw measurements given in figure 8.10. Figure 8.11 visualizes Moving Average Filter results with $N = 10$ and $N = 50$.

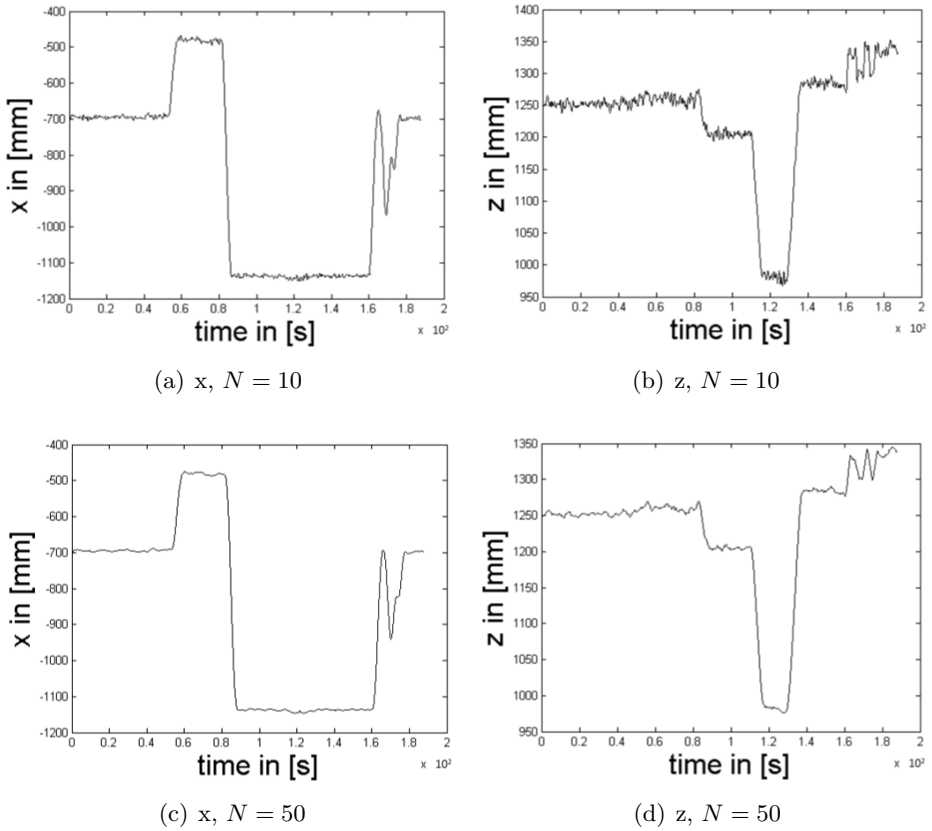

(a) x, $N = 10$ (b) z, $N = 10$

(c) x, $N = 50$ (d) z, $N = 50$

Figure 8.11: Measured UWB position data with Moving Average Filter of buffer size $N = 10$ and $N = 50$.

By increasing the ring buffer size smoother estimated filtered position results with less measurement noise can be achieved. The known drawback of inert behavior and therefore bad estimation results in movement phases due to longer ring buffer cycles does not seem to have to much of an effect in this scenario.

For the Particle Filter two parameters are configured. The particle speed is configured as $0.5\,m/s$ and $1\,m/s$. The filter width defines the width of the Gaussian distribution and is set as 50 and 500. Figure 8.12 shows particle filtered position data with $\sigma_v = 0.5\,m/s$ and different filter widths and also variation of the particle speed to $\sigma_v = 1.0\,m/s$.

It can be seen that the particle speed has no obvious impact in this scenario. It is only important for highly dynamic behavior where a slower particle speed cannot represent the UWB modules movements. The filter width does also not provide qualitatively visible differences for the position estimation.

The Kalman Filter is varied in the covariance matrix diagonal threshold ξ between 0.1 and 1. Figure 8.13 provides measurement results for different Kalman filter configurations.

The Kalman Filter overshoots at the end of a movement phase the more the smaller the ξ-value is chosen. It shows that the Kalman Filter relies more on the state than on measurement data input when ξ is small. The influence on the inertia of the filtered data can clearly be seen in figure 8.14 for ξ-values from 0.001 up to 10.

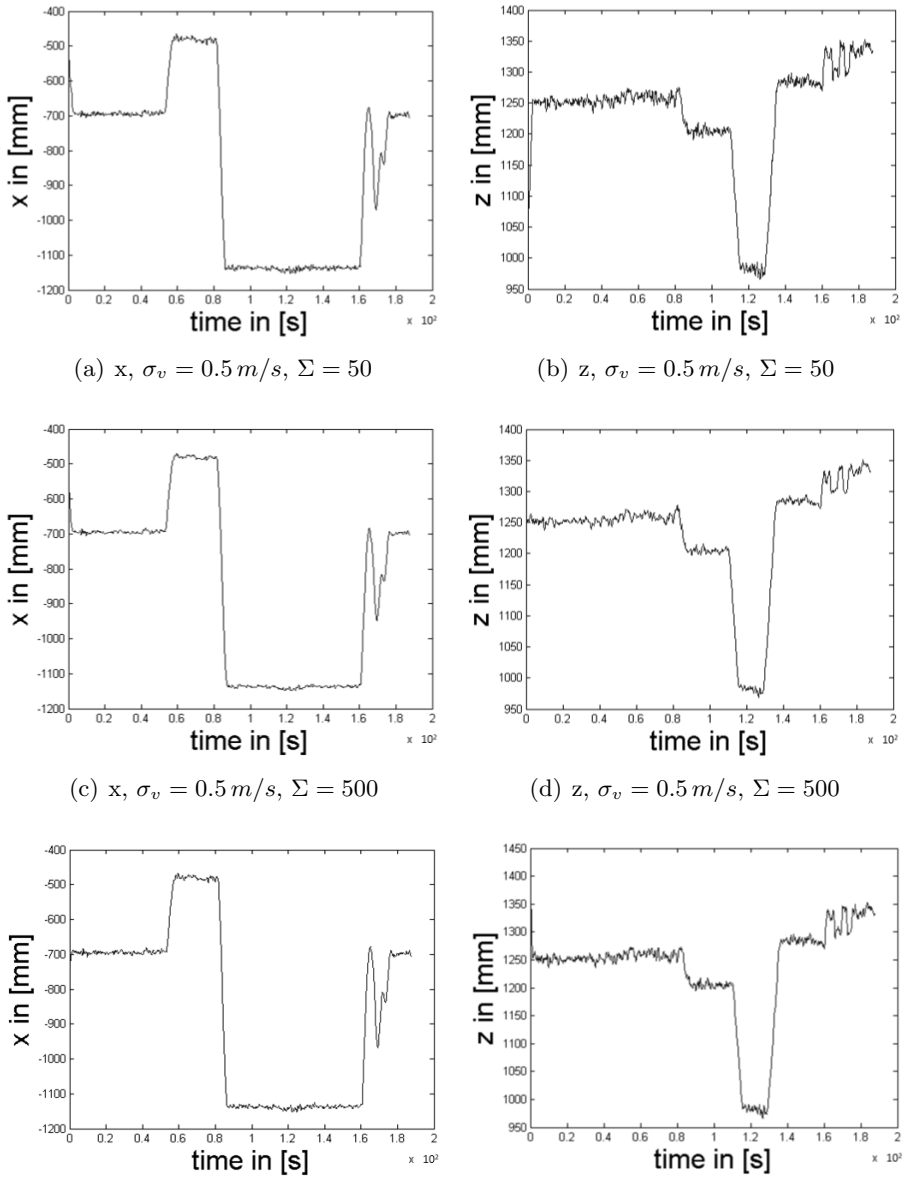

(a) x, $\sigma_v = 0.5\,m/s$, $\Sigma = 50$

(b) z, $\sigma_v = 0.5\,m/s$, $\Sigma = 50$

(c) x, $\sigma_v = 0.5\,m/s$, $\Sigma = 500$

(d) z, $\sigma_v = 0.5\,m/s$, $\Sigma = 500$

(e) x, $\sigma_v = 1.0\,m/s$, $\Sigma = 500$

(f) z, $\sigma_v = 1.0\,m/s$, $\Sigma = 500$

Figure 8.12: Measured UWB position data with Particle Filter with particle speed $\sigma_v = 0.5\,m/s$ and filter width $\Sigma = 50$, particle speed $\sigma_v = 0.5\,m/s$ and filter width $\Sigma = 500$ and particle speed $\sigma_v = 1.0\,m/s$ and filter width $\Sigma = 500$ respectively.

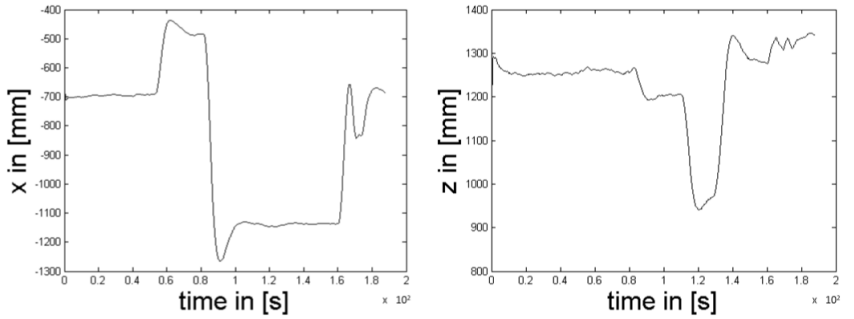

(a) x, $\xi = 0.1$ (b) z, $\xi = 0.1$

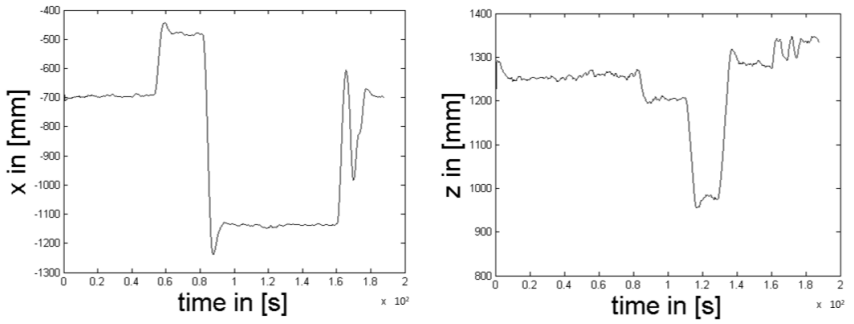

(c) x, $\xi = 1.0$ (d) z, $\xi = 1.0$

Figure 8.13: Measured UWB position data using Kalman Filter with ξ of 0.1 and 1.0.

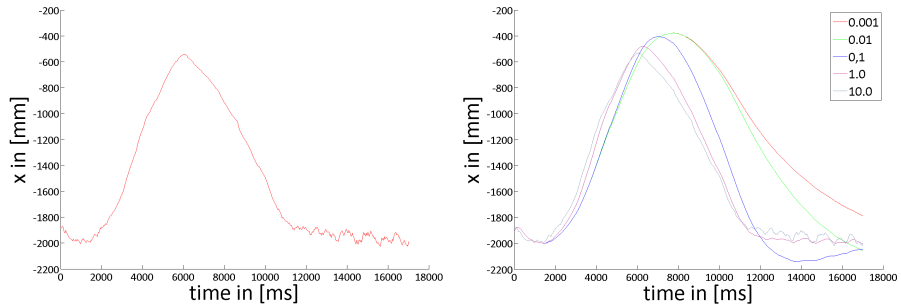

(a) Raw data, x (b) Kalman filtered data, x

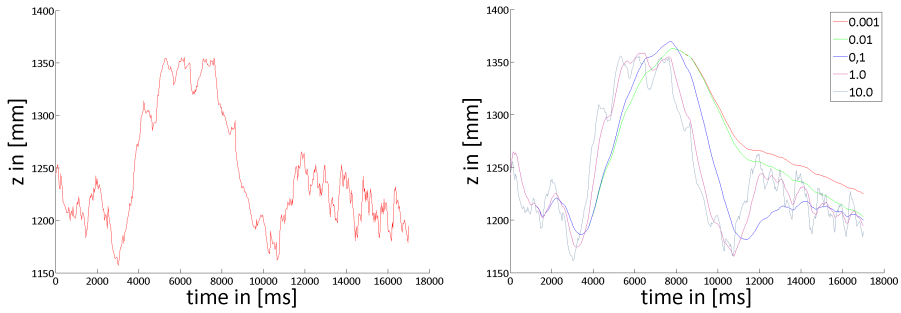

(c) Raw data, z (d) Kalman filtered data, z

Figure 8.14: Measured UWB x-position data for raw data and Kalman filtered data with different ξ-values.

8.4 Filter Comparison

This section is dedicated to positioning performance regarding accuracy and precision of the UWB localization prototype in static and dynamic measurement scenarios in the proposed medical system setup. The mobile UWB node including the reference marker is placed on the tabletop of the patient table. For the static scenario six table positions are used with a long rest phase after each movement before the actual measurement for this static position starts. The position error ϵ between one position result of UWB localization and optical reference system is calculated from equation (8.3).

$$\epsilon = \sqrt{(\hat{x} - x)^2 + (\hat{y} - y)^2 + (\hat{z} - z)^2} \tag{8.3}$$

For comparability reasons a root mean square error based on equation (8.2) on page 70 is used. The estimated position of the reference system is denoted as $(\hat{x}, \hat{y}, \hat{z})$ whereas the tracking result of the UWB prototype is given with (x, y, z) and the number of measurements at this position is given with N. Equation (8.4) provides the positioning precision based on the deviation of the position accuracy ϵ regarding the mean position error $\bar{\epsilon}$ for N samples.

$$\sigma_\epsilon = \sqrt{\frac{\sum_{n=0}^{N} (\bar{\epsilon} - \epsilon_n)^2}{N}} \tag{8.4}$$

In figure 8.15 localization results for static position 1 are shown.

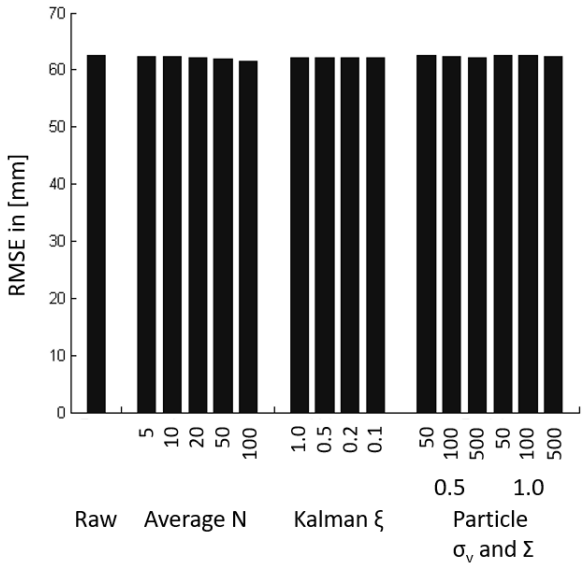

Figure 8.15: „Distribution of the positioning accuracy for raw UWB localization data and selected filter configurations for position 1. From left to right, for the Moving Average Filter the sample size N increases from 5 to 100, for the Kalman Filter the dynamic factor ξ increases from 0.1 to 1.0 and for the Particle Filter the particle velocity σ_v and the covariance matrix Σ are varied from 0.5 to 1.0 and 50 to 500 respectively.“(BKR15)

It can be seen that the positioning error of the UWB prototype compared to the optical reference system is comparable over all options independent of the applied tracking filter. Figure 8.16 shows the exemplary position error for raw and one Kalman filtered data set. Applying a tracking filter has noticeable impact on the precision σ_ϵ of the localization prototype.

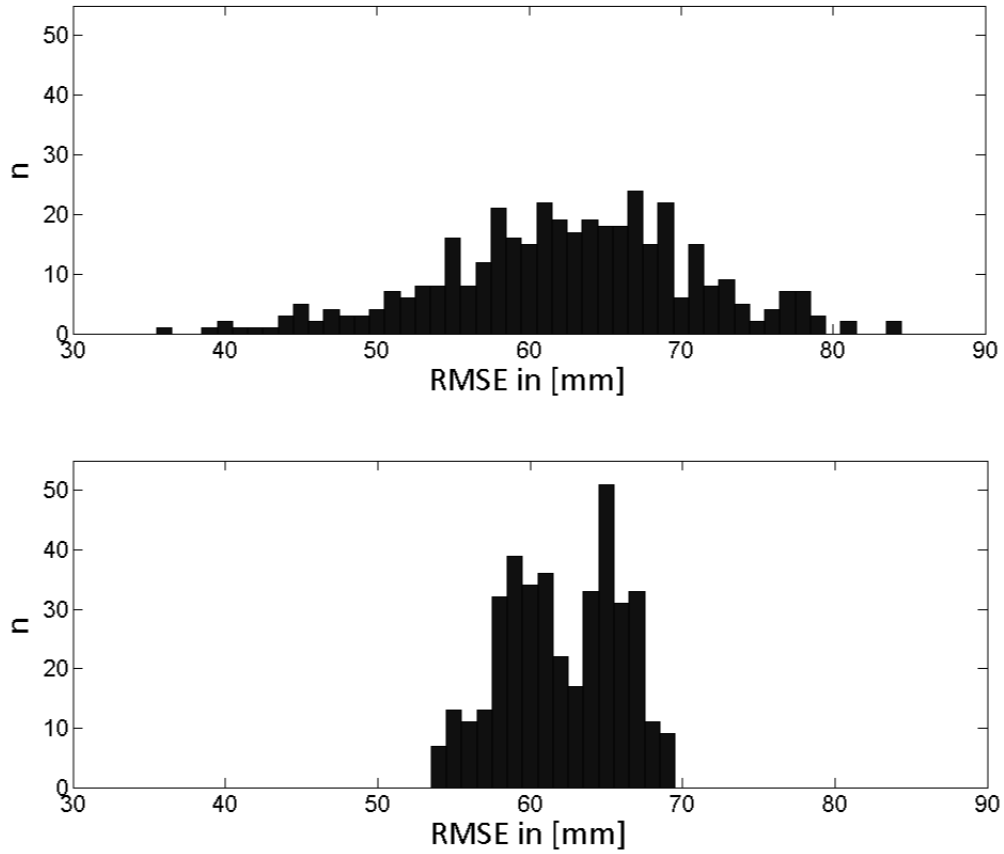

Figure 8.16: Error distribution for raw UWB positioning and Kalman filtered data for position 1. (BKR15) ©2015 IEEE

Figure 8.17 shows position precision results for position 1. The effect of the filters tuning factors can easily be seen. Tracking filters tuned to resemble dynamic behavior perform worse than those tuned to resemble static behavior.

Figure 8.18 provides information on position errors for all six static positions done in this experiment. The position error ranges from 35 to 42 mm. For the most static tuned Kalman Filter a higher error can be seen although it was stated that the applied filter does not have an influence on the accuracy. This is due to the set up of the experiment. With dynamic factor $\xi = 0.1$ the long rest phase before starting the measurement is not enough for the very inert behavior of this filter to swing back to the actual position. A similar overshooting can be seen in figure 8.14 on page 80 for the Kalman filtered x-values and low values for ξ.

Figure 8.19 shows position precision results for all six static positions. It can be seen that the Kalman Filter's inert behavior with $\xi = 0.1$ also results in decreased precision.

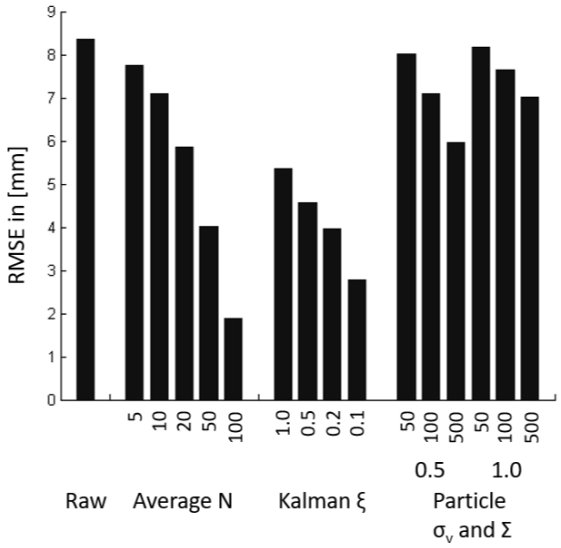

Figure 8.17: „Distribution of the positioning precision for raw UWB localization data and selected filter configurations for position 1. From left to right, for the Average filter the sample size N increases from 5 to 100, for the Kalman filter the dynamic factor ξ increases from 0.1 to 1.0 and for the Particle Filter the particle velocity σ_v and the covariance matrix Σ are varied from 0.5 to 1.0 and 50 to 500 respectively.“(BKR15) ©2015 IEEE

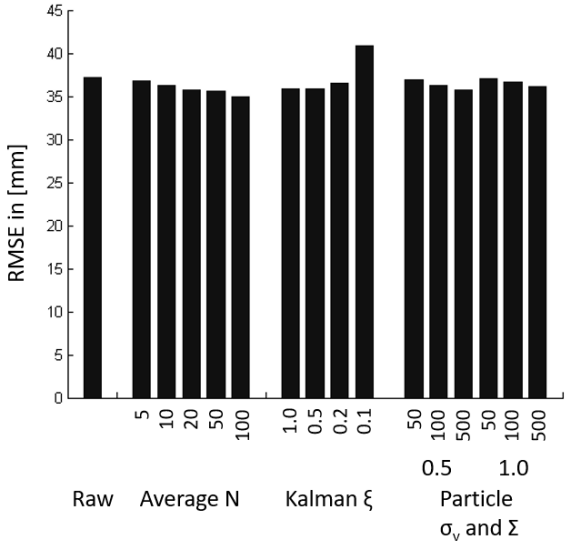

Figure 8.18: „Distribution of the positioning accuracy for raw UWB localization data and selected filter configurations for all positions. From left to right, for the Average filter the sample size N increases from 5 to 100, for the Kalman filter the dynamic factor ξ increases from 0.1 to 1.0 and for the Particle Filter the particle velocity σ_v and the covariance matrix Σ are varied from 0.5 to 1.0 and 50 to 500 respectively.“(BKR15) ©2015 IEEE

Moving Average and Kalman Filters outperform raw measurements and Particle Filters for the conducted evaluation in a static scenario. It can be seen that the parameter tuning of the tracking filters has great impact on the dynamic behavior and therefore the localization

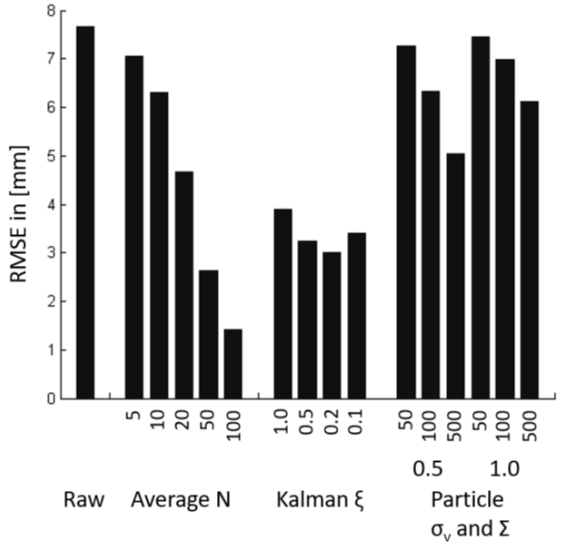

Figure 8.19: „Distribution of the positioning precision for raw UWB localization data and selected filter configurations for all positions. From left to right, for the Average filter the sample size N increases from 5 to 100, for the Kalman filter the dynamic factor ξ increases from 0.1 to 1.0 and for the Particle Filter the particle velocity σ_v and the covariance matrix Σ are varied from 0.5 to 1.0 and 50 to 500 respectively.“(BKR15) ©2015 IEEE

results. The results for a dynamic scene can be seen in figure 8.20. Exemplary, the Moving Average Filter with different sizes N is used. It can be seen that there is no overshooting with the Moving Average Filter in contrast to the Kalman Filter. It can also be derived that N has an impact on the inert behavior of the filtered results of the positioning system. This can be explained with the number of measurements used in the ring buffer to estimate to current position. The speed of position estimates ranges from 33 to 55 ms and therefore 30 and 18 Hz update rate depending on computational performance. With a Moving Average Filter of size $N = 100$ this results in 3.3 to 5.5 s until each value in the ring buffer is replaced.

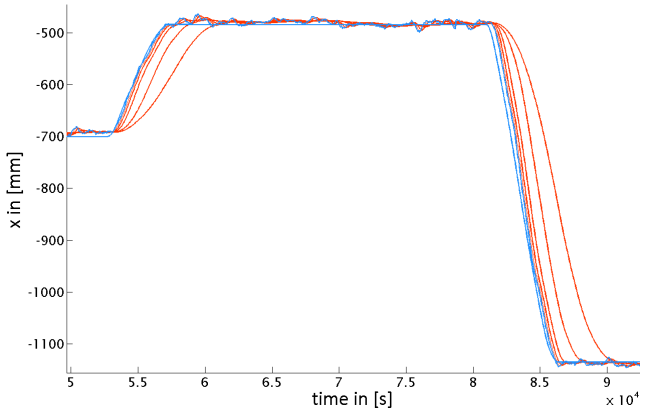

Figure 8.20: UWB localization in a dynamic setup where the Optotrak reference measurements and UWB raw data are given in blue whereas red represents various tuned Moving Average filters. (BKR15) ©2015 IEEE

9 Results and Discussion

The developed UWB localization prototype is described in depth and evaluated heavily by using simulations and real measurements in a medical environment. From the results it is clear that UWB localization can be used to estimate the position of a mobile UWB module. With only three UWB anchor nodes in a highly reflective environment it provides reasonable position results compared to a highly accurate and precise optical reference system. Processing the raw UWB data with applied tracking filters outperforms raw position estimation without filters in the conducted static scenario measurements. Position accuracy for raw and filtered data result in approximately $35\,mm$. This confirms the fact that filter techniques only have an influence on the distribution of the error not on the absolute value. Using tracking filters the position precision is halved from over $7\,mm$ in medium tuned cases and reduced to only $1.4\,mm$ using excessively tuned filtering. This improvement in precision goes hand in hand with a reduction of dynamic behavior for the UWB localization. Since the medical environment comprises many mobile objects the dynamical behavior of the localization system is of high importance. To overcome this drawback, further improvements on the localization system are pursued. In part IV, an extension of the UWB localization system with external sensor data is presented that aims for the current weak point of dynamic behavior combined with high precision for position estimation.

Part IV

Dynamic Radio Location Prototype

10 External Sensors

To handle the drawbacks of the UWB radio location prototype introduced in part III, a sensor fusion approach implementing an additional external sensor with a different sensor technology to support the UWB sensors is pursued. The goal is to overcome the currently implemented fixed filter tuning that controls the dynamics of position estimation. To realize precise results in static scenarios but also an instant adaption to movements in a dynamic environment a second source of information is needed. In 10.1 selected types of external sensors are introduced and compared. We shed a light on two explicit implementations of appropriate sensor types in 10.2. In 10.3 the introduced external sensors are compared and tested for their suitability to extend the UWB localization system by two experimental studies. A short conclusion on external sensors is given in 10.4.

10.1 Overview

There is a great variety of sensors available that can be utilized to deduce valuable information for localization and positioning. The underlying goal is having a complement for the existing UWB localization system for indoor use in a dynamic, harsh and crowded medical environment. Therefore the sensor should not exceed the dimensions of an UWB sensor node. Ideally the external sensor is easily integrable into the existing localization system. In (BFW97), seven categories of positioning systems are defined:

1. Odometry
2. Inertial Navigation
3. Magnetic Compasses
4. Active Beacons
5. Global Positioning Systems
6. Landmark Navigation
7. Map-Based Positioning

Each category can be composed of different sensor technologies and not all categories are suitable to complement the UWB localization system. The seven categories can be arranged in two groups regarding the localization and positioning result they give (BEF$^+$96). The first two categories, introduced in 10.1.1, are types of relative position measurements or dead

reckoning. The third to seventh category belong to the absolute or reference-based positioning systems, described in 10.1.2. In 10.1.3 a short conclusion on external sensors is given.

10.1.1 Dead Reckoning

Dead Reckoning describes the relative position estimation based on incremental motion information over time regarding a previous position. This approach is very sensitive towards orientation and speed errors. Every error in the first place cumulates for later results since the current position is used as previous position in the next position estimation step.

Odometry makes use if direct data from the respective driving technology to estimate position changes over time. For cars or mobile robots this often is the revolution of wheels that is measured by encoders. Together with the circumference of the wheel, the distance traveled is computed. For persons and legged robots the distance traveled is calculated by the number of steps and the corresponding step length. This only gives information of the distance traveled and needs to be combined with sensor technologies to deduce the heading direction to get a relative position. The objects equipped with an UWB localization system are of very different kinds and do most likely not have active drives. Since we seek a general external sensor solution to complement UWB localization, Odometry is not suitable.

Inertial Navigation makes use of motion and rotation sensors to calculate the speed and heading direction of the object to be localized and estimates the relative position from this information. Compared to Odometry, inertial navigation systems directly measure physical parameters of the moving object. To deduce relative position data from the quantity to be measured, the measurements are once or two times integrated.

An accelerometer measures the acceleration that affects itself. An acceleration sensor that is properly calibrated gives a result of $9.81 m/s^2$ for the upright direction in a static scenario on a surface. This acceleration value resembles the gravity of Earth. There are exceptions from this characteristic, for example the eddy current based Ferraris sensors that only measures relative accelerations between two components. Nevertheless, most common used acceleration sensors are not independent of the standard acceleration due to gravity since they use a mass-spring system mounted with one sensitive direction. To be able to realize very small designs, the acceleration sensors are build as micro-electro-mechanical systems (MEMS). This allows for miniaturization of the mechanical structures in the dimension of micrometers and to integrate it on a chip. Figure 10.1 shows a MEMS structure to realize an accelerometer. A macroscopic gyroscope commonly consists of a spinning wheel that can move freely to any orientation in its mounting. This instruments are often used as sensors in airplanes, spacecrafts or military applications. On the on hand they are very precise, on the other hand they are expensive and have a quiet big design. Like accelerometers, gyroscopes can also be build up as MEMS. In this configuration they can be understood as an extension of an acceleration sensor. One

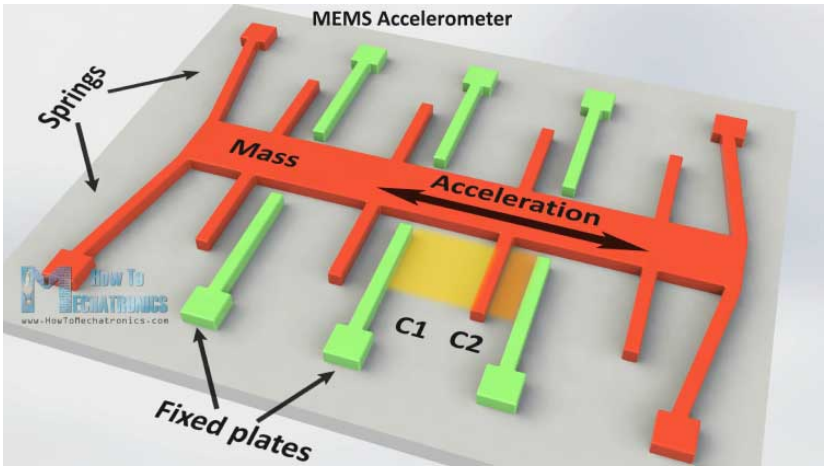

Figure 10.1: Schematic structure of a MEMS accelerometer build up on a substrate (grey). There is a fixed structure (green) on the substrate and a movable mass held by springs (red) to provide one degree of freedom. With acceleration applied to the sensor, the movable mass is displaced. This results in a change of the capacity between fixed and movable structure. From the measured capacity the acceleration can be derived. (Dej16)

type of gyroscopes uses two masses that are moveably mounted in perpendicular directions. In this composition the Coriolis effect is exploited to measure the angular rate. Figure 10.2 gives a schematic view of a MEMS gyroscope with a two mass system.

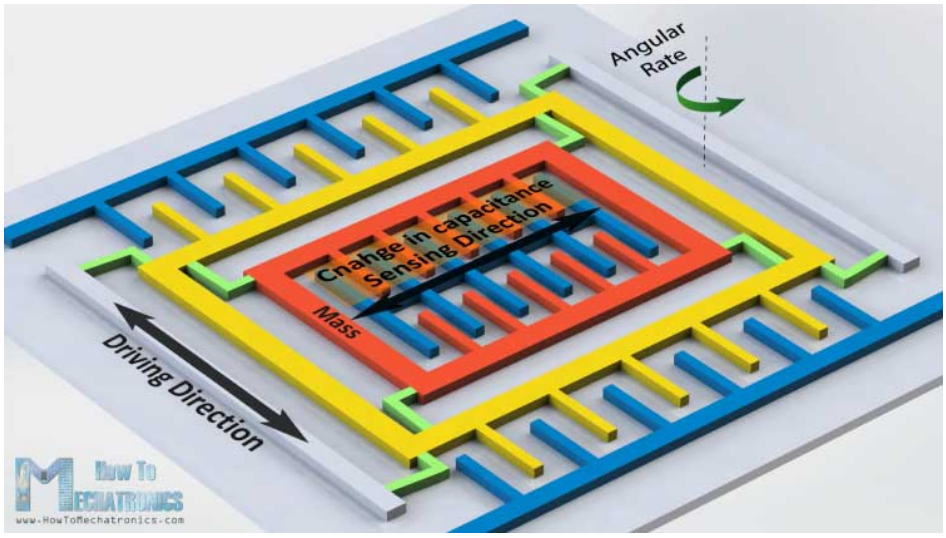

Figure 10.2: Schematic structure of a MEMS gyroscope. There are several fixed structures (blue) providing one part of the capacities. Having one mass oscillating in the direction of its degree of freedom (yellow) and exert a perpendicular force by an angular rate, the second mass (red) is affected by this force and therefore displaced. Both masses are moveably mounted using springs (green). With the inner mass moving, the capacity change can be measured and therefore the angular rate can be estimated. (Dej16)

10.1.2 Reference based Systems

Reference based systems give absolute measurement information regarding a specified coordinate frame. Unlike dead reckoning systems, they do not rely on a previous position to estimate information relative to that. Measurements are directly given in a specific coordinate frame which is given by the references.

Magnetic Compasses can be used to measure the earth's magnetic field. Common magnetometers use the Hall Effect to estimate the magnetic field. Other implementations use for example the magneto resistive effect or a fluxgate compass. Figure 10.3 gives an example for a hall effect magnetometer and its working principle. As a drawback, magnetic compasses are highly effected by other magnetic fields caused by magnetic materials or electromagnets.

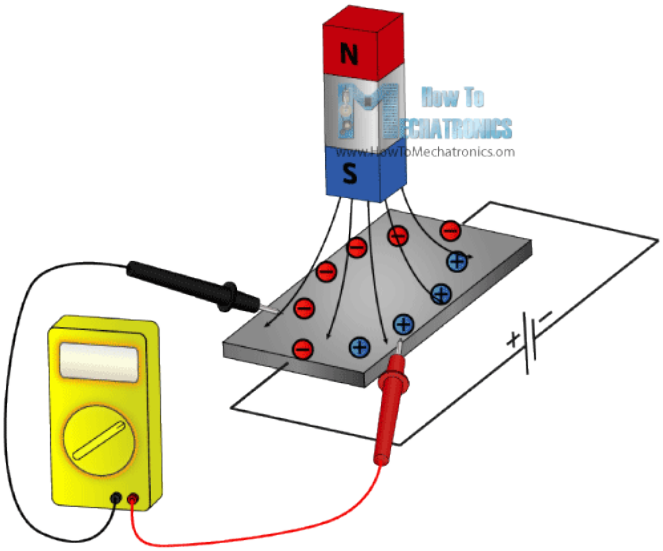

Figure 10.3: Magnetic Compass using the Hall Effect to determine the magnetic field. The magnetometer comprises a conductive plate (grey) with an electric current to flow through it. A magnetic field disturbs the flow of the electrons inside the conductor and applies a Lorentz force which results in a displacement of the electrical flow perpendicular to the magnetic field and the current flow. This results in a separation of charge alongside the conductor which can be measured as a voltage representing the strength of the magnetic filed. (Dej16)

Active Beacon navigation systems can be used implementing several sensor technologies. The provided UWB system belongs to this group of navigation or localization sensor systems. The beacons, in this case the UWB modules, actively send a signal to the tracked object and use this information for the localization. Optical triangulation systems are also counted as active beacons. Since our localization prototype already comprises one active beacon technology and alternatives are already discussed in 1 this can be skipped here.

Global Positioning System or GPS is the state of the art localization system for outdoor navigation. It comprises 24 satellites as reference stations with time of flight and trilateration to estimate the position of the receiver. Due to the fact that GPS is most likely not available in indoor scenarios it cannot be used as extension for this localization prototype.

Landmark Navigation unlike active beacons uses passive information for localization purpose. These landmarks can be specific geometric objects with a distinct shape or additional information from e.g. bar-codes. Landmarks are placed at fixed and known positions and have to be easy to identify by the sensor technology used on the object to be tracked. The position accuracy of the landmarks is a crucial factor on the localization accuracy with this approach. The amount of landmarks in range of the sensor is also important. The more landmarks are available in the field of view, the better the positioning result is. On the object to be tracked a sensor technology to sense the landmarks is needed. Often an optical camera approach is pursued to either find geometric features or a bar-code.

Map-Based Positioning differs from landmark navigation in the point that no distinct shapes or objects are used as reference, but features from the whole local environment. Commonly used are laser range sensors to build up the map for the current object position. This information can be compared to a previously stored map which for example can be generated from a CAD model.

10.1.3 External Sensors - Conclusions

From the introduced seven fields for localization and navigation technologies only two seem to be of additional value for the UWB localization system. For Odometry wheel revolution or step length need to be available which is not necessarily given for the objects to be tracked in medical environment. GPS is not feasible since it is not available in indoor scenarios. UWB itself being an active beacon based system cannot gain that much additional and non redundant information from another system of the same kind. In chapter3 different active beacon technologies are already introduced and UWB found out to be the most promising one. Map-based positioning needs a map with clear and fixed features to extract. In the crowded and dynamic medical environment this can not be guaranteed. For landmark based approaches a sensor, e.g. a camera, is needed on the object to be tracked. This is not a feasible solution to be integrated with the UWB system where the board can be hid in the tracked object and only the antenna needs to be electrically visible. Other landmark solutions with e.g. RFID are radio location technologies exposed to the same environmental influences like UWB, providing the same type of information, here position, and found out to result in inferior positioning results.

Due to the possibility to build inertial sensors like accelerometers and gyroscopes in MEMS technology with small designs and their ability to provide direct information on the movement

or movement change of the object mounted on, they are a reasonable extension of the UWB localization system that provides a different type of information to complement the UWB position information. Magnetic compasses provide a good extension of the possibilities of inertial navigation systems and can thus be also of interest for the presented localization prototype.

10.2 Inertial Measurement Units

To experimentally evaluate the proposed sensor fusion approach using accelerometers, gyroscopes and magnetometers two different industrially available sensors are implemented. One of the sensors is a basic implementation that provides acceleration information in 3 dimensions of freedom (DOF). The other sensor is a state of the art sensor combination that comprises 9 dimensions of freedom with accelerometer, gyroscope, magnetometer and a microcontroller to postprocess and combine measurements in one chip.

First the simple triaxial acceleration sensor (SMB380) from Bosch Sensortech GmbH is presented (Bos17). The SMB380 has a small footprint of $3.0 \times 3.0\,\mathrm{mm}^2$ with 0.9 mm height. It provides 10 bit resolution for acceleration data and different measurement ranges where the smallest range with $\pm 2\,g$ is the most suitable one for the pursued application. The SMB380 sensor is implemented in the JoyWarrior24F8 by Code Mercenaries Hard- und Software GmbH that realizes the power supply, input and output communication for the sensor (Cod17). Figure 10.4 visualized the accelerometer in the used enclosure.

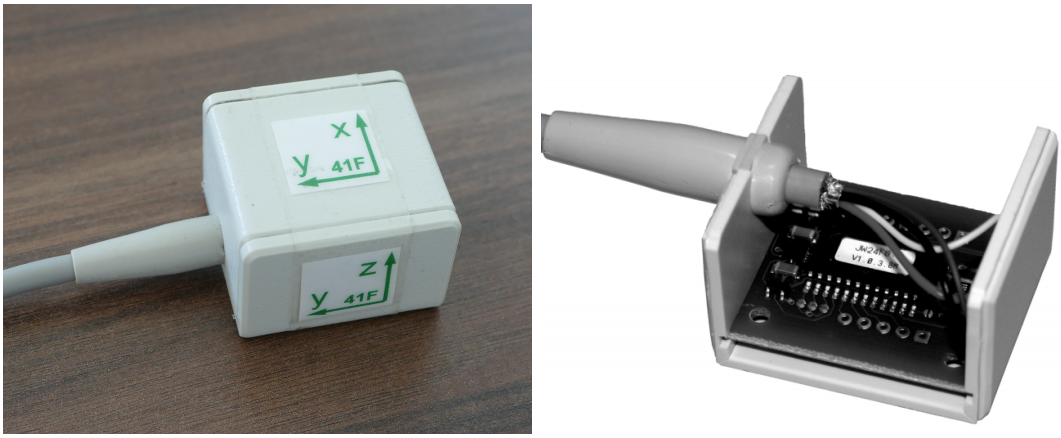

(a) Sensor in enclosure (b) Sensor open

Figure 10.4: 3 DOF Sensor with indicated orientation on enclosure.

The BNO055 by Bosch Sensortech GmbH is claimed as „Intelligent 9-axis absolute orientation sensor“ with 9-axis sensor fusion (Bos17). It has a footprint of $3.8 \times 5.2\,\mathrm{mm}^2$ with 1.13 mm height. This is double the size of the SMB380 but still small compared to the P410 UWB module. The BNO055 provides 14 bit resolution for acceleration data with the smallest range of $\pm 2\,g$, 16 bit for the gyroscope with ranges from $\pm 125°/\mathrm{s}$ to $\pm 2000°/\mathrm{s}$ and $\sim 0.3\mu\mathrm{T}$ for the magnetometer. For the pursued application the smallest gyroscope measurement range can

be chosen to get the best resolution since we do not expect high-speed rotations. For the sensor output several non-fusion and fusion modes can be chosen. To make the most use of all measured sensor data the NDOF fusion mode that combines all nine dimensions of freedom is used and results in absolute acceleration and orientation measurements with an output rate of 100 Hz that already compensates for the gravity of Earth. For the UWB-IMU fusion approach the BNO055 is implemented in an Xplained Pro wingboard to be compatible with the Atmel Xplained Pro evaluation board shown in figure D.1 (Atm17). The wingboard is given in figure 10.5 and provides the powering, input and output communication for the sensor.

Figure 10.5: 9 DOF Sensor Wingboard Xplained Pro by Atmel. (Atm17)

To protect the electronics from environmental effects a robust housing is build that could also hold additional wingboards with other functionalities provided. Figure 10.6 shows the whole 9 DOF IMU with housing.

Figure 10.6: 9 DOF Sensor Setup of the electronics in a robust housing.

10.3 Experiments

To compare the 3 DOF and 9 DOF inertial measurement units, experiments in a static and a dynamic scene were conducted. The UWB localization system and the IMUs are positioned in a medical environment comprising a cone-beam CT, a patient table, a ceiling mounted display, lead shielded walls and several assets. The external sensors are positioned on the patient table and fixed with tape to the UWB localization system. Figure 10.7 shows the combined sensor setup on the patient table.

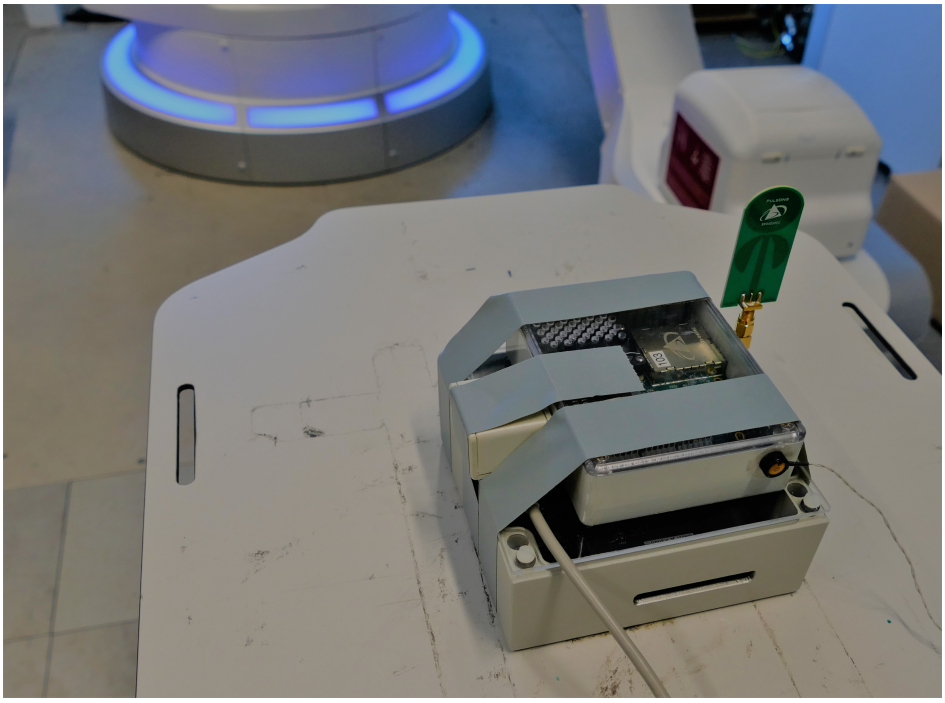

Figure 10.7: Combined sensor setup on patient table in medical environment comprising the P410 UWB module, both IMUs and an Optotrak optical marker.

For the sensor fusion approach it is of high interest whether the object to be localized is in motion or not to adapt the Kalman Filter. In equation (10.1) the absolute acceleration is estimated from the acceleration in x-, y- and z-axis. After that the acceleration of gravity is subtracted.

$$a_{abs} = \sqrt{a_x^2 + a_y^2 + a_z^2} - g \tag{10.1}$$

This simple approach is only valid when the absolute acceleration of the object and the acceleration of gravity effect in the same direction. Otherwise a vector-based approach as stated in equation (10.2) would be needed. For this vector-based approach the orientation of the absolute acceleration is needed.

$$a_{abs} = \sqrt{(a_x - g_x)^2 + (a_y - g_y)^2 + (a_z - g_z)^2} \tag{10.2}$$

For the 9 DOF IMU all needed values are measured and available. For the 3 DOF acceleration only sensor, a high pass filter like a butterworth filter could be applied. In the conducted two measurement scenarios it can be guaranteed for the absolute acceleration and the acceleration of gravity to be aligned so we do not need to account for counter measures here.

From the static scenario measurements the quality of the calibration of the sensors and the noise behavior can be deduced. For the dynamic scene the patient table is moved to six different heights over a time of approximately 55 seconds with plateau phases of several seconds at each position. The measurement results from the dynamic scene give information about the signal response of the IMU. Combining the noise and signal response results of static and dynamic scenes the signal to noise ratio (SNR) can be derived as a basis for decision whether the inertial sensor is appropriate to support the UWB localization system or not.

In figure 10.8 the UWB position data for the static scenario is given for x-, y- and z-axis. It can be easily seen that in the static scenario the measurements move in a range of $\pm 3cm$ maximum error around the median value for each axis.

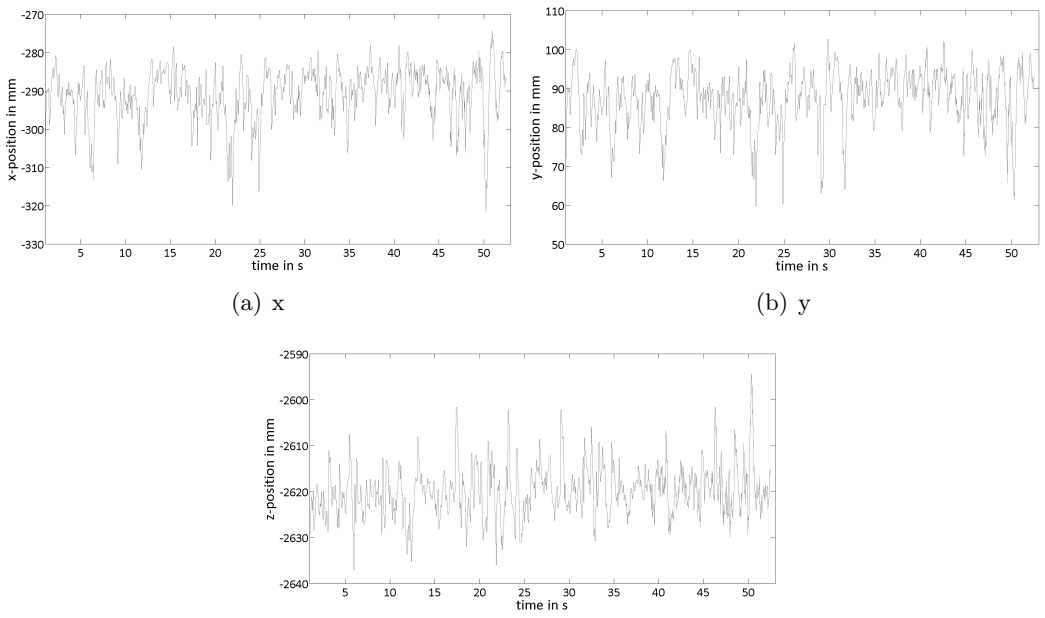

(a) x

(b) y

(c) z

Figure 10.8: Static measurement campaign to evaluate and compare 3 DOF and 9 DOF IMUs. Shown are the UWB measurements for approximately 55 seconds of no motion of the patient table.

Acceleration measurement results for the static campaign are given in figure 10.9. Since the acceleration data is given as absolute value no negative acceleration values appear. It can be seen that the 3 DOF acceleration sensor is affected by an approximately ten times higher mean error than the 9 DOF sensor unit.

A detailed comparison of the behavior in static scenario can be seen in table 10.1. From the mean acceleration value the quality of the calibration can be deduced. The expected value

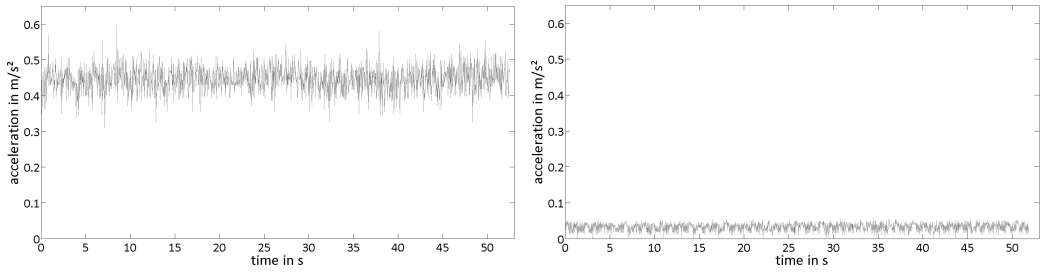

(a) 3 DOF, *acceleration* (b) 9 DOF, *acceleration*

Figure 10.9: Absolute acceleration measurement results for 3 DOF and 9 DOF sensor units in static scenario.

for the static scenario is of course $0\,m/s^2$. The 9 DOF sensor units acceleration results are one magnitude better than the 3 DOF sensor unit. The standard deviation for acceleration measurement gives information about the noise sensitivity of the sensor. The 9 DOF IMU gives three times better results than the 3 DOF sensor in this category.

Table 10.1: Statistical evaluation of IMU acceleration measurement in static scenario

	$\bar{a}$ $[m/s^2]$	std $[m/s^2]$	var $[m^2/s^4]$
3 DOF	0.446	0.0372	$1.35\,\exp -3$
9 DOF	0.032	0.0119	$1.41\,\exp -4$

Additionally to the measured acceleration data its corresponding derivative with respect to time, the jerk, is computed. It can be used as a good indicator for motions where acceleration does not lead to reliable conclusions. Figure 10.10 shows the derived jerk data for the static scenario. Comparable to the acceleration data, the 9 DOF sensor unit obviously gives better results than the 3 DOF sensor unit.

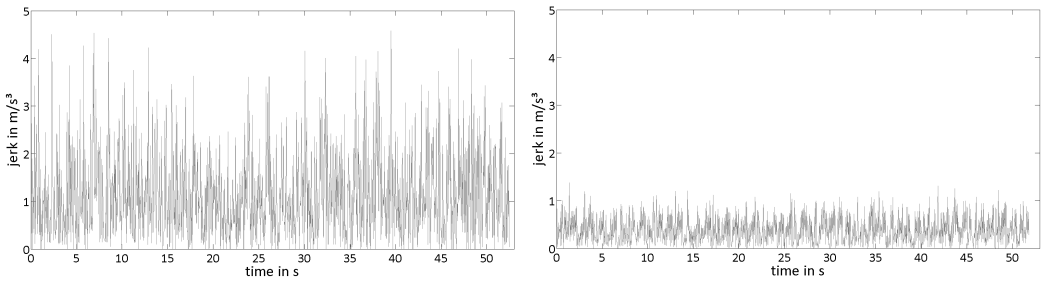

(a) 3 DOF, *jerk* (b) 9 DOF, *jerk*

Figure 10.10: Absolute derived jerk results for 3 DOF and 9 DOF sensor units in static scenario.

In table 10.2 jerk data of both IMUs is compared. As for the acceleration, the expected value for the jerk is $0\,m/s^3$. The results again are many times more accurate for the 9 DOF than 3 DOF sensor unit. The standard deviation as indicator for the noise behavior gives three times better results for the 9 DOF sensor unit. Approximately the same ratio goes for the jerk mean value as indicator for the calibration of the sensors.

Table 10.2: Statistical evaluation of IMU jerk measurement in static scenario

	$\bar{j}$ $[m/s^3]$	std $[m/s^3]$	var $[m^2/s^6]$
3 DOF	1.368	0.9126	0.833
9 DOF	0.408	0.2899	0.084

In figure 10.11 the UWB position data for the dynamic scenario is given for x-, y- and z-axis. Here the data from the 3 DOF run is visualized as representative of a dynamic scene. The motion profile for the 9 DOF sensor looks similar. For the dynamic scenario the patient table is only moved up and down which results mainly in a movement in x-direction in the coordinate frame of the measurement system. Overall the measurements in y- and z-axis move in a range of $\pm 3.5\,cm$ maximum error which is comparable to the static measurement campaign.

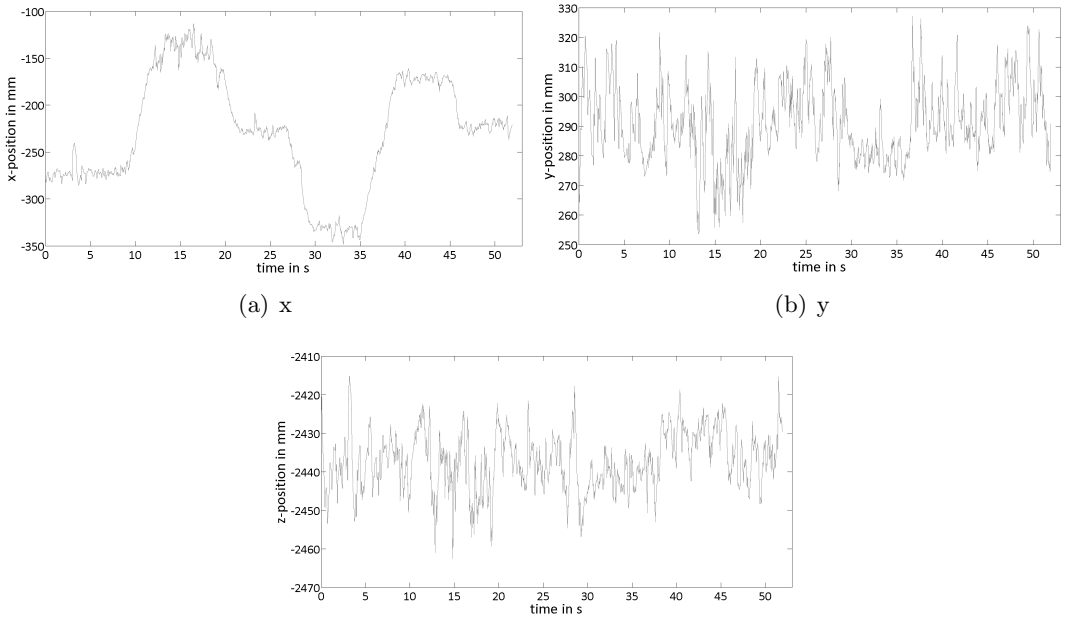

(a) x

(b) y

(c) z

Figure 10.11: Dynamic measurement campaign to evaluate and compare 3 DOF and 9 DOF IMUs. Patient table movement with static phases at six different table heights.

Figure 10.12 shows the results for acceleration measurements in the dynamic scenario. For the 3 DOF sensor unit the static offset from $0\,m/s^2$ already seen in the static campaign is again existent. The mean acceleration value in the static phases for the 9 DOF sensor unit can be estimated to be ten times smaller compared to the 3 DOF sensor. This observation is analogous to the static measurement campaign. The peaks of the acceleration when the table starts moving to the next position can easily be seen. The points of deceleration and end of motion can not be derived from sheer observation of the chart.

Figure 10.13 shows the corresponding derived jerk results for the dynamic campaign. The noise in the static phases gives equivalent results compared to the static scenario. The peaks of the start of a movement phase can easily be recognized. Distinguishing the end of a motion

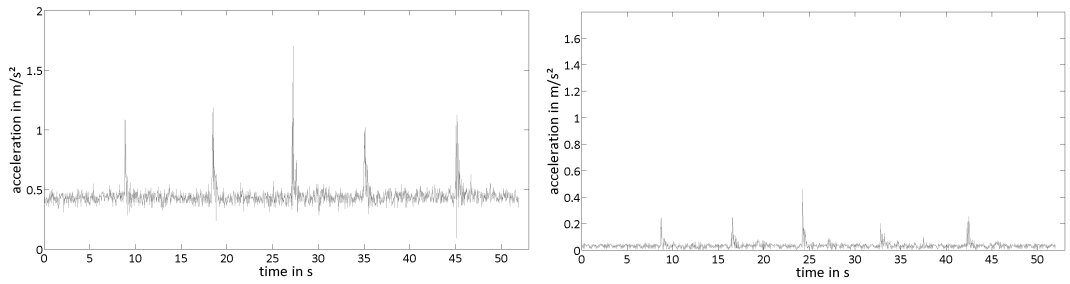

(a) 3 DOF, *acceleration* (b) 9 DOF, *acceleration*

Figure 10.12: Absolute acceleration measurement results for 3 DOF and 9 DOF sensor units in dynamic scenario.

phase apparently is not as easy. Overall the 9 DOF sensor unit gives lower amplitude results which is comparable to the acceleration behavior in figure 10.12.

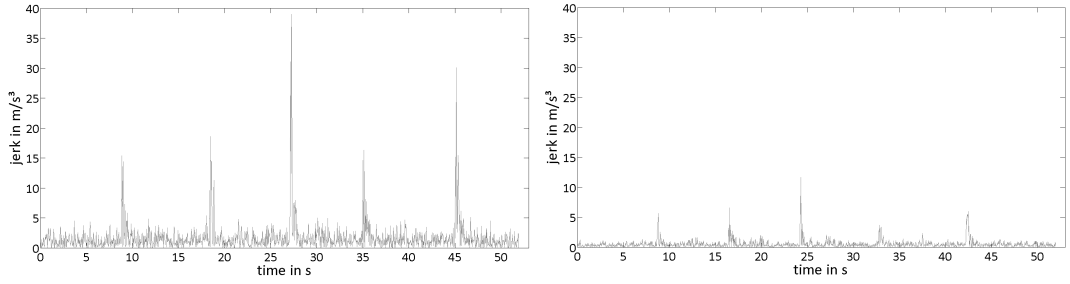

(a) 3 DOF, *jerk* (b) 9 DOF, *jerk*

Figure 10.13: Absolute derived jerk results for 3 DOF and 9 DOF sensor units in dynamic scenario.

To get a clear measure of how to realize an acceleration or deceleration phase in the motion of the patient table a new parameter is introduced. The signal to noise ratio (SNR) given in equation (10.3) provides a ratio of the signal power that holds meaningful information and the power of unwanted noise that overlays this information.

$$SNR = \frac{meaningful\ signal}{noise} \tag{10.3}$$

Meaningful information in the scope of external sensors to support the UWB localization system is to recognize a motion of the object to be tracked on the basis of acceleration and jerk data. Therefore it is essential to be able to clearly differentiate between a sensor measurement resulting from a motion or from noise. Equation (10.4) provides the definition of the SNR used in this thesis. It is shown with variables for acceleration but is also valid for jerk data when replacing acceleration for jerk.

$$SNR = \frac{a_{motion} - \bar{a}_{static}}{\sqrt{\sigma_{a,static}}} \tag{10.4}$$

A meaningful signal is described by the distance between the actual value of acceleration

or jerk and the mean acceleration value in a static case, the calibration error. This signal amplitude is compared to the standard deviation of acceleration or jerk in the static case, which provides a measure for the sensors noise.

To provide the signal to noise ratio for the measurements from the dynamic scenario, we utilize a combined visualization of motion, acceleration and jerk data received from the UWB localization system and the 3 DOF sensor unit. Figure 10.14 on page 103 provides information of the motion phases that should be identified using the external sensor data of the IMUs. The green and red dashed lines give information about the start and end of a motion phase.

Focusing on the points where a change in motion occurs, the signal amplitudes can be retrieved as one component to compute the SNR. Table 10.3 provides the acceleration and jerk amplitudes from the 3 DOF sensor unit for start and end points of every motion during the dynamic scenario. The acceleration is 2 to 3 times higher for the start of the patient table motion compared to the end, whereas for the jerk the ratio is 3 to 7.5 times respectively.

Table 10.3: Statistical evaluation of the meaningful signal in dynamic scenario for 3 DOF sensor unit

		motion ID				
motion phase	measure	1	2	3	4	5
start (green)	a $[m/s^2]$	1.08	1.19	1.70	1.02	1.12
	j $[m/s^3]$	15.37	18.62	38.96	16.32	30.09
end (red)	a $[m/s^2]$	0.51	0.56	0.54	0.54	0.54
	j $[m/s^3]$	4.82	4.79	4.98	4.67	4.50

Figure 10.15 on page 104 shows the combined visualization of position, acceleration and jerk data for the 9 DOF sensor unit. Table 10.4 provides the same observation of acceleration and jerk measurements for the 9 DOF sensor unit. In this case, the acceleration ratio for start and end of motion ranges between 2 and 5, whereas the jerk ratio lies between 1.5 and 5.5 respectively.

Table 10.4: Statistical evaluation of the meaningful signal in dynamic scenario for 9 DOF sensor unit

		motion ID				
motion phase	measure	1	2	3	4	5
start (green)	a $[m/s^2]$	0.25	0.25	0.46	0.20	0.25
	j $[m/s^3]$	5.68	6.61	11.65	3.68	5.99
end (red)	a $[m/s^2]$	0.06	0.07	0.09	0.10	0.07
	j $[m/s^3]$	1.59	1.99	2.03	2.35	1.28

To compute the signal to noise ratio for acceleration and jerk as well as the 3 DOF and 9 DOF sensor units, equation (10.4) is used. Utilizing the amplitude values from table 10.3 and 10.4 for a_{motion} and j_{motion}, the acceleration and jerk mean value as well as the standard deviation for static measurements from table 10.1 and 10.2, the SNR can be calculated. The results for the 3 DOF sensor unit are given in table 10.5 and for the 9 DOF sensor unit in table 10.6 respectively.

For the 3 DOF IMU the SNR lies in the range of 15.34 to 41.19 for the start of a motion and from 1.8 to 3.96 for the end respectively. When comparing the SNR for acceleration and jerk it can be seen that the jerk SNR provides better results with higher signal to noise ratio and therefore more robust information.

Table 10.5: Statistical evaluation of the signal to noise ratio in dynamic scenario for 3 DOF sensor unit

		motion ID				
motion phase	measure	1	2	3	4	5
start (green)	SNR_a	17.19	19.93	33.74	15.41	18.26
	SNR_j	15.34	18.91	41.19	16.39	31.47
end (red)	SNR_a	1.80	2.95	2.66	2.59	2.63
	SNR_j	3.78	3.74	3.96	3.61	3.43

For the 9 DOF sensor unit the SNR provides results between 11.30 and 38.78 for motion start and between 2.16 and 6.68 for motion end respectively. Comparable to the 3 DOF evaluation jerk data SNR gives better results over acceleration SNR.

Table 10.6: Statistical evaluation of the signal to noise ratio in dynamic scenario for 9 DOF sensor unit

		motion ID				
motion phase	measure	1	2	3	4	5
start (green)	SNR_a	17.94	17.93	35.98	14.25	18.66
	SNR_j	18.19	21.38	38.78	11.30	19.25
end (red)	SNR_a	2.16	3.38	4.68	5.40	2.87
	SNR_j	4.06	5.46	5.59	6.68	3.00

The SNR is our criteria to decide which inertial sensor is more suitable to provide meaningful information on the motion status to support the UWB localization system. Table 10.7 shows the mean signal to noise ratios for all combinations of sensor units, measured quantity and motion phase. In case of the start of the patient table movement, 3 DOF and 9 DOF sensors give comparable results. For the stop phase of a motion, the 9 DOF sensor unit gives superior results with a SNR of $34\,\% - 46\,\%$ higher than for the 3 DOF sensor.

Table 10.7: Mean signal to noise ratio in dynamic scenario for 3 DOF and 9 DOF sensor unit and motion start and end phase.

	3 DOF		9 DOF	
motion phase	acc	jerk	acc	jerk
start	20.91	24.67	20.95	21.78
stop	2.53	3.70	3.70	4.96

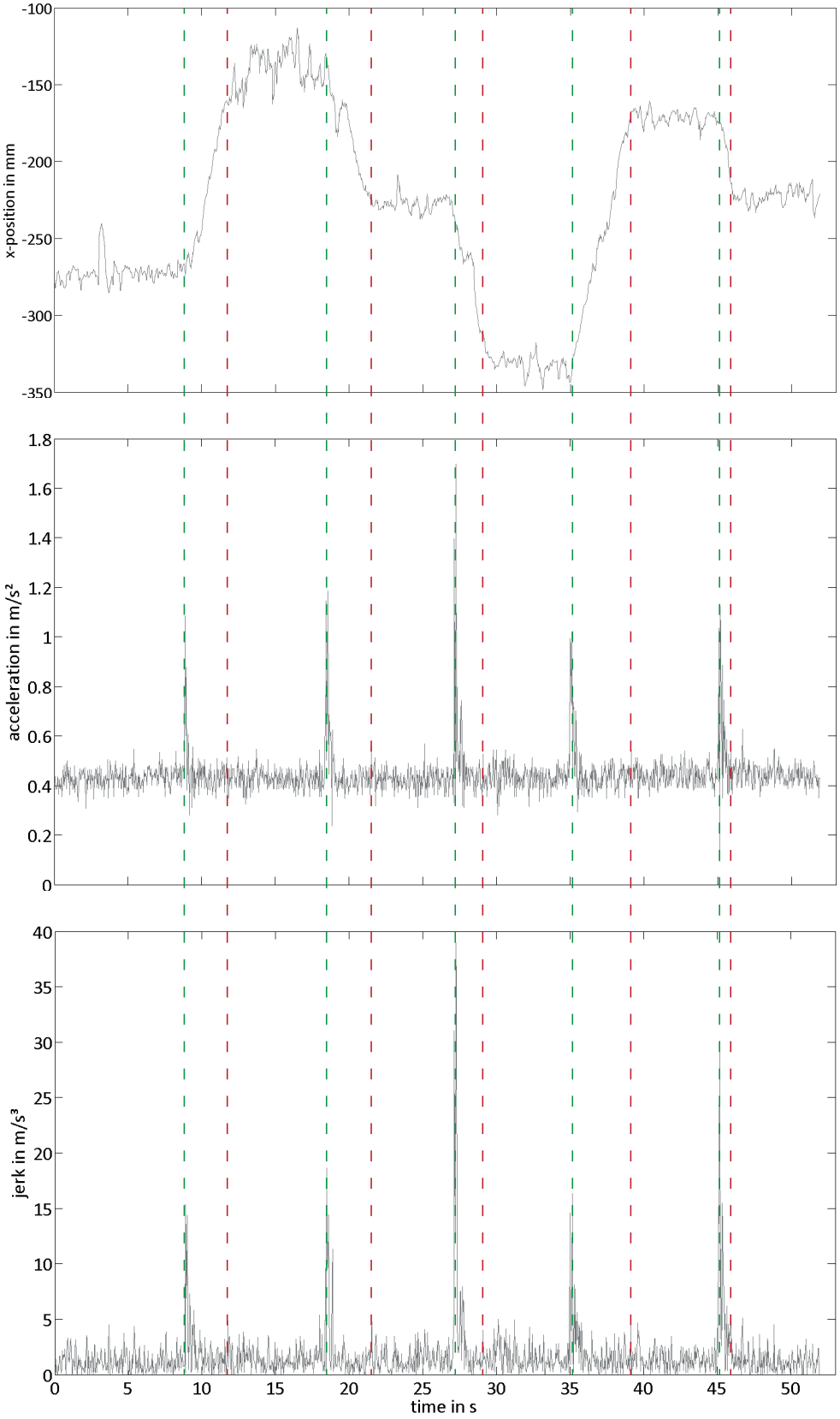

Figure 10.14: Overlay of dynamic position, acceleration and jerk data for the 3 DOF sensor unit. Green dashed lines depict the starting point of a motion in time. Red dashed lines represent the ending point of a motion in time.

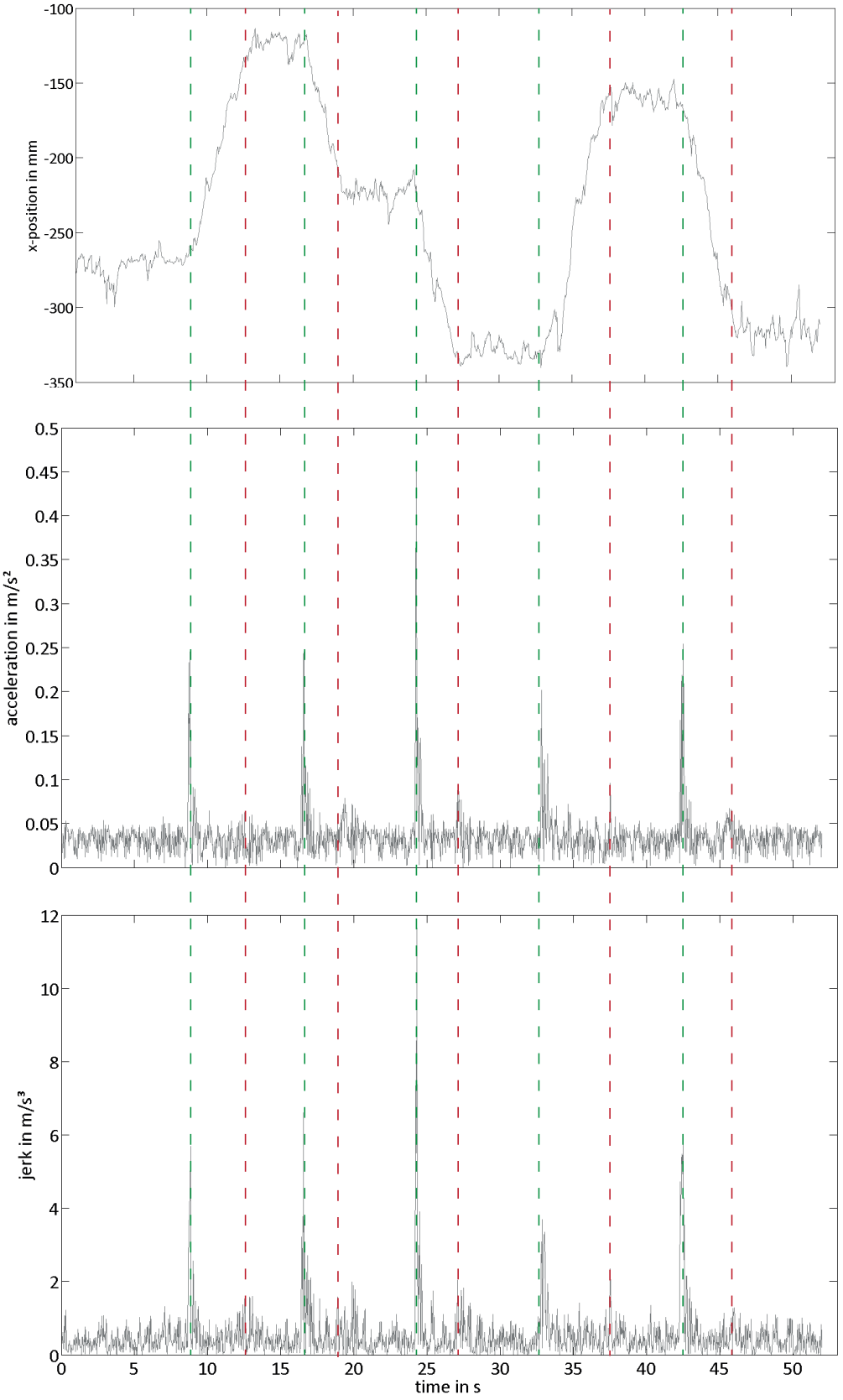

Figure 10.15: Overlay of dynamic position, acceleration and jerk data for the 9 DOF sensor unit. Green dashed lines depict the starting point of a motion in time. Red dashed lines represent the ending point of a motion in time.

10.4 Conclusion

The goal of this section was to identify a suitable sensor technology to support the existing UWB localization system in improving the localization precision in static and dynamic movement scenarios. Therefore it is essential to realize the movement behavior of the object to be tracked. A selection of external sensors is introduced and compared. With identifying inertial navigation as an appropriate technology, a specific sensor to be used in combination with the UWB system has to be determined. With two different sensor units comprising a 3 DOF acceleration sensor on the one hand and a 9 DOF combination of acceleration, gyroscope and magnetic sensor on the other hand several experiments in static and dynamic environment were conducted to find the most appropriate one. For the quality of the sensor units in the considered frame, a specific signal to noise ratio was introduced. Overall the 9 DOF combined sensor unit gives superior results in recognizing motion phases in dynamic scenarios and is therefore used in the following localization prototype.

11 Adaptive Covariance Kalman Filter

There are different approaches to implement the inertial measurements to improve position estimation of the UWB localization system. The most obvious one is to use acceleration data in the prediction phase of the Kalman filter to get an improved prediction of the movement of the UWB modules between update phases. This approach adds IMU measurement data to improve the pure state model based prediction phase and has no influence on the update phase of the Kalman Filter that contains processing of the UWB measurements.

In section 7.3.3 potential inert behavior of the Kalman Filter due to adaptation of the filter parameter ξ is introduced. Low values for ξ result in decreasing diagonal terms of the Kalman covariance matrix. Additionally, the idea is presented to discard the process noise covariance matrix Q that increases the Kalman covariance values in an additive way. By directly providing a lower boundary for the Kalman Filter diagonal terms the dynamics of the filter can be configured more specifically. The approach presented in this thesis combines UWB localization measurements with absolute acceleration information of an IMU. UWB and IMU sensor data are fused using the presented Kalman Filter in a loosely coupled way. The covariance matrix of the Kalman Filter is dynamically adapted based on the absolute acceleration information from the IMU. Figure 11.1 shows the UWB and IMU input to the Kalman Filter.

With the chosen loosely coupled approach there is no need to register UWB and IMU sensor information unlike tightly coupled systems or approaches using an Extended Kalman Filter. In the presented approach, calibration of the sensor can be done independently. To tune the Kalman Filter only the absolute acceleration is used. Therefore, no orientation information is needed for the acceleration. To neglect the gravity of Earth from acceleration measurements from a 3 DOF sensor a high pass filter could be used. With a 9 DOF IMU all necessary information is available to discard the acceleration from gravity. Figure 11.2 provides a detailed view of the Kalman Filter with its state vector and the covariance matrix. The update and prediction phase of the filter are shown where UWB positioning information are input to the update phase as well as the newly introduced tuning phase that uses the absolute acceleration data as input and directly and solely affects the covariance matrix but not the state vector.

For the static scenario experiments conducted in section 8 only the constant velocity state space model with ($\mathbf{x_k} = (x_k, y_k, z_k, \dot{x}_k, \dot{y}_k, \dot{z}_k)$) is utilized. In this chapter the static model with ($\mathbf{x_k} = (x_k, y_k, z_k)$), and the constant acceleration model with ($\mathbf{x_k} = (x_k, y_k, z_k, \dot{x}_k, \dot{y}_k, \dot{z}_k, \ddot{x}_k, \ddot{y}_k, \ddot{z}_k)$), introduced in section 7.3.2 on page 64, are also scrutinized. The different state space models

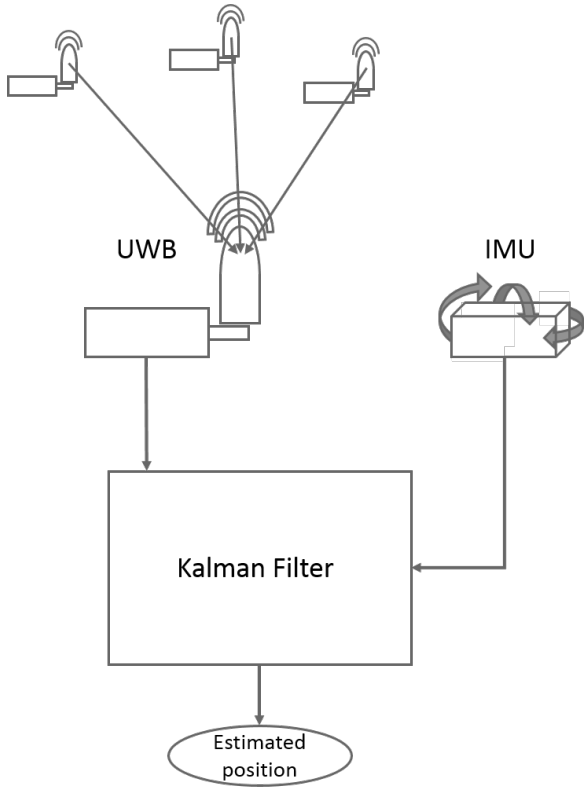

Figure 11.1: Sensor fusion of UWB and IMU using a Kalman Filter. Distance measurements from three references to the mobile UWB modules are used to trilaterate a position estimate. The absolute acceleration is derived from IMU measurements and forwarded as a second input to the Kalman Filter. (BKR17) ©2017 IEEE

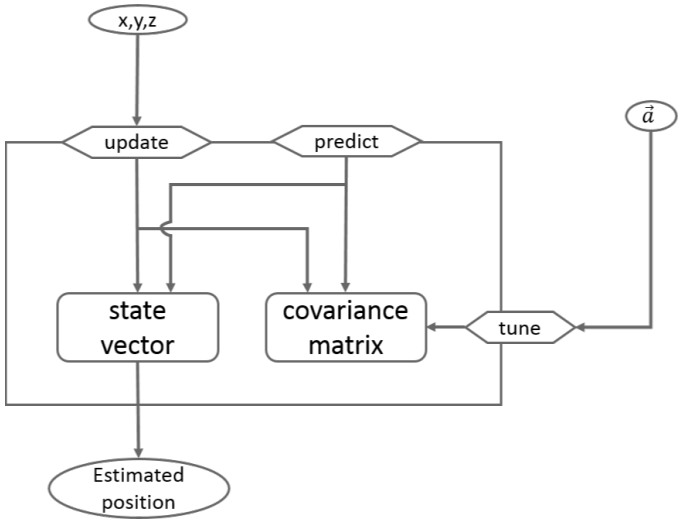

Figure 11.2: Zoom into adaptive Kalman Filter visualizing the three phases and the respective in- and outputs. In the update phase, location data is provided by the UWB system. In the tune phase, acceleration data is provided by the IMU. Filter tuning is applied directly before the next update phase. (BKR17) ©2017 IEEE

do all have their strengths in specific motion scenarios. The static state model assumes no motion and is therefore suitable for static scenarios. The constant velocity model assumes a constant velocity and is therefore well suited for scenarios with linear movements. The constant acceleration model should especially work well during the acceleration phase of a tracked object.

From section 10.3 it is known that the position and their first two derivatives are not always enough to detect the start and end of a movement phase in a robust way. Therefore, the third derivative of the position, the jerk, was introduced as a calculated result from the raw IMU data. In many movement scenarios the jerk gives better information than velocity and acceleration. In the medical environment introduced in section 8.2 moving the patient table results in a noticeable jerk due to released brakes. Based on this knowledge both acceleration and jerk are applied to the tuning factor ξ. Equation (11.1) shows the experimentally derived values for acceleration $\vec{a}$ and jerk j. They are based on a thorough calibration of the IMU for static and dynamic movement scenarios. The lower boundary represents no movement with only measurement noise present whereas the upper boundary represents a clear dynamic movement scenario. A quadratic formula without units is used for acceleration and jerk with $\xi = (50\vec{a})^2 + 1$ and $\xi = (3j)^2 - 10$ respectively whereas the maximum value is use for ξ.

$$\xi = \begin{cases} 0, & \vec{a} < 0.058 \text{ or } j < 1.55 \\ 20, & \vec{a} > 0.082 \text{ or } j > 1.82 \end{cases} \tag{11.1}$$

12 Experiments

The static and dynamic experiments are conducted in the medical environment introduced in section 8.2 with the same sensor setup on the tabletop of the patient table. The proposed dynamic radio location prototype gives an update rate of 30 Hz per localization including covariance adaption based on acceleration and jerk data. Reference measurements are provided by the Optotrak optical stereo camera system. The xml configuration file of the C++ software framework is extended for the additional features of the Kalman Filter. Figure 12.1 indicates two new attributes of the Kalman Filter and an extended comment region.

```
<!--Enlarge for help on Kalman Filter
KalmanMeasurementError: "double value"  (e.g. 20.0) for fixed error estimate
                        "Dynamic"       for adaptive error estimate according
                                        to Time Domain estimate error
ExtSensor:  "None"          No external Sensor -> fixed PminValue defined in
                            " KalmanMinPvalue "
            "Acceleration"  3 DOF Sensor + adaptive PminValue due to jerk data
            "Orientation"   9 DOF Sensor + adaptive PminValue due to Acceleration
                            and jerk data + predict phase with Acceleration Data
StateModel: "Static"        3x1 state model with x-,y- and z- position
            "Velocity"      6x1 state model with x-,y- and z- position
                            and x-, y- and z- velocity
            "Acceleration"  9x1 state model with x-,y- and z- position,
                            x-, y- and z- velocity and x-, y- and z- acceleration-->
    <Kalman BufferSize="1" KalmanMeasurementError="20.0"
    KalmanSystemError="0.0" KalmanMinPvalue="0.0" MaxNodeSpeed="10.0"
    ExtSensor="None" StateModel="Acceleration" />
```

Figure 12.1: Extended configuration of Kalman Filter

„ExtSensor“ indicates whether a 3 DOF, 9 DOF or no external sensor is used. With „StateModel“ the applied state space model can be configured to conduct experiments with three different state models where velocity and acceleration are assumed to be constant in their respective models. In 12.1 real measurement experiments with a fixed Kalman Filter in static and dynamic scenarios are provided. RMSE and standard deviation evaluations are used as reference UWB localization for the adaptive Covariance Kalman Filter implementation. Section 12.2 sheds a light on state space model comparison. It is shown that the assumption from chapter 8 to prefer the constant velocity over static and constant acceleration state models holds true for dynamic motion scenarios. In 12.3 the raw and dynamic radio location data are evaluated against the NDI Optotrak reference system and the fixed Kalman Filter.

12.1 Fixed Kalman Filter

With two variants of the Kalman Filter static and dynamic measurements are conducted in the known medical environment. Raw measurements are recorded and „SimReal“ is used to apply an inert and a dynamic Kalman filter fixed to a low and a high value for ξ respectively. Figure 12.2 presents results of the static measurement campaign with both types of Kalman Filters applied. The inert Kalman Filter configuration levels out the noise in the UWB measurements whereas the dynamic Kalman Filter is tightly related to the raw UWB values. These results match the observations from chapter 8.

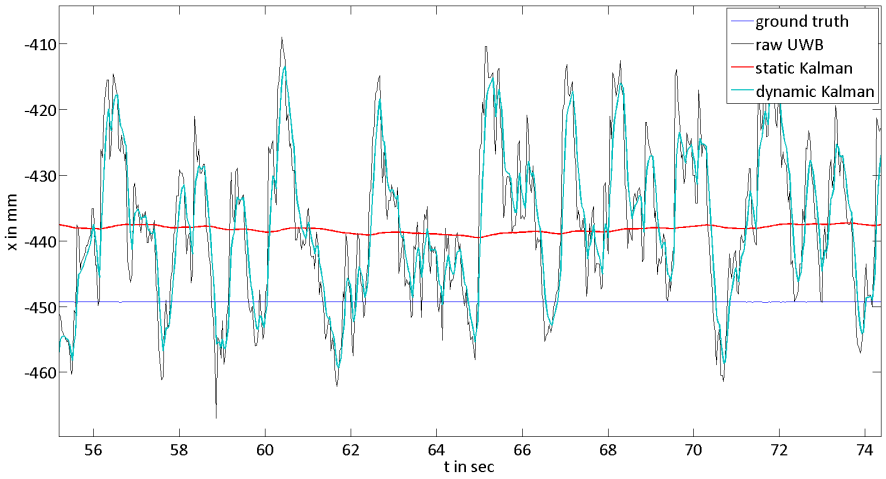

Figure 12.2: UWB raw and Kalman filtered data compared against NDI Optotrak Certus ground truth measurements in a static scene. Filter setup with low and high value for ξ for static and dynamic filter tuning, respectively. (BKR17) ©2017 IEEE

Table 12.1 shows the standard deviation in x, y and z direction for raw measurements compared to the inert and dynamic Kalman Filter. The dynamically tuned Kalman filter shows results close to the raw measurements whereas the static configuration provides a smooth noise behavior.

Table 12.1: Standard deviation of UWB measurements in static scenario (BKR17) ©2017 IEEE

	x [mm]	y [mm]	z [mm]
raw UWB	11.9	12.1	8.0
dynamic Kalman	10.4	10.6	6.9
static Kalman	1.9	3.1	1.5

A dynamic movement scenario is shown in figure 12.3. The Kalman Filter with dynamic filter setup closely follows UWB raw measurements even with the dynamic behavior whereas the inert Kalman filter does not adapt to movement changes.

With a closer look at one plateau phase in figure 12.4 it is clear that the dynamic Kalman Filter does not provide significant reduction of the deviation of positioning results.

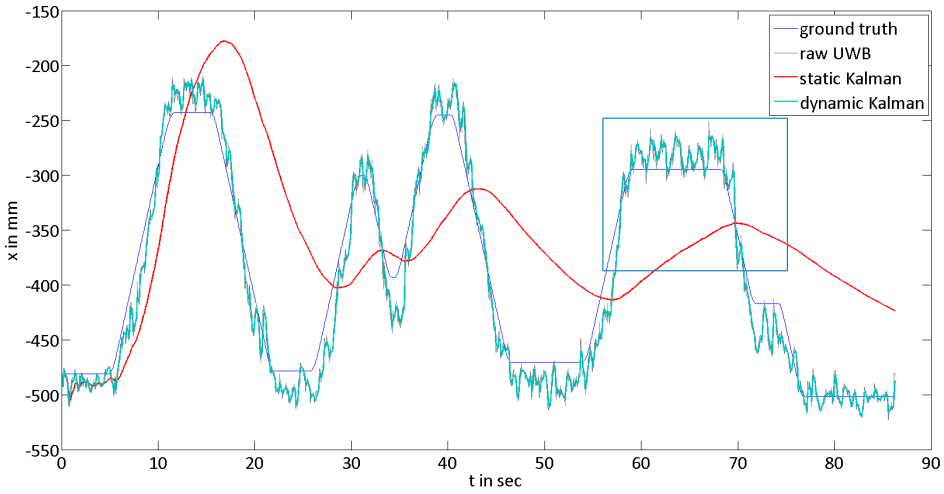

Figure 12.3: UWB raw and Kalman filtered data compared against NDI Optotrak Certus ground truth measurements in a dynamic scene. Filter setup with low and high value for ξ for static and dynamic filter tuning, respectively. (BKR17) ©2017 IEEE

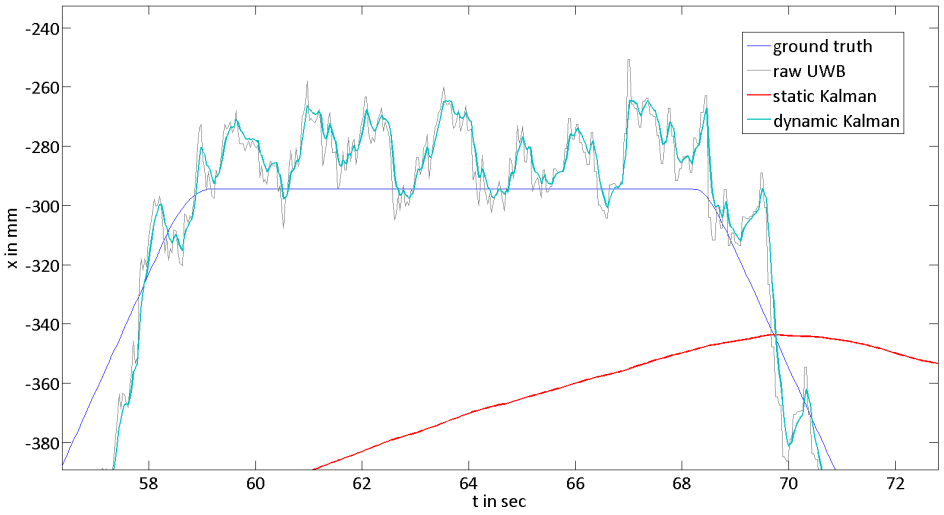

Figure 12.4: Detailed view of static phase in dynamic scenario. (BKR17) ©2017 IEEE

Table 12.2 shows the RMSE in x, y and z direction for raw measurements compared to the inert and dynamic filter setup. The dynamic Kalman Filter is comparable to raw measurements whereas the inert configuration gives high errors in x direction as there was movement in this axis but good filter effect in the static y and z axes.

Table 12.2: RMSE of UWB measurements in dynamic scenario (BKR17) ©2017 IEEE

	x [mm]	y [mm]	z [mm]
raw UWB	21.9	47.8	17.4
dynamic Kalman	22.3	47.4	16.4
static Kalman	76.2	29.6	12.7

12.2 State Model Evaluation

In this section the adaptive covariance Kalman Filter is evaluated using the following three state space models:

static model	$x_k = (x, y, z)$
constant velocity model	$x_k = (x, y, z, \dot{x}, \dot{y}, \dot{z})$
constant acceleration model	$x_k = (x, y, z, \dot{x}, \dot{y}, \dot{z}, \ddot{x}, \ddot{y}, \ddot{z})$

Figure 12.5 shows filter results for all three state models compared to UWB raw measurements. The static state space model does not reflect the ascending and decending movement phases very good whereas smoothly levels out nose in the plateau phase. Both velocity and acceleration state model closely follow the raw UWB values.

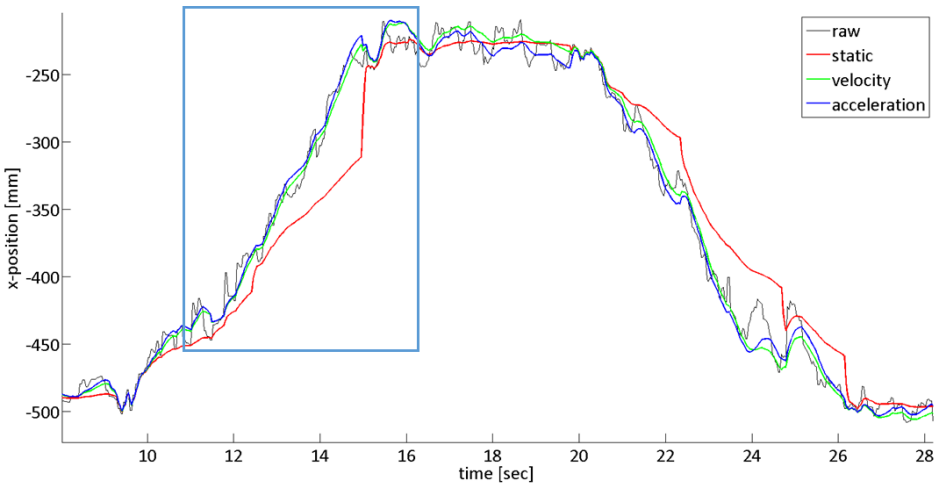

Figure 12.5: Influence of state models in dynamic scene. (BKR17) ©2017 IEEE

Figure 12.6 provides a detailed view on the ascending phase of the measured position data. Position estimation using the static state model is far off during the movement phase. After the movement starts with a jerk for releasing the brakes of the patient table the movement can be approximated with constant velocity and no acceleration. Therefore, the covariance matrix is not adapted based on incoming acceleration or jerk data from the IMU. This leads to a covariance matrix with low values resulting in the system to believe in the current state and to weight incoming measurements from the UWB position system very low. When the movement stops with negative acceleration or a noticeable jerk at around 15 seconds the system adapts the state estimation heavily based on the incoming UWB measurements. Both velocity and acceleration state space model closely follow the raw UWB measurements while they level out measurements noise.

The static state space model does not give good results in constant velocity movement scenarios. Therefore, it cannot be used for the dynamic radio location prototype since many movements in medical environment like rotation of a X-ray C-arm system or lifting of a patient table can be described as constant velocity movements. The constant acceleration state

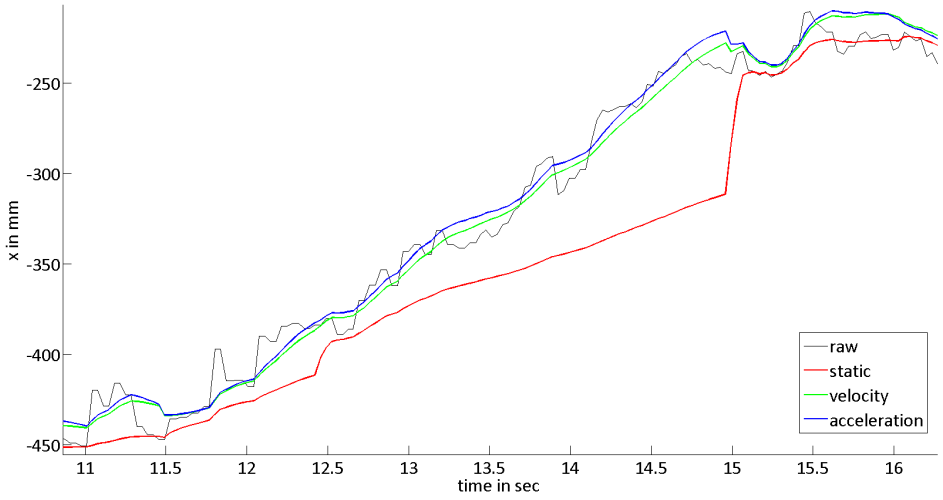

Figure 12.6: Detailed view of state models in ascending phase. (BKR17) ©2017 IEEE

space model gives good results in this experiment. Nevertheless, information on acceleration are already available from the IMU and therefore redundant. Additionally, there are no motions in medical environment that resemble a constant acceleration movement. The constant velocity state space model holds information on the velocity of the tracked object that is not directly available from UWB or IMU measurements. Whenever the IMU does provide acceleration data around 0 the constant velocity state space model provides the most likely current state of the tracked object. This leads to the decision to use the constant velocity state space model for the dynamic radio location prototype.

12.3 Adaptive Covariance Kalman Filter

To better compare the adaptive covariance Kaliman Filter against the Kalman Filters with fixed static and dynamic tuning the same movement scenario from section 12.1 is used. Figure 12.7 provides results for position estimation of dynamic radio location prototype, raw UWB data and the ground truth reference system in a static scenario.

It can be seen that the adaptive covariance Kalman Filter provides smooth position estimation comparable to a fixed statically tuned Kalman Filter. In Table 12.3 the standard deviations of raw UWB measurements and the three filtered localization solutions are compared. The proposed adaptive covariance Kalman Filter gives comparable results to the static Kalman Filter and outperforms the dynamically tuned Kalman Filter.

Figure 12.8 shows positioning results from the dynamic movement experiment. The proposed adaptive covariance Kalman Filter gives comparable results to the Kalman Filter with fixed dynamic configuration from 12.1.

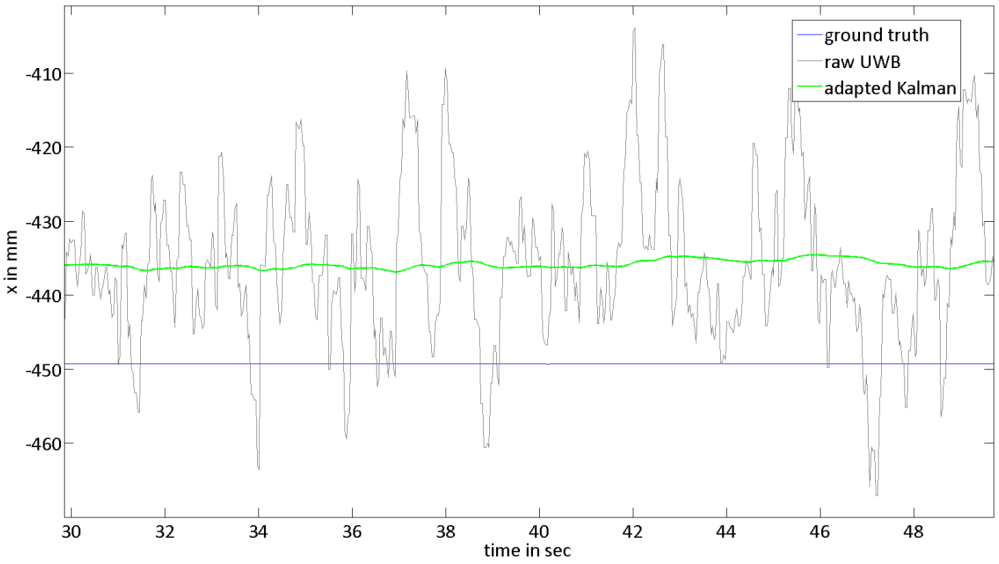

Figure 12.7: Adaptive filter setup applied for a static scenario. The reference measurements are obtained using the optical tracking system NDI Optotrak Certus. (BKR17) ©2017 IEEE

Table 12.3: Standard deviation of UWB measurements in static scenario (BKR17) ©2017 IEEE

	x [mm]	y [mm]	z [mm]
raw UWB	11.9	12.1	8.0
dynamic Kalman	10.4	10.6	6.9
static Kalman	1.9	3.1	1.5
adaptive Kalman	2.1	3.3	1.5

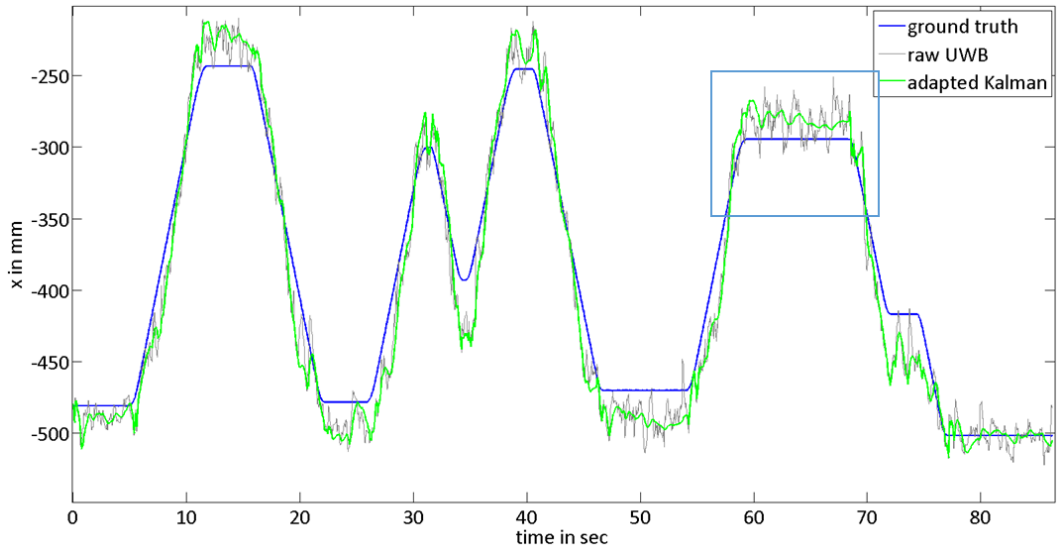

Figure 12.8: Adaptive filter setup applied for a dynamic scenario. The reference measurements are obtained using the optical tracking system NDI Optotrak Certus. (BKR17) ©2017 IEEE

Table 12.4 provides the RMSE of raw UWB positioning data and the three filtered localization solutions. The proposed adaptive covariance Kalman Filter gives comparable but even slightly better results than the dynamic Kalman Filter and outperforms the statically tuned Kalman Filter.

Table 12.4: RMSE of UWB measurements in dynamic scenario (BKR17) ©2017 IEEE

	x [mm]	y [mm]	z [mm]
raw UWB	21.9	47.8	17.4
dynamic Kalman	22.3	47.4	16.4
static Kalman	76.2	29.6	12.7
adaptive Kalman	20.8	47.2	16.1

Figure 12.9 shows a detailed view on the last high plateau phase of the localization experiment. At the end of the ascending movement phase the adaptive covariance Kalman Filter slowly starts to smoothen the position estimates since the acceleration and jerk information from the IMU give very low values and the diagonal elements of the covariance matrix are set to very low numbers. After a few seconds the measurement noise from the UWB positioning estimation is already leveled out and the position results are very smooth. With the start of the next movement phase the adaptive covariance Kalman Filter instantly provides dynamic behavior to follow the motion.

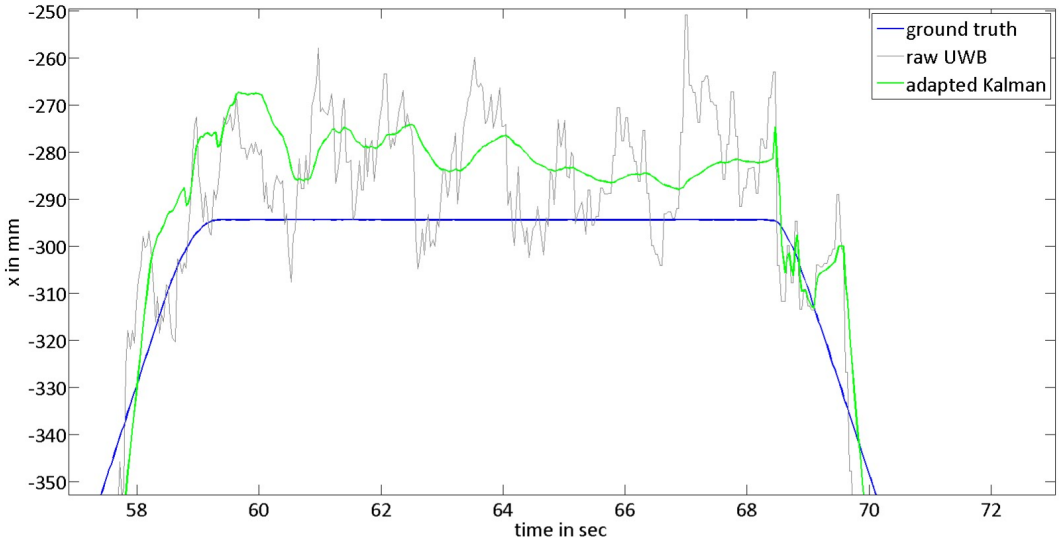

Figure 12.9: Zoom into plateau phase of dynamic scenario. (BKR17) ©2017 IEEE

13 Results and Discussion

The presented positioning and identification system is based on UWB localization combined with acceleration information from an IMU. The fused data using a Kalman Filter leads to very useful localization results in medical environment. The proposed Kalman Filter loosely couples input data from both UWB system and IMU whereas it expects estimated 3D position data from the UWB system and absolute acceleration information form the IMU. The acceleration data is not used is input in the Kalman Filter but directly adapts the diagonal elements of the state covariance matrix to realize a loosely coupled tuning of the Kalman Filter without the need to register UWB and IMU measurement systems or to implement more advanced versions of the Kalman Filter like an Extended Kalman Filter. To fulfill the second goal from section 2 the dynamic radio location prototype comprises only industrially available hardware for UWB positioning and inertial sensors. With 30 Hz the system realizes a reasonable localization rate. Experiments are conducted in an X-ray test lab representing a medical environment with severe multipath reflections due to leaded glass, thick walls and numerous technical devices. For comparison an NDI Optotrak optical reference system as well as static and dynamic non-adapted Kalman Filters are used. The first goal is to find the best suited state space model to represent the tracked object. With static and dynamic movement scenarios conducted in the medical environment it could be shown that the constant velocity state model is best suited for all movement scenarios since the three physical quantities position, velocity and acceleration are covered by UWB, state model and IMU, respectively. The conducted experiments show that the adaptive covariance Kalman Filter outperforms the non-adaptive static and dynamic Kalman Filter versions since it is on par in their strong scenarios and provides much better precision in the weaker scenario, respectively. Precision results give (2.1, 3.1, 1.5) mm in x, y and z for the static scenario which are on par with a Kalman Filter with static state space model applied (BKR17). The proposed adaptive covariance Kalman Filter gives very food RMSE accuracy results of (20.8, 47.2, 16.1) mm in x, y and z and therefore slightly improves the raw UWB measurements although the sensor fusion approach mainly accounts for the precision of the system. It is to mention that the prototypal localization system only comprises three anchor modules and one mobile node.

Part V

Discussion, Outlook and Summary

14 Discussion and Outlook

At the beginning of this thesis the major goal of a prototypal development of a radio location system based on industrially available components, and the evaluation of this system regarding it's feasibility for the proposed medical environment is given. Five specific objectives were introduced to precisely define the goal. In the first part of the discussion it is evaluated whether these objectives are achieved with the proposed work. In a second part the results of the localization prototype are fit into the current literature provided in 3.2.2.

Technology decision based on a comprehensive technology evaluation In this thesis two of the most promising radio location technologies RFID and UWB are introduced and evaluated based on the aspects like accuracy, localization range, sensitivity to multipath, line of sight, power consumption, industrial availability and worldwide regulations. For the pursued usage of localization in medical environment UWB was superior to or on par with RFID in most of the scrutinized aspects. On this basis UWB is used for all prototypal developments in this thesis.

Use of industrially available hardware Industrial availability is one aspect that supports the decision for UWB over RFID. For RFID severeal implementations are available and provided in 3.1.3, but they do not fulfill important requirements for the localization system. For UWB there are many industrially available implementations mostly based on the Decawave DWM1000 chip. The UWB modules used in this thesis are the TimeDomain P410 which are very promising regarding most of the requirements. For the dynamic radio location prototype industrially available IMUs are evaluated and implemented.

Implementation of a suitable localization framework A good framework is important to develop, run and evaluate a localization system. It is important to run the localization in a robust way, configure the system for changing hardware, differently tuned filters and be able to evaluate those configurations with artificial and real localization data. The localization framework provided in this thesis accounts for these requirements. In chapter 8 and 12 configurable parameters for the UWB localization system are introduced. Also, the possibility to log acquired data from UWB, IMU and optical reference systems and reuse it for different configurations is a big advantage in a system evaluation.

Localization accuracy in the low centimeter or even sub-centimeter range In this thesis a very basic localization algorithm is implemented based on the availability of only three UWB reference modules. The applied tracking filters and the additional external sensors mostly improve the precision of the localization system. The achieved accuracy is within the range of $1\,cm$ to $5\,cm$. This result is scraping the demanded accuracy and should be improved in

future work. The outlook later this chapter provides some ideas for working towards this goal.

High localization precision in sub-centimeter range in static and dynamic environment This objective is twofold and expects high precision but also implies robustness in different kinds of environments. To account for precision tracking filters like Particle and Kalman filter are implemented and evaluated in static and dynamic movement scenarios. To realize robust localization in both static and dynamic cases an IMU is integrated into the localization system and used to directly adapt the developed adaptive Kalman filter. With this approach precision in the low millimeter range is achieved for static scenarios with no increase in the localization error in a RMS sense for dynamic scenarios.

There are also some implicit requirements for a localization systems that need to be met. One example is a reasonable localization rate. The introduced prototype runs at 30 Hz which is sufficient for most dynamic scenarios. Another implicit prerequisite is the size of the localization system. Each UWB module consists of a circuit the size of a credit card that can be used in a housing or can be integrated into the object to be localized. Only the antenna needs to be „visible“. The antennas used in this thesis have a size of (7×3) cm. It is possible to use smaller antennas for the pursued scenarios since the required measurement range is limited to a few meters. Overall the goal and the formulated and not formulated but implicit objectives are met.

Several aspects need to be considered when it comes to fit the proposed localization solution into the current literature. The industrially available P410 UWB modules from Time Domain outperform most scientific UWB system introduced in 3.2.2 and can also be seen as benchmark for commercial UWB systems when it comes to accuracy. To improve the precision of the localization system, three tracking algorithms have been implemented and evaluated. A sensor fusion approach was proposed to account for different movement scenarios in medical environments. In contrast to other fusion approaches, which use the IMU measurements as input for the prediction phase of a Kalman filter, given in 3.2.2, the proposed solution directly utilizes the absolute inertial measurements to tune the Kalman covariance matrix and therefore does not need a calibration between the UWB and IMU components. The achieved accuracy and precision with only three anchor nodes provides a good starting point for the evaluation of applications in medical environments.

This thesis proposes a technology evaluation and two prototypal implementations scrutinized in measurement scenarios conducted in a medical environment comparable to clinical ones. To get closer to using UWB in clinical applications several workpackages could be taken as next steps. These steps belong to different fields of research for UWB localization in medical environment. One field of further work could be the overall accuracy of the localization since the precision was already significantly improved with the proposed prototype in this thesis. The accuracy of the adaptive covariance UWB prototype in a RMSE sense is already appropriate for a number of applications but needs additional improvements to provide feasibility for more advanced clinical applications.

One solution to mitigate the systematic accuracy offset between UWB and ground truth measurements involves implementing a range model accounting for the measurement bias for single UWB measurements. Using a linear (MF14) or exponential (GBG+09) function could be used to approach the range model. (BKR17) Since the presented protoypal implementation only uses three UWB anchor nodes to realize an under-determined localization scenario an overall improvement could be pursued by introducing additional UWB nodes. These additional UWB nodes could be used as anchors or mobile UWB nodes. With additional anchors more advanced localization algorithms like the on introduced in chapter 5.2.2 could be applied to estimate the position of mobile UWB modules. This would lead to increased robustness, precision and accuracy. With the additional UWB nodes used as mobile UWB nodes a cooperative approach where also ranging information between mobile UWB nodes are utilized could be beneficial (WCM+11). (DCLW08) and (CGD+12) give some insight on the necessity to truly understand when and with which UWB node cooperation is useful since additional measurement inputs could also be detrimental to the localization result. Another field of future work could be the investigation of suitable clinical applications and a prototypal evaluation with the currently available or an extended UWB localization prototype. There are many examples worth investigating. For future prototypes that include more UWB nodes it would be reasonable to make use of the latest improvements in UWB localization products that arrived at the market recently, e. g. the P440 module by TimeDomain (Tim17).

15 Summary

For years, technical devices play a key-role in advancing medical interventions and supporting physicians in their work. A number of advanced applications that could realize a substantial benefit are in need for identification and localization of the surrounding medical environment including stationary and actively moving devices. Among the technical devices in an OR or interventional suite are imaging systems, patient tables, displays, lead shields and trolleys for tools or other functions like contrast agent injectors. A spatio-temporal localization framework can provide the missing information, Co-registered operations of multiple medical devices, autonomous movement or basic collision avoidance as a first step could be realized using this information. In this thesis a dynamic radio location system for precise localization in medical environment based on a sensor fusion approach using Ultra wideband and inertial sensor data is presented. An adaptive covariance Kalman Filter is introduced to combine the available sensor measurements in a way that they individually contribute to the localization result in different ways.

In part I the need for localization of tools or objects in many medical scenarios is motivated. Available approaches for specific questions are provided in a state of the art. Based on this information the goal of this thesis, to develop a suitable radio location system for use in a medical environment, is derived and specified.

Part II starts with a thorough introduction on two promising radio technologies RFID and UWB. For each technology the basic principles and important technical aspects are given. To point out the importance of the possibility of global use of the radio location system, regulatory aspects are discussed in detail. Furthermore, a study on available scientific and industrial solutions is given for each technology. A conclusion and a decision for the UWB technology completes the radio technology section. In a next step four important ranging technologies are introduced and assessed for their use in an UWB localization system. Three well-known localization techniques are depicted and evaluated to conclude this part.

Part III starts with the decision and introduction of the utilized P410 UWB hardware by Time Domain. This implies the utilization of a two-way time of flight ranging approach that provides absolute ranges between UWB modules. Spherical trilateration, in an under-constrained setup with three UWB anchors, is used as localization technology for the developed UWB localization system. Counter-measures to account for common error causes in localization are described and implemented. In a next step tracking filter approaches are introduced to improve the precision behavior of the raw UWB localization system. A comprehensive localization framework is implemented to address artificial simulations, real measurements

and the recording and replay of measurement data to apply and test different system and filter configurations. A Kalman, Particle and Moving Average Filter are implemented and scrutinized heavily in simulations and real experiments in the medical environment described in this context. This part concludes with the insight of the UWB localization system being either appropriate for static behavior or for dynamic scenarios depending on the tuning of the tracking filter. For precise position estimation in all motion and non motion phases additional information needs to be involved.

Part IV introduces seven types of sensor technology that provide information based around positioning and evaluates their suitability to complement UWB localization data. Inertial sensors and magnetic compasses are the two approaches that are found to be the most appropriate technology candidates. Two explicit implementations of inertial measurement units are introduced and evaluated in real experiments in the proposed medical environment. As a conclusion an inertial measurement unit providing 9 degrees of freedom is used to complement the UWB positioning measurement. The structure of the Kalman Filter is predestined for sensor fusion. In this thesis an approach to utilize additional sensor input to directly tune the Kalman covariance matrix is introduced. Experiments are conducted to evaluate three state models and the Adaptive Covariance Kalman Filter against an optical measurement system and the previously introduced fixed Kalman Filter approach. Results show that the presented adaptive localization approach leads to highly precise position estimation results independent of the motion behavior of the tracked object.

In Part V the thesis is summarized and an overall discussion is given regarding the initial requirements for a radio location system in medical environments. An outlook for future possibilities is given to conclude the thesis.

Bibliography

Azzouzi, Salah ; Cremer, Markus ; Dettmar, Uwe ; Knie, Thomas ; Kronberger, Rainer: Improved AoA based localization of UHF RFID tags using spatial diversity. In: *RFID-Technologies and Applications (RFID-TA), 2011 IEEE International Conference on* IEEE, 2011, S. 174–180

Azzouzi, Salah ; Cremer, Markus ; Dettmar, Uwe ; Kronberger, Rainer ; Knie, Thomas: New measurement results for the localization of uhf rfid transponders using an angle of arrival (aoa) approach. In: *2011 IEEE International Conference on RFID* IEEE, 2011, S. 91–97

Albaidhani, Abbas ; Morell, Antoni ; Vicario, Jose L.: Ranging in UWB using commercial radio modules: Experimental validation and NLOS mitigation. In: *Indoor Positioning and Indoor Navigation (IPIN), 2016 International Conference on* IEEE, 2016, S. 1–7

Atmel. `http://www.atmel.com`. Version: 2017

Arnitz, Daniel ; Witrisal, Klaus ; Muehlmann, Ulrich: Multifrequency continuous-wave radar approach to ranging in passive UHF RFID. In: *IEEE Transactions on Microwave Theory and Techniques* 57 (2009), Nr. 5, S. 1398–1405

Borenstein, Johann ; Everett, HR ; Feng, Liqiang u. a.: Where am I? Sensors and methods for mobile robot positioning. In: *University of Michigan* 119 (1996), Nr. 120, S. 15

Barras, David ; Ellinger, Frank ; Jackel, Heinz ; Hirt, Walter: Low-power ultra-wideband wavelets generator with fast start-up circuit. In: *IEEE Transactions on Microwave Theory and Techniques* 54 (2006), Nr. 5, S. 2138–2145

BeSpoon SAS. `http://bespoon.com/`. Version: 2017

Borenstein, J. ; Feng, L ; Wehe, D.: Mobile Robot Positioning Sensors and Techniques. In: *Journal of Robotic Systems, Special Journal of Robotic Systems, Special Issue on Mobile Robots* 14 (1997), 06. `http://dx.doi.org/10.1002/(SICI)1097-4563(199704)14:43.0.CO;2-R`. – DOI 10.1002/(SICI)1097–4563(199704)14:43.0.CO;2–R

Bin, Liu: SRD and its Challenge - SRD Management in China. In: *ITU Workshop on Short Range Devices and Ultra Wideband* (2014)

Briese, Danilo ; Kunze, Holger ; Rose, Georg: High precision uwb-based 3d localization for medical environment. In: *2015 IEEE International Conference on Ubiquitous Wireless Broadband (ICUWB)* IEEE, 2015, S. 1–5

Briese, Danilo ; Kunze, Holger ; Rose, Georg: UWB localization using adaptive covariance Kalman Filter based on sensor fusion. In: *2017 IEEE 17th International Conference on Ubiquitous Wireless Broadband (ICUWB)* IEEE, 2017, S. 1–7

Robert Bosch GmbH. `http://www.bosch-sensortec.com/en`. Version: 2017

Brainlab AG. `https://www.brainlab.com`. Version: 2017

Corrales, Juan A. ; Candelas, FA ; Torres, Fernando: Hybrid tracking of human operators using IMU/UWB data fusion by a Kalman filter. In: *Human-Robot Interaction (HRI), 2008 3rd ACM/IEEE International Conference on* IEEE, 2008, S. 193–200

CEPT, ECC: ECC decision of 24 March 2006 on the harmonised conditions for devices using ultra-wideband (UWB) technology in bands below 10.6 GHz. In: *ECC/DEC/(06)* 4 (2006)

Conti, Andrea ; Guerra, Matteo ; Dardari, Davide ; Decarli, Nicolo ; Win, Moe Z.: Network experimentation for cooperative localization. In: *IEEE Journal on Selected Areas in Communications* 30 (2012), Nr. 2, S. 467–475

Cleary, Kevin ; Kinsella, A: OR 2020: the operating room of the future. In: *Journal of laparoendoscopic & advanced surgical techniques. Part A* 15 (2005), Nr. 5, S. 495–497

Cheng, Chieh C. ; Lesyna, David A. ; Moyers, Michael F. u. a.: *Path planning and collision avoidance for movement of instruments in a radiation therapy environment.* Oktober 9 2007. – US Patent 7,280,633

Çetin, Ömer ; Nazli, Hakki ; Gürcan, Rıdvan ; Öztürk, Hilmi ; Güneren, Hilal ; Yelkovan, Yasin ; Çayir, Mustafa ; Çelebi, Hasari ; Partal, Hakan P.: An experimental study of high precision TOA based UWB positioning systems. In: *Ultra-Wideband (ICUWB), 2012 IEEE International Conference on* IEEE, 2012, S. 357–361

Code Mercenaries Hard- und Software GmbH. `http://codemercs.com/de/`. Version: 2017

Contigiani, Marco ; Pietrini, Rocco ; Mancini, Adriano ; Zingaretti, Primo: Implementation of a tracking system based on UWB technology in a retail environment. In: *Mechatronic and Embedded Systems and Applications (MESA), 2016 12th IEEE/ASME International Conference on* IEEE, 2016, S. 1–6

Chawla, Kirti ; Robins, Gabriel: An RFID-based object localisation framework. In: *International journal of radio frequency identification technology and applications* 3 (2011), Nr. 1-2, S. 2–30

Chawla, Kirti ; Robins, Gabriel ; Zhang, Liuyi: Object localization using RFID. In:

Wireless Pervasive Computing (ISWPC), 2010 5th IEEE International Symposium on IEEE, 2010, S. 301–306

De Angelis, Alessio ; Nilsson, John ; Skog, Isaac ; Händel, Peter ; Carbone, Paolo: Indoor positioning by ultrawide band radio aided inertial navigation. In: *Metrology and Measurement Systems* 17 (2010), Nr. 3, S. 447–460

Dart Ultra-Wideband by Zebra Technologies, Inc. https://www.zebra.com/us/en/solutions/location-solutions/enabling-technologies/dart-uwb.html. Version: 2017

Dardari, Davide ; Conti, Andrea ; Lien, Jaime ; Win, Moe Z.: The effect of cooperation on UWB-based positioning systems using experimental data. In: *EURASIP Journal on Advances in Signal Processing* 2008 (2008), S. 124

Decawave Ltd. http://www.decawave.com/. Version: 2017

Dejan: *MEMS Accelerometer Gyroscope Magnetometer & Arduino.* https://howtomechatronics.com/how-it-works/electrical-engineering/mems-accelerometer-gyrocope-magnetometer-arduino/. Version: 2016

Domdouzis, Konstantinos ; Kumar, Bimal ; Anumba, Chimay: Radio-Frequency Identification (RFID) applications: A brief introduction. In: *Advanced Engineering Informatics* 21 (2007), Nr. 4, S. 350–355

Dobkin, Daniel M.: *The rf in RFID: uhf RFID in practice.* Newnes, 2012

europe.com healthcare-in: *Next generation O-arm ? Surgical Imaging System.* http://www.healthcare-in-europe.com/en/article/16130-next-generation-o-arm-surgical-imaging-system.html. Version: 2016. – O-arm and optical navigation system by Medtronic

FCC, Federal Communication C. u. a.: First report and order, Revision of Part 15 of commission's rules regarding ultra-wideband transmission system. In: *FCC 02-48* (2002), February

Fang, Bertrand T.: Simple solutions for hyperbolic and related position fixes. In: *IEEE transactions on aerospace and electronic systems* 26 (1990), Nr. 5, S. 748–753

Finkenzeller, K.: *RFID-Handbuch: Grundlagen und praktische Anwendungen von Transpondern, kontaktlosen Chipkarten und NFC.* Hanser, 2012 https://books.google.de/books?id=QI1WtQAACAAJ. – ISBN 9783446429925

Fischer, Gunter ; Klymenko, Oleksiy ; Martynenko, Denys ; Luediger, Heinz: An impulse radio UWB transceiver with high-precision TOA measurement unit. In: *Indoor Positioning and Indoor Navigation (IPIN), 2010 International Conference on* IEEE, 2010, S. 1–8

Faseth, T. ; Winkler, M. ; Arthaber, H. ; Magerl, G.: The influence of multipath

propagation on phase-based narrowband positioning principles in UHF RFID. In: *2011 IEEE-APS Topical Conference on Antennas and Propagation in Wireless Communications*, 2011, S. 1144–1147

González, Javier ; Blanco, Jose-Luis ; Galindo, Cipriano ; Galisteo, A Ortiz-de ; Fernandez-Madrigal, Juan-Antonio ; Moreno, Francisco A. ; Martínez, Jorge L.: Mobile robot localization based on ultra-wide-band ranging: A particle filter approach. In: *Robotics and autonomous systems* 57 (2009), Nr. 5, S. 496–507

Gulhar, Abhinav ; Briese, Danilo ; Mewes, Philip W. ; Rose, Georg: Registration of a robotic system to a medical imaging system. In: *Intelligent Robots and Systems (IROS), 2015 IEEE/RSJ International Conference on* IEEE, 2015, S. 3208–3213

Gomes, Paula: Surgical robotics: Reviewing the past, analysing the present, imagining the future. In: *Robotics and Computer-Integrated Manufacturing* 27 (2011), Nr. 2, S. 261–266

Gezici, Sinan ; Poor, H V.: Position estimation via ultra-wide-band signals. In: *Proceedings of the IEEE* 97 (2009), Nr. 2, S. 386–403

Regulatory status for using RFID in the EPC Gen2 (860 to 960 MHz) band of the UHF spectrum. `http://www.gs1.org/epc-rfid`. Version: November 2016

Guvenc, Ismail ; Sahinoglu, Zafer: Threshold-based TOA estimation for impulse radio UWB systems. In: *2005 IEEE International Conference on Ultra-Wideband* IEEE, 2005, S. 420–425

Gezici, Sinan ; Sahinoglu, Zafer ; Kobayashi, Hisashi ; Poor, H V.: Ultra-wideband impulse radio systems with multiple pulse types. In: *IEEE Journal on Selected Areas in Communications* 24 (2006), Nr. 4, S. 892–898

Gezici, Sinan ; Sahinoglu, Zafer ; Molisch, Andreas F. ; Kobayashi, Hisashi ; Poor, H V.: A two-step time of arrival estimation algorithm for impulse radio ultra wideband systems. In: *Signal Processing Conference, 2005 13th European* IEEE, 2005, S. 1–6

Gezici, Sinan ; Tian, Zhi ; Giannakis, Georgios B. ; Kobayashi, Hisashi ; Molisch, Andreas F. ; Poor, H V. ; Sahinoglu, Zafer: Localization via ultra-wideband radios: a look at positioning aspects for future sensor networks. In: *Signal Processing Magazine, IEEE* 22 (2005), Nr. 4, S. 70–84

Heidrich, J. ; Brenk, D. ; Essel, J. ; Fischer, G. ; Weigel, R. ; Schwarzer, S.: Local positioning with passive UHF RFID transponders. In: *2009 IEEE MTT-S International Microwave Workshop on Wireless Sensing, Local Positioning, and RFID*, 2009, S. 1–4

Hol, Jeroen ; Dijkstra, Fred ; Luinge, Henk ; Schön, Thomas u. a.: Tightly coupled UWB/IMU pose estimation. (2009)

Healthineers, Siemens: *AXIOM Artis dFC/dBC Magnetic Navigation.* `http://w5.siemens.com/web/ua/ru/medecine/archive/cardio_angio/dfc_dbc_`

magnetic_navigation/pages/dfc_dbc_magnetic_navigation.aspx. Version: 2017. – Niobe EM system by Stereotaxis

Homier, Eric A. ; Scholtz, Robert A.: Rapid acquisition of ultra-wideband signals in the dense multipath channel. In: *Ultra Wideband Systems and Technologies, 2002. Digest of Papers. 2002 IEEE Conference on* IEEE, 2002, S. 105–109

Hightower, Jeffrey ; Want, Roy ; Borriello, Gaetano: SpotON: An indoor 3D location sensing technology based on RF signal strength. In: *UW CSE 00-02-02, University of Washington, Department of Computer Science and Engineering, Seattle, WA* 1 (2000)

Hekimian-Williams, Cory ; Grant, Brandon ; Liu, Xiuwen ; Zhang, Zhenghao ; Kumar, Piyush: Accurate localization of RFID tags using phase difference. In: *2010 IEEE International Conference on RFID (IEEE RFID 2010)* IEEE, 2010, S. 89–96

IDOLINK Co.,Ltd. http://www.ido-link.com/english/main.action. Version: 2017

Inc., Keckler Medical C.: *Hybrid Operating Rooms featuring Siemens Imaging Systems.* http://hybridoperatingroom.com/hybrid-operating-room-designs-layouts-pictures-examples/. Version: March 2017

International, ECMA: *Standard ECMA-368 - High Rate Ultra Wideband PHY and MAC Standard.* 3. 2008 https://www.ecma-international.org/publications-and-standards/standards/ecma-368/

Jiménez, AR ; Seco, F: Comparing Decawave and Bespoon UWB location systems: Indoor/outdoor performance analysis. In: *Indoor Positioning and Indoor Navigation (IPIN), 2016 International Conference on* IEEE, 2016, S. 1–8

Khan, M A. ; Antiwal, Videep K.: Location estimation technique using extended 3-D LANDMARC algorithm for passive RFID tag. In: *Advance Computing Conference, 2009. IACC 2009. IEEE International* IEEE, 2009, S. 249–253

Kalman, Rudolph E.: A new approach to linear filtering and prediction problems. In: *Journal of Fluids Engineering* 82 (1960), Nr. 1, S. 35–45

Kuruoglu, Gulnur S. ; Erol, Melike ; Oktug, Sema: Localization in wireless sensor networks with range measurement errors. In: *Telecommunications, 2009. AICT'09. Fifth Advanced International Conference on* IEEE, 2009, S. 261–266

Kok, Manon ; Hol, Jeroen D. ; Schon, Thomas B.: Indoor positioning using ultrawideband and inertial measurements. In: *Vehicular Technology, IEEE Transactions on* 64 (2015), Nr. 4, S. 1293–1303

Kronberger, Rainer ; Knie, Thomas ; Leonardi, Roberto ; Dettmar, Uwe ; Cremer, Markus ; Azzouzi, Salah: UHF RFID localization system based on a phased array antenna. In: *Antennas and Propagation (APSURSI), 2011 IEEE International Symposium on* IEEE, 2011, S. 525–528

Kröll, Harald ; Steiner, Christoph: Indoor ultra-wideband location fingerprinting. In: *Indoor Positioning and Indoor Navigation (IPIN), 2010 International Conference on* IEEE, 2010, S. 1–5

Kuester, Daniel G.: *Passive binary-modulated backscatter in microwave networks with applications to RFID*, Citeseer, Diss., 2012

Li, Gang ; Arnitz, Daniel ; Ebelt, Randolf ; Muehlmann, Ulrich ; Witrisal, Klaus ; Vossiek, Martin: Bandwidth dependence of CW ranging to UHF RFID tags in severe multipath environments. In: *2011 IEEE International Conference on RFID* IEEE, 2011, S. 19–25

Landt, Jeremy: The history of RFID. In: *IEEE potentials* 24 (2005), Nr. 4, S. 8–11

Ladikos, Alexander ; Benhimane, Selim ; Navab, Nassir: Real-time 3D reconstruction for collision avoidance in interventional environments. In: *International Conference on Medical Image Computing and Computer-Assisted Intervention* Springer, 2008, S. 526–534

Liu, Jun S. ; Chen, Rong: Sequential Monte Carlo methods for dynamic systems. In: *Journal of the American statistical association* 93 (1998), Nr. 443, S. 1032–1044

Liu, Xiaotao ; Corner, Mark D. ; Shenoy, Prashant: Ferret: RFID localization for pervasive multimedia. In: *International Conference on Ubiquitous Computing* Springer, 2006, S. 422–440

Lee, Joon-Yong ; Scholtz, Robert A.: Ranging in a dense multipath environment using an UWB radio link. In: *IEEE Journal on Selected Areas in Communications* 20 (2002), Nr. 9, S. 1677–1683

Li, Xin ; Zhang, Yimin ; Amin, Moeness G.: Multifrequency-based range estimation of RFID tags. In: *2009 IEEE International Conference on RFID* IEEE, 2009, S. 147–154

Li, Zhonghua ; Zhou, Zijing ; He, Chunhui ; Huang, Xiao: Advances in RFID-ILA: The past, present and future of RFID-based indoor location algorithms. In: *Control and Decision Conference (CCDC), 2012 24th Chinese* IEEE, 2012, S. 3830–3835

Medtronic plc. `http://www.medtronic.com`. Version: 2017

Monica, Stefania ; Ferrari, Gianluigi: An experimental model for UWB distance measurements and its application to localization problems. In: *Ultra-WideBand (ICUWB), 2014 IEEE International Conference on* IEEE, 2014, S. 297–302

MiddleEastHealthMag.com: *The dream machine.* `http://www.middleeasthealthmag.com/cgi-bin/index.cgi?http://www.middleeasthealthmag.com/may2006/feature3.htm`. Version: 2006. – Brainsuite by Brainlab AG

Miesen, Robert ; Kirsch, Fabian ; Vossiek, Martin: Holographic localization of passive

uhf rfid transponders. In: *2011 IEEE International Conference on RFID* IEEE, 2011, S. 32–37

Miesen, Robert ; Kirsch, Fabian ; Vossiek, Martin: UHF RFID localization based on synthetic apertures. In: *IEEE Transactions on Automation Science and Engineering* 10 (2013), Nr. 3, S. 807–815

Future-Shape GmbH. `http://www.future-shape.com/en/technologies/32/navifloor-robots-localisation-with-rfid`. Version: 2017

NDI, Northern Digital Inc. `http://http://www.ndigital.com/`. Version: 2017

Ni, Lionel M. ; Liu, Yunhao ; Lau, Yiu C. ; Patil, Abhishek P.: LANDMARC: indoor location sensing using active RFID. In: *Wireless networks* 10 (2004), Nr. 6, S. 701–710

Nikitin, Pavel V. ; Martinez, Rene ; Ramamurthy, Shashi ; Leland, Hunter ; Spiess, Gary ; Rao, KVS: Phase based spatial identification of UHF RFID tags. In: *2010 IEEE International Conference on RFID (IEEE RFID 2010)* IEEE, 2010, S. 102–109

Papapostolou, Apostolia ; Chaouchi, Hakima: RFID-assisted indoor localization and the impact of interference on its performance. In: *Journal of Network and Computer Applications* 34 (2011), Nr. 3, S. 902–913

Pietrzyk, Michal M. ; Grün, Thomas von d.: Experimental validation of a TOA UWB ranging platform with the energy detection receiver. In: *Indoor Positioning and Indoor Navigation (IPIN), 2010 International Conference on* IEEE, 2010, S. 1–8

Povalac, Ales ; Sebesta, Jiri: Phase difference of arrival distance estimation for RFID tags in frequency domain. In: *RFID-Technologies and Applications (RFID-TA), 2011 IEEE International Conference on* IEEE, 2011, S. 188–193

Quantitec GmbH. `http://intranav.com/`. Version: 2017

Rahim, Md A.: *Interference Mitigation Techniques to Support Coexistence of Ultra-WideBand Systems.* Jörg Vogt Verlag, 2010

Rappaport, Theodore S.: *Wireless Communications: Principles and Practice.* Dorling Kindersley, 2009 (Prentice Hall communications engineering and emerging technologies series). `https://books.google.co.uk/books?id=11qEWkNFFwQC`. – ISBN 9788131728826

Redpoint Positioning Corporation. `https://www.redpointpositioning.com/`. Version: 2017

Rembold, Bernhard: Optimum modulation efficiency and sideband backscatter power response of RFID-tags. In: *Frequenz* 63 (2009), Nr. 1-2, S. 9–13

Ramirez-Mireles, Fernando ; Scholtz, RA: Multiple-access performance limits with time hopping and pulse position modulation. In: *Military Communications Conference, 1998. MILCOM 98. Proceedings., IEEE* Bd. 2 IEEE, 1998, S. 529–533

Ricci, William M. ; Russell, Thomas A. ; Kahler, David M. ; Terrill-Grisoni, Lauralan ; Culley, Patrick: A comparison of optical and electromagnetic computer-assisted navigation systems for fluoroscopic targeting. In: *Journal of orthopaedic trauma* 22 (2008), Nr. 3, S. 190–194

Soonjun, Suwatchai ; Boontri, Dokor ; Cherntanomwong, Panarat: A novel approach of RFID based indoor localization using fingerprinting techniques. In: *2009 15th Asia-Pacific Conference on Communications* IEEE, 2009, S. 475–478

Sewio Networks, s.r.o. `http://www.sewio.net/`. Version: 2017

Schroeder, Jens ; Galler, Stefan ; Kyamakya, Kyandoghere: A low-cost experimental ultra-wideband positioning system. In: *Ultra-Wideband, 2005. ICU 2005. 2005 IEEE International Conference on* IEEE, 2005, S. 632–637

Silva, Bruno ; Pang, Zhibo ; Akerberg, Johan ; Neander, Jonas ; Hancke, Gerhard: Experimental study of UWB-based high precision localization for industrial applications. In: *Ultra-WideBand (ICUWB), 2014 IEEE International Conference on* IEEE, 2014, S. 280–285

Scherhäufl, Martin ; Pichler, Markus ; Schimbäck, Erwin ; Müller, Dominikus J. ; Ziroff, Andreas ; Stelzer, Andreas: Indoor localization of passive UHF RFID tags based on phase-of-arrival evaluation. In: *IEEE Transactions on Microwave Theory and Techniques* 61 (2013), Nr. 12, S. 4724–4729

Scherhäufl, Martin ; Pichler, Markus ; Stelzer, Andreas: Localization of passive UHF RFID tags based on inverse synthetic apertures. In: *2014 IEEE International Conference on RFID (IEEE RFID)* IEEE, 2014, S. 82–88

Strong, E B. ; Rafii, Amir ; Holhweg-Majert, Bettina ; Fuller, Scott C. ; Metzger, Marc C.: Comparison of 3 optical navigation systems for computer-aided maxillofacial surgery. In: *Archives of Otolaryngology–Head & Neck Surgery* 134 (2008), Nr. 10, S. 1080–1084

Stoica, Lucian ; Rabbachin, Alberto ; Oppermann, Ian: A low-complexity noncoherent IR-UWB transceiver architecture with TOA estimation. In: *IEEE Transactions on Microwave Theory and Techniques* 54 (2006), Nr. 4, S. 1637–1646

Sczyslo, S. ; Schroeder, J. ; Galler, S. ; Kaiser, T.: Hybrid localization using UWB and inertial sensors. In: *2008 IEEE International Conference on Ultra-Wideband* Bd. 3, 2008, S. 89–92

Stereotaxis Inc. `http://www.stereotaxis.com/`. Version: 2017

Stockman, Harry: Communication by means of reflected power. In: *Proceedings of the IRE* 36 (1948), Nr. 10, S. 1196–1204

Sarkka, Simo ; Viikari, Ville V. ; Huusko, Miika ; Jaakkola, Kaarle: Phase-based

UHF RFID tracking with nonlinear Kalman filtering and smoothing. In: *IEEE Sensors Journal* 12 (2012), Nr. 5, S. 904–910

TELECOMMUNITY, ASIA-PACIFIC: APT Report on Ultra Wideband (UWB). (2012)

Tiemann, Janis ; Eckermann, Fabian ; Wietfeld, Christian: ATLAS-an open-source TDOA-based Ultra-wideband localization system. In: *Indoor Positioning and Indoor Navigation (IPIN), 2016 International Conference on* IEEE, 2016, S. 1–6

TDC Acquisition Holdings, Inc. `http://www.timedomain.com/`. Version: 2017

Taylor, Russell H. ; Stoianovici, Dan: Medical robotics in computer-integrated surgery. In: *Robotics and Automation, IEEE Transactions on* 19 (2003), Nr. 5, S. 765–781

Ubisense Group plc. `https://ubisense.net/de`. Version: 2017

Viikari, Ville ; Pursula, Pekka ; Jaakkola, Kaarle: Ranging of UHF RFID tag using stepped frequency read-out. In: *IEEE Sensors Journal* 10 (2010), Nr. 9, S. 1535–1539

Wille, Andreas ; Broll, Magdalena ; Winter, Susanne: Phase difference based RFID navigation for medical applications. In: *2011 IEEE International Conference on RFID* IEEE, 2011, S. 98–105

Win, Moe Z. ; Conti, Andrea ; Mazuelas, Santiago ; Shen, Yuan ; Gifford, Wesley M. ; Dardari, Davide ; Chiani, Marco: Network localization and navigation via cooperation. In: *IEEE Communications Magazine* 49 (2011), Nr. 5

WhereNet by Zebra Technologies, Inc. `https://www.zebra.com/us/en/solutions/location-solutions/enabling-technologies/wherenet.html`. Version: 2017

Wang, Jue ; Katabi, Dina: Dude, where's my card?: RFID positioning that works with multipath and non-line of sight. In: *ACM SIGCOMM Computer Communication Review* 43 (2013), Nr. 4, S. 51–62

Wille, Andreas ; Muzalewski, Mathäus ; Winter, Susanne: RFID-basierte Navigation auf Grundlage unterschiedlicher Messgrößen. In: *Automatisierungstechnische Verfahren für die Medizin* (2012), S. 47–48

Nanjing Woxu Wireless Co.,Ltd. `http://www.woxuwireless.com/`. Version: 2017

Win, Moe Z. ; Scholtz, Robert A.: Impulse radio: How it works. In: *IEEE Communications letters* 2 (1998), Nr. 2, S. 36–38

Wille, Andreas ; Winter, Susanne: Medical navigation based on RFID tag signals: Model and simulation. In: *Biomed tech* 55 (2010), Nr. 1, S. 2

Wang, Shangbo ; Waadt, Andreas ; Burnic, Admir ; Xu, Dong ; Kocks, Christian ; Bruck, Guido H. ; Jung, Peter: System implementation study on RSSI based positioning in UWB networks. In: *Wireless Communication Systems (ISWCS), 2010 7th International Symposium on* IEEE, 2010, S. 36–40

YANG, Liuqing ; GIANNAKIS, Georgios B.: Timing ultra-wideband signals with dirty templates. In: *IEEE Transactions on Communications* 53 (2005), Nr. 11, S. 1952–1963

ZHANG, Yimin ; AMIN, Moeness G. ; KAUSHIK, Shashank: Localization and tracking of passive RFID tags based on direction estimation. In: *International Journal of Antennas and Propagation* 2007 (2007)

ZWIRELLO, Lukasz ; LI, Xuyang ; ZWICK, Thomas ; ASCHER, Christian ; WERLING, Sebastian ; TROMMER, Gert F.: Sensor data fusion in UWB-supported inertial navigation systems for indoor navigation. In: *Robotics and Automation (ICRA), 2013 IEEE International Conference on* IEEE, 2013, S. 3154–3159

ZHOU, Junru ; ZHANG, Hongjian ; MO, Lingfei: Two-dimension localization of passive RFID tags using AOA estimation. In: *Instrumentation and Measurement Technology Conference (I2MTC), 2011 IEEE* IEEE, 2011, S. 1–5

Part VI

Appendix

A RFID transponders

Figure A.1: Various implementations of RFID transponders are available on the market. It starts with printed tags with different antenna designs in a, b and c. Other exemplars like d and e are fabricated in plastic material to be more robust. Massive housing of the RFID antenna can be found in f and g to be able to use the tags on metallic surfaces. RFID tag f is embedded in a flexible and wearable wristband.

B UWB regulations

Table B.1: UWB band group allocation (Int08)

Band Group	Band ID	Lower Frequency (MHz)	Center Frequency (MHz)	Upper Frequency (MHz)
1	1	3168	3432	3696
	2	3696	3960	4224
	3	4224	4488	4752
2	4	4752	5016	5280
	5	5280	5544	5808
	6	5808	6072	6336
3	7	6336	6600	6864
	8	6864	7128	7392
	9	7392	7656	7920
4	10	7920	8184	8448
	11	8448	8712	8976
	12	8976	9240	9504
5	13	9504	9768	10032
	14	10032	10296	10560
6	9	7392	7656	7920
	10	7920	8184	8448
	11	8448	8712	8976

Table B.2: Emission Limits for UWB for indoor applications in the USA. ($F^{+}02$)

Frequency Band [MHz]	Indoor Applications [dBm]
$0.009 - 960$	§15.209
$960 - 1610$	-75.3
$1610 - 1990$	-53.3
$1990 - 3100$	-51.3
$3100 - 10600$	-41.3
$10600 - 22000$	-51.3
$22000 - 29000$	-51.3
Above 29000	-51.3

Frequency range	Maximum mean e.i.r.p. spectral density	Maximum peak e.i.r.p. (defined in 50 MHz)
Below 1.6 GHz	-90 dBm/MHz	-50 dBm
1.6 to 2.7 GHz	-85 dBm/MHz	-45 dBm
2.7 to 3.4 GHz (Notes 1 and 2)	-70 dBm/MHz	-36 dBm
3.4 to 3.8 GHz (Notes 1 and 2)	-80 dBm/MHz	-40 dBm
3.8 to 4.2 GHz (Notes -1 and 2)	-70 dBm/MHz	-30 dBm
4.2 to 4.8 GHz (Notes 1 and 2)	-70 dBm/MHz	-30 dBm
4.8 to 6 GHz	-70 dBm/MHz	-30 dBm
6 to 8.5 GHz	-41.3 dBm/MHz	0 dBm
8.5 to 10.6 GHz (Note 2)	-65 dBm/MHz	-25 dBm
Above 10.6 GHz	-85 dBm/MHz	-45 dBm

Table B.3: Emission Limits for UWB in EU with maximum mean EIRP spectral density per MHz and maximum peak EIRP defined per 50 MHz). (CEP06)

	Operational frequency	3.1 - 3.4 GHz	3.4 - 3.8 GHz[1]	3.8 - 4.8 GHz[1]	8.5 - 9 GHz
	Minimum initial channel availability check time	14s	5.1s		14s
Zone 1 for Signal detection level S >A	Maximum mean e.i.r.p. spectral density	-70 dBm/MHz	-80 dBm/MHz	-70 dBm/MHz	-65 dBm/MHz
	Default Avoidance bandwidth	300 MHz	200 MHz		500 MHz
Signal Detection threshold A		-38 dBm	-38 dBm		-61 dBm
Zone 2 for Signal detection level A > S > B	Maximum mean e.i.r.p. spectral density	-41.3 dBm/MHz	-65 dBm/MHz		-41.3 dBm/MHz
	Default Avoidance bandwidth	-	200 MHz		-
Signal Detection threshold B			-61 dBm		
Zone 3 for Signal detection level S < B	Maximum mean e.i.r.p. spectral density	-	-41.3 dBm/MHz		-
Definitions of the parameters in table 3 can be found in ECC Report 120. [1] Detection mechanism needs to be validated to protect existing operation of victim stations of radio services such as BWA terminals					

Table B.4: ECC Detect and Avoid mitigation techniques. (CEP06)

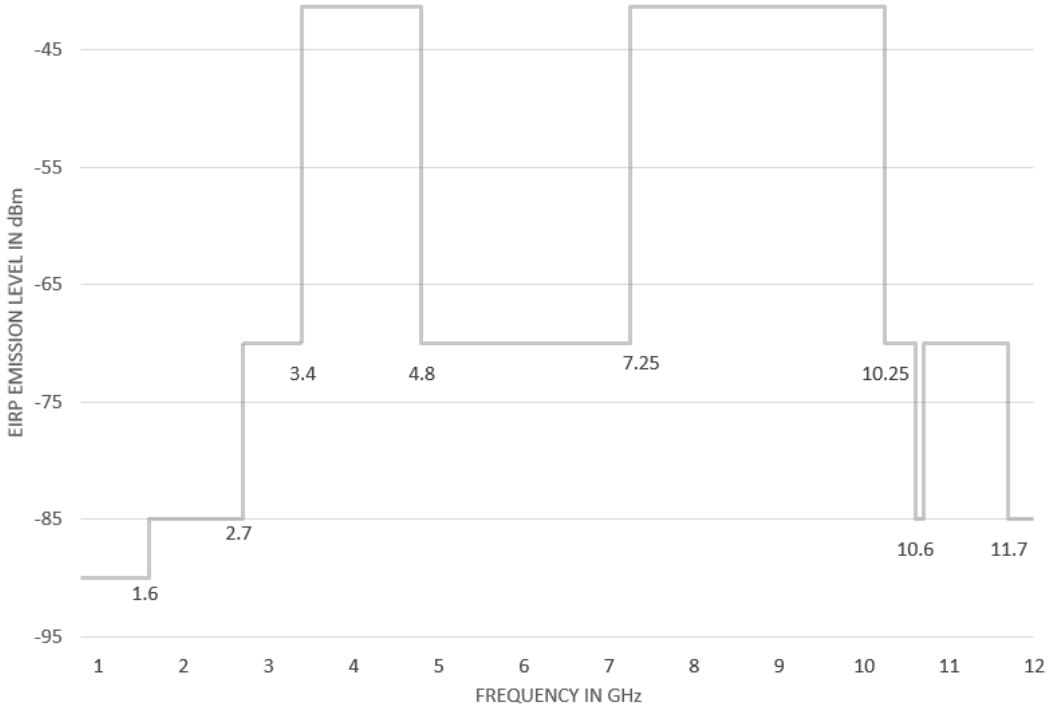

Figure B.1: UWB regulatory mask in Japan based on (TEL12)

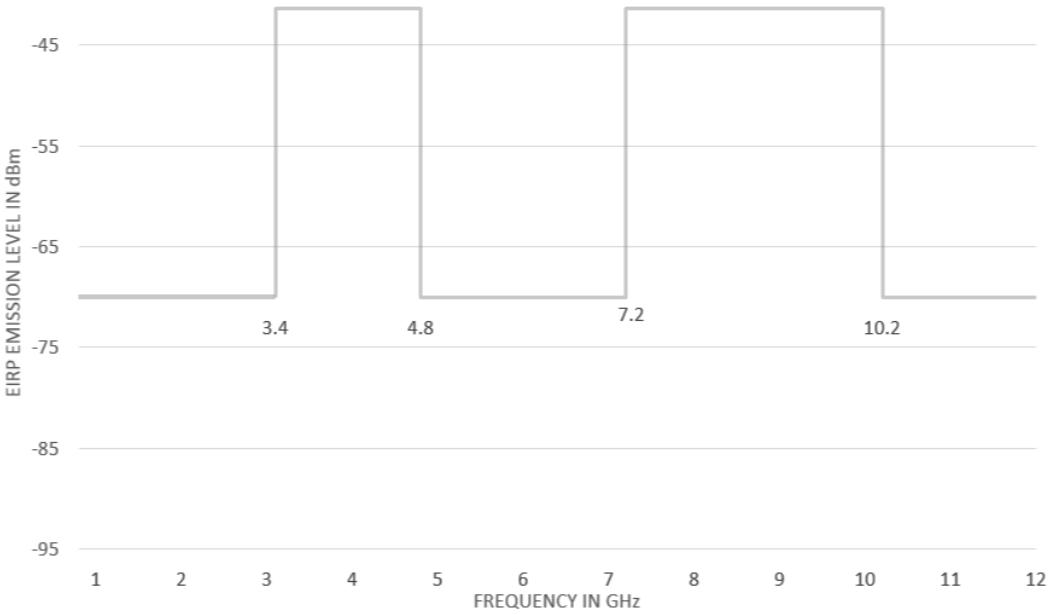

Figure B.2: UWB regulatory mask in Korea based on (TEL12)

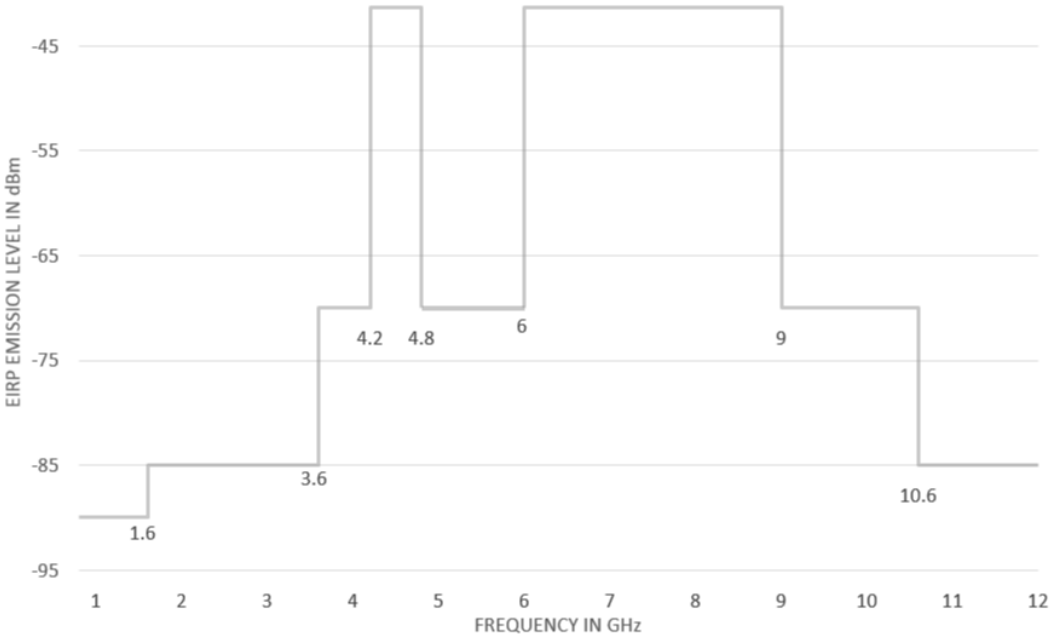

Figure B.3: UWB regulatory mask in China based on (Bin14)

C UWB Broadspec antenna

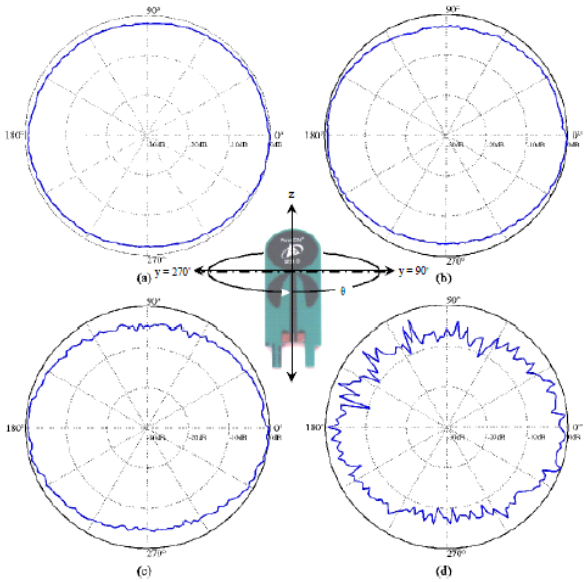

Figure C.1: UWB Broadspec antenna azimuth beam pattern. (Tim17)

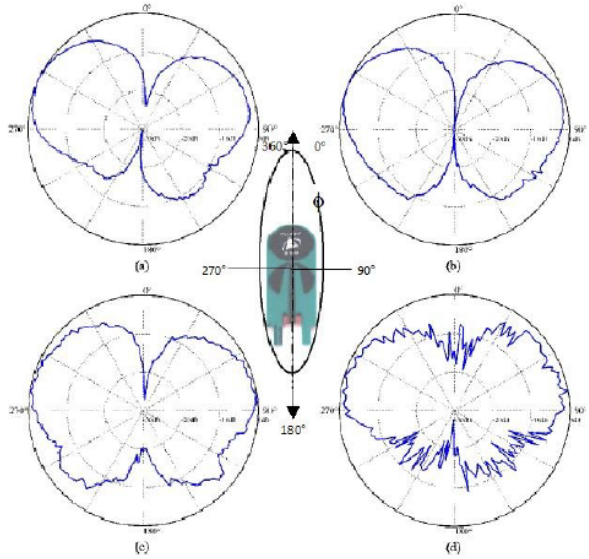

Figure C.2: UWB Broadspec antenna elevation beam pattern. (Tim17)

D Inertial Measurement Unit

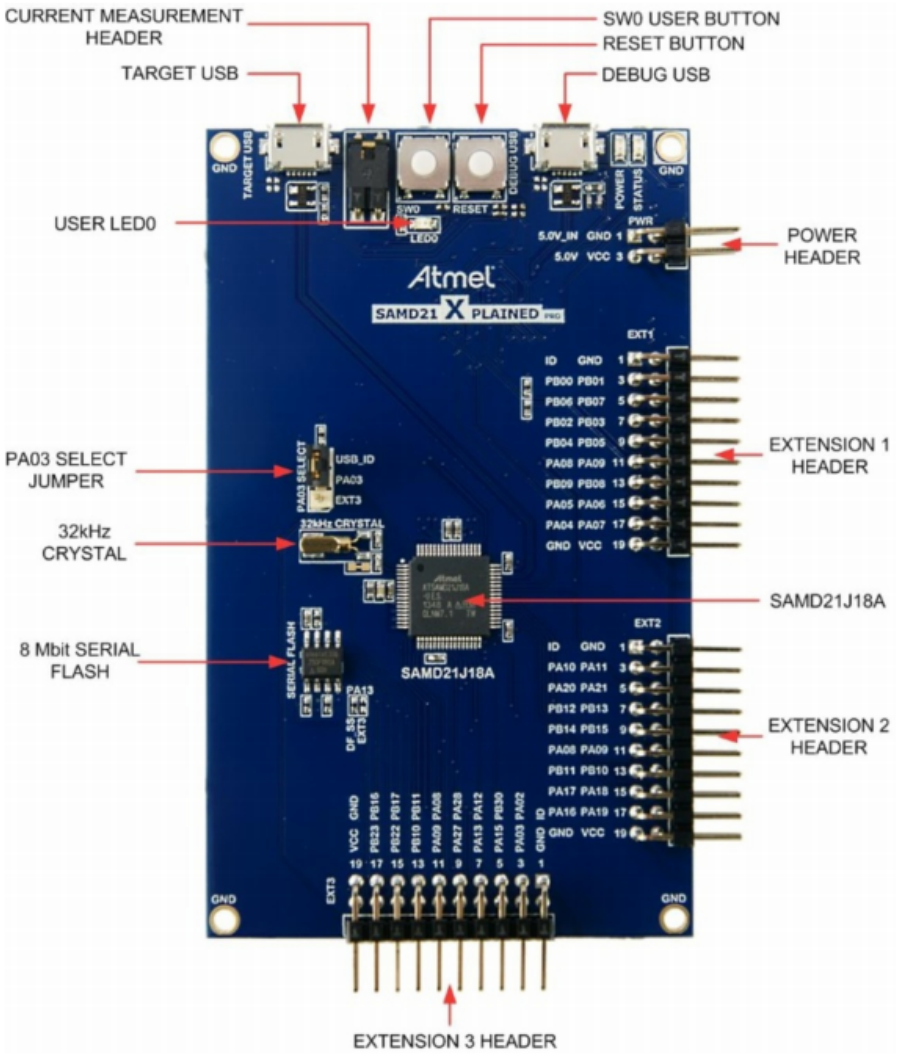

Figure D.1: Basicboard for 9 DOF Sensor.

Publications

Parts of this thesis have been previously published. Material on radio location using UWB in medical environment in part III has been published in

BRIESE, D.; KUNZE, H.; ROSE, G.: High Precision UWB-based 3D Localization for Medical Environment. In: Proceedings of IEEE International Conference on Ubiquitous Wireless Broadband, Montréal, 2015.

Sensor fusion of UWB and inertial sensors for the dynamic radio location prototype in part IV is related to

BRIESE, D.; KUNZE, H.; ROSE, G.: UWB Localization using adaptive covariance Kalman Filter based on Sensor Fusion. In: Proceedings of IEEE International Conference on Ubiquitous Wireless Broadband, Salamanca, 2017.

Outside of the scope of this theses fall the following publications.

GULHAR, A.; **BRIESE, D.**, MEWES, P.; ROSE, G.: Registration of a Robotic System to a Medical Imaging System. In: Proceedings of IEEE International Conference on Intelligent Robots and Systems, Hamburg, 2015.

BRIESE, D.; GULHAR, A.; KUNZE, H., NIEBLER, C.; MEWES, P.; ROSE, G.: Co-registration of robotic systems in medical environment. In: Proceeding of the IGIC - Conference on Image-Guided Interventions, Magdeburg, 2014.

BRIESE, D.; NIEBLER, C.; ROSE, G.: Hand-Eye Calibration using Dual Quaternions in Medical Environment. In: Proceedings of the SPIE - Progress in Biomedical Optics and Imaging, San Diego, 2014.